Manuscript Click here to view linked References

A member of a new dynamin superfamily modulates mitochondrial membrane branching in *Trypanosoma brucei*

Chloé Alexandra Morel[1], Corinne Asencio[1], David Moreira[2], Corinne Blancard[3], Bénédicte Salin[3], Etienne Gontier[4], Stéphane Duvezin-Caubet[3], Manuel Rojo[3], Frédéric Bringaud[1] and Emmanuel Tetaud[1*]

[1]Univ. Bordeaux, CNRS, MFP, UMR 5234, F-33000, Bordeaux, France
[2]Ecologie Systématique Evolution, CNRS, Université, Paris-Sud, Université Paris-Saclay, AgroParisTech, Gif-sur-Yvette, France.
[3]Univ. Bordeaux, CNRS, IBGC, UMR 5095, F-33000, Bordeaux, France
[4]Univ. Bordeaux, CNRS, BIC, UAR 3420, F-33000, Bordeaux, France

*Correspondence: emmanuel.tetaud@u-bordeaux.fr

SUMMARY

Unlike most other eukaryotes, where mitochondria continuously fuse and divide, the mitochondrion of trypanosome cells forms a single and continuously interconnected network that divides only during cytokinesis. However, the machinery governing mitochondrial remodeling and interconnection of trypanosome mitochondrion remain largely unknown. We functionally characterize a novel dynamin-superfamily protein (DSP) from *T. brucei* (*Tb*MfnL) which shares close similarity with a family of homologs present in various eukaryotic and prokaryotic phyla, but not in opisthokonts like mammals and budding yeast. The sequence and domain organization of *Tb*MfnL is distinct and it is phylogenetically very distant from the yeast and mammalian dynamin-related proteins involved in mitochondrial fusion/fission dynamincs, such as Opa1 and Mfn. *Tb*MfnL localizes to the inner mitochondrial membrane facing the matrix, and upon overexpression, induces a strong increase in the interconnection and branching of mitochondrial filaments in a GTPase-dependent manner. *Tb*MfnL is a component of a novel membrane remodeling machinery with an unprecedented matrix-side localization that is able to modulate the degree of intermitochondrial connections.

34 **Keywords:** Mitochondrial dynamics – Dynamin-superfamily protein - Membrane
35 remodeling - Evolution – *Trypanosomes*

INTRODUCTION

Trypanosoma brucei is a parasite responsible for African sleeping sickness as well as the related cattle disease Nagana, affecting sub-Saharan Africa. *T. brucei* is transmitted to mammals by an insect vector: the tsetse fly (*Glossina* spp.). During the trypanosome life cycle, the parasite exists in at least two replicative forms; the procyclic form (PCF), transmitted by the tsetse fly, and the bloodstream form (BSF) responsible for diseases in vertebrates. Unlike most other eukaryotes that contain numerous mitochondria, trypanosomes have a single mitochondrion, which is highly elongated and reticulated. In contrast to yeast and mammals, with tens to hundreds of mitochondrial DNA (mtDNA) nucleoids distributing throughout the mitochondrial compartment, the mitochondrial genome of trypanosome is restricted to a specific structure at the basis of the flagellum known as kinetoplast (kDNA) [1]. During the trypanosome life cycle and its adaptation to different hosts and environments, the shape of its mitochondrial compartment undergoes spectacular changes that reflect its functional plasticity [2]. Indeed, the mitochondrion of this parasite exists in at least two major forms: (i) the fully active and developed one characteristic for the PCF that harbors the oxidative phosphorylation complexes (OXPHOS) for energy production [3, 4] and (ii) the functionally less active and morphologically reduced form found in the bloodstream, with energy produced exclusively through glycolysis since OXPHOS is repressed [5]. These modifications correlate with the adaptation of the parasite to the proline-rich hemolymph and tissue fluids of the blood-feeding tsetse fly and the glucose-rich blood of a mammalian host [6]. Since studies in mammals and in yeast having unraveled tight links between mitochondrial bioenergetics, morphology and dynamics [7-9], it is tempting to assume that such close relationships not only regulate mitochondrial function and energy metabolism, but also the life cycle and pathogenic potential of trypanosomes. However, in contrast to fungi and metazoa, where mitochondrial morphology and fusion/fission dynamics have been thoroughly characterized [10, 11], little is known about the morphology and dynamics of mitochondria in trypanosomes.

In most eukaryotes, mitochondria are very dynamic, alternating between two major events, fusion and fission. Mitochondrial dynamics allows to maintain mitochondrial morphology, distribution and size [8]. The main proteins involved in these events are large GTPases belonging to the dynamin superfamily protein (DSP), such as Dnm1/Drp1 in yeast and mammalian cells, which are soluble

71 protein transiently recruited to mitochondrial and peroxisomal membranes to
72 mediate organelle division [12, 13]. Mammalian mitochondrial fusion requires
73 fusion of outer mitochondrial membrane (OMM) followed by fusion of inner
74 mitochondrial membrane (IMM) which is carried out by mitofusins 1 and 2 (Mfn1
75 and Mfn2) and optic atrophy 1 (Opa1), respectively [14, 15]; while mitofusins are
76 anchored to the OMM and face the cytosol, Opa1 localizes to the mitochondrial
77 inter-membrane space (IMS). Alteration of fusion/fission dynamics and of the
78 equilibrium between them provokes mitochondrial fragmentation or hyperfusion
79 [12, 16], and is linked to diseases, notably neuropathies [17].
80 The investigation of mitochondrial fission and fusion in trypanosomes has been
81 relatively limited until now. Available evidence indicates that mitochondrial fission
82 is restricted to cell division [18, 19] and may not occur continuously [18, 20] but
83 can be induced artificially [19, 21]. Evidence for mitochondrial fusion in
84 trypanosomes came 25 years ago from *in vivo* genetic exchange of mtDNA [22].
85 Finally, a recent study of mitochondrial dynamics in another trypanosomatid,
86 *Crithidia fasciculata*, unveiled the occurrence of mitochondrial fission, fusion, and
87 sliding throughout the cell cycle, pointing to the existence of mitochondrial fusion
88 and fission machineries in trypanosomatids [23].
89 Two decades of research have revealed that numerous mitochondrial fission and
90 fusion factors that, despite significant differences, appear conserved in fungi and
91 mammals [24]. In plants, mitochondria also fuse and divide. While plant DSPs
92 involved in fission are known, factors directly involved in fusion have not been
93 identified, suggesting the existence of a fusion machinery differing from that of
94 yeast and mammals [25, 26], [27]. So far, only two dynamin-like proteins (*Tb*Dlp)
95 have been described in *T. brucei* (Tb927.3.4720 and Tb927.3.4760): their ablation
96 impairs mitochondrial division and endocytosis and leads to cytokinesis arrest [19,
97 28, 29]. *Tb*Dlp thus appears to be the functional homolog of Drp1/Dnm1 in
98 mammals and yeast, but its fission activity on mitochondria seems restricted to
99 the cytokinesis [19]. Another presumed DSP (*Tb*MfnL, Tb927.7.2410) has been
100 also reported to be involved in mitochondrial fission [30]. To date, however, no
101 protein involved in mitochondrial fusion has been identified in trypanosomes.
102 In this study, we revisited the function of the trypanosome DSP *Tb*MfnL [30].
103 Phylogenic analysis reveals that this protein defines a new family of DSP found in
104 both eukaryotes and prokaryotes but absent from organisms containing Mfn or
105 Opa1 homologs (fungi and mammals) and from plants. We find that excess *Tb*MfnL

106 leads to increased mitochondrial branching and interconnexion and we show that
107 it is anchored to the mitochondrial inner membrane, facing the matrix. Taken
108 together, these findings suggest that *Tb*MfnL is not involved in fission, but
109 mediates or modulates mitochondrial interconnection and branching.
110
111 **RESULTS**
112 **1 - Sequence analysis of *Tb*MfnL identifies it as a member of a novel**
113 **dynamin family.**
114 To identify potential fusion players, we started our search by careful re-
115 examination of trypanosome genomic and proteomic databases for proteins
116 showing sequence homology to known fusion factors (Opa1/Mfn1-2/Fzo1). We
117 were only able to identify the previously reported dynamin-related protein, named
118 *Tb*Mfn-Like or *Tb*MfnL (Tb927.7.2410) [30], that displays a domain organization
119 that has more similarities with mammalian and yeast fusion factors of the outer
120 membrane (Mfn2/Fzo1) than of the inner membrane (Opa1) (**Figure 1A and**
121 **Table S1**). Analysis of the *Tb*MfnL sequence revealed several motifs and domains,
122 including an N-terminal region containing a predicted mitochondrial targeting
123 signal (MTS) with potential cleavage sites (**Figure S1**), followed by a GTPase
124 domain with conserved G1 to G4 motifs and two consecutive C-terminal
125 transmembrane domains (TMs) (**Figure 1A and Figures S1/S2**). The presence
126 of an N-terminal MTS makes it unlikely for *Tb*MfnL to localize to the outer
127 membrane, as Mfn/Fzo, and the absence of an N-proximal TM domain, which
128 prevents Opa1 import into the matrix, suggests that *Tb*MfnL is imported into the
129 matrix and does not represent a functional homolog of the fusion factors Opa1 or
130 Mfn.
131 We next investigated whether this DSP could be conserved in other organisms.
132 Using Blastp with *Tb*MfnL as a query to search various protein databases, we
133 identified well-conserved sequences in relatives of *Trypanosoma* belonging to the
134 class Kinetoplastea, including free-living bodonid species (**Figure S1 and Table**
135 **S1** for examples). Surprisingly, we also discovered homologous proteins with high
136 similarity across the entire sequence in other very diverse Euglenozoa species,
137 including the classes Euglenida and Diplonemea, and also in various much more
138 distantly related eukaryotic lineages, particularly within the SAR clade, including
139 Stramenopiles and Alveolata (**Figure 1B, Figure S2 and Table S1** for example).
140 However, no proteins with the same general architecture were identified in the

141 Opisthokonta (the clade that includes fungi and animals) or in plants, the only
142 sequences showing some similarity being restricted, as anticipated, to the well-
143 conserved GTPase domain. Unexpectedly, we also identified several sequences
144 similar to *Tb*MfnL in bacteria, mainly in the PVC group and in Proteobacteria
145 (**Figure 1B, Figure S2 and Table S1** for example). Analysis of several of these
146 proteins showed again a very conserved structural and domain organization along
147 the whole sequence, with the exception of the absence of the potential
148 mitochondrial targeting sequence (MTS) in prokaryotes (**Figure 1B and Figure**
149 **S2**).
150 We conducted a maximum likelihood phylogenetic analysis of the identified
151 sequences, incorporating several DSPs from mammals and yeast, as well as the
152 cyanobacterial homolog DBLP as outgroup sequences (**Figure 1C and Figure S3**).
153 Most eukaryotic sequences branched within a well-supported (99% ultrafast
154 bootstrap support –UFBS-) group. Despite the fact that sequences within this clade
155 tended to group according to their taxonomic origin, we observed several
156 unexpected relationships (e.g., dinoflagellates branched within the Euglenozoa,
157 and cryptophytes and haptophytes within the Stramenopiles). Moreover,
158 colponemids (a group of deep-branching alveolates) formed a fully-supported
159 (100% UFBS) group with two stramenopile sequences. Bacterial sequences formed
160 a paraphyletic group at the base of this main eukaryotic clade, with two
161 ameobozoan species (*Acanthamoeba castellanii* and *Dracoamoeba jomungandri*)
162 robustly branching (97% UFBS) within one of the bacterial subgroups. This
163 unexpected relationship strongly suggested that these amoebae acquired this gene
164 by horizontal gene transfer (HGT) from bacterial donors. By contrast, the
165 anomalous relationships among eukaryotic taxa observed within the main
166 eukaryotic clade were more difficult to explain, although multiple gene duplications
167 and losses appeared to have played a role to shape the current distribution of this
168 gene in eukaryotes. The class Diplonemea provided evidence for this hypothesis,
169 with two highly supported (100% UFBS) groups of sequences of the same genera
170 (*Diplonema*, *Lacrimia*, and *Rhynchopus*) branching paraphyletically at the base of
171 a large clade of dinoflagellate (Alveolata) sequences (**Figure S3**). A small group
172 of sequences containing stramenopile, alveolate, and haptophyte species branched
173 sister to all the other prokaryotic and eukaryotic sequences and most likely
174 represented an ancient paralog of this gene, giving additional evidence for the role
175 of duplication in the evolution of this gene. Furthermore, it is very likely that HGT

176 between different eukaryotic groups also occurred, as in the case of the
177 dinoflagellate sequences cited above, which appear to have acquired this gene
178 from euglenozoan donors, and in the case of the haptophyte and cryptophytes
179 sequences that branched within the large group of stramenopile sequences.
180 Given the specific architecture of this DSP, its large phylogenetic distance to other
181 previously known protein families, and its wide and distinct taxonomic
182 representation in prokaryotes and eukaryotes –but its absence in animals and
183 plants- strongly indicate that it represents a novel DSP associated with membrane
184 dynamics.
185
186 **2 - *Tb*MfnL is localized in the mitochondrion**
187 To determine the subcellular localization of *Tb*MfnL (Tb927.7.2410), we added a
188 10xHA tag at the C-terminal extremity of the endogenous *Tb*MfnL (*Tb*MfnL$_{::10HA}$) in
189 both PCF and BSF trypanosomes (**Figure 2A**). C-terminal tagging was used to
190 avoid disruption of the potential N-terminal MTS. Western blot analysis with anti-
191 HA antibody showed that *Tb*MfnL$_{::10HA}$ is about 2-fold more expressed in PCF than
192 BSF, which is in agreement with the data obtained through SILAC and
193 transcriptomic analysis for this protein [31, 32] (**Figure 2B**). The localization of
194 the *Tb*MfnL protein was studied in PCF by immunofluorescence using threonine
195 dehydrogenase (Tdh, [33]) as a mitochondrial matrix marker (**Figure 2C**).
196 *Tb*MfnL$_{::10HA}$ and Tdh clearly colocalized in the mitochondrial compartment, but
197 *Tb*MfnL depicted a less homogeneous mitochondrial distribution (**Figure 2C,**
198 **Merge**). Unfortunately, we could not use the anti-Tdh immune serum for
199 immunofluorescence analysis on BSF. Consequently, we performed a labeling of
200 the mitochondria, with an anti-HSP60 (mitochondrial maker). Like observed in
201 PCF, *Tb*MfnL$_{::10HA}$ and HSP60 colocalized in the mitochondrial compartment
202 (**Figure 2C, Merge)**. The presence of a N-terminal targeting sequence and its
203 localization by fluorescence microscopy demonstrated that *Tb*MfnL is a
204 mitochondrial protein. These data are consistent with the mitochondrial localization
205 of the C-terminal GFP-tagged *Tb*MfnL reported by the TrypTag database (cellular
206 localization of trypanosome proteins [34]). Of note, the N-terminal GFP-Tagged
207 *Tb*MfnL exhibited a cytoplasmic localization in TrypTag database [34], likely due
208 to masking of the MTS pre-sequence.
209

210 **3 – Inactivation and silencing of *Tb*MfnL does not alter mitochondrial**
211 **shape**
212 Live microscopy of yeasts and cultured mammalian cells has revealed that
213 mitochondrial morphology is continuously remodeled by antagonistic fission and
214 fusion reactions [16, 35]. Under normal conditions, the fusion/fission balance is
215 established in favor of fusion and the mitochondria appear filamentous. Inhibition
216 of fusion leads to mitochondrial fragmentation by ongoing fission [16] and
217 reversely enhancing fusion leads to hyperfused mitochondria with increased
218 branching and interconnection [12].
219 To investigate the role of *Tb*MfnL, we first inactivated the *Tb*MfnL gene by
220 CRISPR/Cas9 [36]. Both *Tb*MfnL alleles were inactivated by integration of a
221 puromycin resistance marker cassette into both PCF and BSF cloned cells (**Figure**
222 **3A**). Cloned parasites were analyzed by PCR to select cell lines carrying puromycin
223 resistance gene insertions in both *Tb*MfnL alleles (*Tb*MfnL$^{-/-}$) (**Figure 3B**). No
224 significant impact on cell growth was observed in these PCF and BSF null-mutants
225 over a period of 7 days compared to parental cells (**Figure S4**) and no significant
226 difference in the structure of the *Tb*MfnL$^{-/-}$ mitochondrion was observed by staining
227 mitochondrion with rhodamine-123 or immunofluorescence analyses with the anti-
228 HSP60 immune serum, in both PCF and BSF mutant cell lines, respectively (**Figure**
229 **3C and 3D**). To confirm that the CRISPR/Cas9 strategy leads to *Tb*MfnL gene
230 inactivation, we repeated this process in a strain endotagged with a C-terminal
231 3xTy1 tag in order to follow the expression of the protein by western blot (**Figure**
232 **S5A-D**) upon insertion of the puromycin resistance gene as above (**Figure S5E-**
233 **G**) and deletion of part of the *Tb*MfnL gene (**Figure S5H-J**), as above. In both
234 cases, the protein was not detected in the inactivated clones and no modification
235 of the mitochondrial structure was observed (**Figure S5G/J)**.
236 In order to detect and quantify discrete modifications of the mitochondrial shape
237 that may escape detection upon qualitative visual analysis, we developed an
238 ImageJ macro (**Data S1**) for automatic quantification of mitochondrial junctions
239 from fluorescence images (**Figure 3C/D/E**). This allowed us to establish that the
240 number of mitochondrial junctions is equivalent in *Tb*MfnL$^{-/-}$ and parental PCF cells
241 (8.5±4.9 vs 9.4±4.3) confirming the qualitative analysis of the microscopy images
242 (**Figure 3C**). The mitochondrial and cristae structures were also examined by
243 transmission electron microscopy (TEM) in *Tb*MfnL$^{-/-}$ PCF cells cultured with either
244 proline or glucose as the sole carbon source. Under these conditions, no significant

245 alterations in mitochondrial or cristae structure were observed, nor were there any
246 noticeable effects on the growth of the mutant cells (**Figure S6**).
247 These findings regarding the consequences of *Tb*MfnL inactivation in PCF and BSF
248 are not in line with a previous report describing a highly fenestrated mitochondrial
249 network consecutive to a partial but significant inhibition (70%) of *Tb*MfnL
250 expression by RNAi in BSF [30]. To exclude that the divergence arose from the
251 different inactivation and silencing strategies, we conditionally down-regulated
252 expression of *Tb*MfnL using a stem-loop RNAi construct. This approach led to a
253 significant reduction (~70%) of the expression of endogenously tagged
254 *Tb*MfnL$_{::10HA}$ in PCF (as observed in BSF [30]), but this was not paralleled by a
255 modification of mitochondrial shape (**Figure S7A-C**). Since mitochondrial
256 fenestration upon *Tb*MfnL silencing was observed in BSF [30], we decided to repeat
257 the experiment using the same strain (*T. brucei* 427 BSF), the same RNAi system
258 (p2T7-177) and the same sequence used for down-regulation [30]. As previously
259 reported [30], we observed a significant reduction of *T*bMfnL expression (~80%
260 after 4 days) of the endogenously tagged *Tb*MfnL$_{::3HA}$ in BSF (**Figure S7D-F**) that
261 was not accompanied by mitochondrial shape modifications (**Figure S7G**). In our
262 hands, neither inactivation nor silencing of *Tb*MfnL alters mitochondrial
263 morphology or induces a fenestration phenotype.
264
265 **4 - *Tb*MfnL overexpression increases mitochondrial branching**
266 We also investigated the possible role of *Tb*MfnL by conditionally overexpressing a
267 C-terminally-tagged (3xTy1) *Tb*MfnL in PCF (^{oe}*Tb*MfnL$_{::3Ty1}$, **Figure 4A**). Expression
268 was confirmed by western blot analysis after 3 to 5 days of tetracycline induction
269 (**Figure 4B**). Rhodamine-123 staining showed that the parental and non-induced
270 ^{oe}*Tb*MfnL$_{::3Ty1}$ cell lines harbor the expected reticulated mitochondrial structure,
271 while the mitochondrion appears significantly more reticulated and branched in the
272 tetracycline-induced ^{oe}*Tb*MfnL$_{::3Ty1}$ cells (**Figure 4C, Figure S8**). After 5 days of
273 induction, the average number of mitochondrial junctions, quantified with the
274 ImageJ macro, appeared more than 2 times higher in induced ^{oe}*Tb*MfnL$_{::3Ty1}$ cells
275 compared to non-induced or parental cells (**Figure 4D**). In order to estimate the
276 level of *Tb*MfnL overexpression achieved in *T. brucei* PCF, we overexpressed
277 *Tb*MfnL$_{::3Ty1}$ in the *Tb*MfnL$_{::3Ty1}$ background, in which the endogenous *Tb*MfnL alleles
278 were 3Ty1-tagged (clone 2A11; **Figure S5A-D**). Western blot analysis with the
279 anti-Ty1 antibodies revealed that expression of *Tb*MfnL$_{::3Ty1}$ is 5.5-times increased

280 in the resulting tetracycline-induced *Tb*MfnL$_{::3Ty1}$/^{oe}*Tb*MfnL$_{::3Ty1}$ compared to the
281 parental *Tb*MfnL$_{::3Ty1}$ clone, which only expressed the endogenously tagged
282 *Tb*MfnL$_{::3Ty1}$ (**Figure S9A**). Overexpression of *Tb*MfnL$_{::3Ty1}$ once again leads to
283 alterations in mitochondrial morphology (**Figure S9B**). It is also noteworthy that
284 the expression of *Tb*MfnL without the C-terminal 3Ty1 tag induced the same
285 phenotype as the tagged *Tb*MfnL, confirming that the phenotype is not due to the
286 use of a C-terminal tag (**Figure S9A/B**). These data clearly demonstrated that
287 overexpression of *Tb*MfnL stimulates inter-mitochondrial connections.
288 To characterize further inter-mitochondrial branching with higher resolution we
289 used serial block face scanning electron microscopy (SBF-SEM), an approach
290 allowing to characterize the overall structure of membranes and organelles within
291 the entire cell volume [18]. With this approach, hundreds of images are collected
292 to perform a 3D reconstruction of the whole cell, as well as spatial organization of
293 the individual organelles within the cell. Four to five parental and ^{oe}*Tb*MfnL$_{::3Ty1}$ PCF
294 cells were reconstructed in 3D, with a particular emphasis on the mitochondrion,
295 the nucleus, the flagellar pocket and the cell outline. We have not been able to
296 correctly identify the kinetoplast DNA on the electron microscopy images.
297 However, since kDNA is in close contact with the flagellar pocket, we have assumed
298 its position. Other organelles (glycosomes, acidocalcisomes, Golgi, flagellum, etc.)
299 are not represented either in order to not overload the 3D representation. As
300 expected, the parental PCF cells showed a reticulated mitochondrion along the
301 whole cell (**Figure 4E**), a rather central nucleus and the flagellar pocket on the
302 posterior side. The length of the parental and ^{oe}*Tb*MfnL$_{::3Ty1}$ cells, varied between
303 20.4±3.3 and 23±4.7 µm, respectively. As observed by fluorescence microscopy,
304 ^{oe}*Tb*MfnL$_{::3Ty1}$ mitochondrion showed more reticulation (**Figure 4E**). Unexpectedly,
305 in some cells this reticulation was even more prominent at the edges of the flagellar
306 pocket, where the kDNA is located, as illustrated in **Figure 4E**, an observation that
307 we had not identified by immunofluorescence microscopy approaches. This hyper-
308 reticulated structure (leaving a few gaps in the mitochondrion) formed a globular
309 structure and probably encapsulated the kDNA (**Figure 4E**). This structure called
310 kDNA pocket has been already described in BSF where kDNA replicates [20], but
311 is even more prominent in the ^{oe}*Tb*MfnL$_{::3Ty1}$ cells. We determined that the
312 mitochondrial volume in PCF cells (4.9 ± 1 µm³, **Figure 4F**) aligns with previous
313 reports (2.5–3 µm³, [2]) and as expected, is nearly twice that of BSF cells (1.1–3
314 µm³, [18, 20]). As anticipated, the mitochondrial volume in ^{oe}*TbMfnL$_{::3Ty1}$* cells is

315 nearly doubled compared to parental cells (8.3 ± 1.9 μm³, **Figure 4F**).
316 Additionally, TEM analysis of the mitochondrial and cristae structures in
317 ^{oe}*Tb*MfnL$_{::3Ty1}$ cells cultured with either proline or glucose as the sole carbon source
318 revealed no significant alterations (**Figure S6**).
319 We also investigated the effect of *Tb*MfnL expression in the BSF trypanosomes,
320 where the mitochondrial compartment is smaller and composed of a shorter and
321 poorly interconnected mitochondrion. Expression of ^{oe}*Tb*MfnL$_{::3Ty1}$ was confirmed
322 by western blot (**Figure 4G**), but unlike in PCF, the mitochondrial structure
323 (labeled here with mitochondrial HSP60) was not altered, remaining tubular like in
324 the parental cells (**Figure 4H**). Induction over a longer period (up to 21 days) did
325 not show mitochondrial alterations.
326
327 **5 - *Tb*MfnL overexpression increases mitochondrial branching in a GTPase**
328 **dependent manner**
329 All dynamin-like proteins possess a GTP-binding domain with highly conserved G1-
330 G4 motifs. They can be inactivated by mutations in the G1 motif that lower the
331 efficiency of GTP-binding and hydrolysis. To determine whether *Tb*MfnL activity
332 requires a functional GTPase domain, the key lysine 141 in the highly conserved
333 G1 motif was converted to alanine (K141A), according to previously characterized
334 GTP-binding domains from other organisms [37-39]. The K141A mutation was
335 introduced into the *Tb*MfnL$_{::3Ty1}$ sequence, which was overexpressed in the PCF
336 ^{oe}*Tb*MfnL-K141A$_{::3Ty1}$ (**Figure 5A**) and *Tb*MfnL$_{::3Ty1}$ PCF backgrounds
337 (*Tb*MfnL$_{::3Ty1}$/^{oe}*Tb*MfnL-K141A$_{::3Ty1}$, **Figure S9**). Expression of *Tb*MfnL-K141A$_{::3Ty1}$
338 was confirmed by western blot analyses after 3 to 5 days of tetracycline induction
339 in the ^{oe}*Tb*MfnL-K141A$_{::3Ty1}$ cell line (**Figure 5B**) and its overexpression was
340 estimated as 3-fold in the *Tb*MfnL$_{::3Ty1}$/^{oe}*Tb*MfnL-K141A$_{::3Ty1}$ mutant compared to
341 the parental *Tb*MfnL$_{::3Ty1}$ clone (**Figure S9A**). *Tb*MfnL-K141A$_{::3Ty1}$ localized to the
342 mitochondria (**Figure 5C**), as expected, but did not alter mitochondrial shape
343 (**Figure 5C/D, Figure S8**) nor the number of mitochondrial junctions (**Figure**
344 **4D**). To exclude the possibility that concentration-dependent effects (due to the
345 twofold lower expression of *Tb*MfnL-K141A$_{::3Ty1}$ compared to the parental
346 *Tb*MfnL$_{::3Ty1}$) might prevent K141A from inducing membrane branching, rather
347 than its inactivated GTPase activity, we equalized the expression levels of wild-
348 type *Tb*MfnL$_{::3Ty1}$ and mutant *Tb*MfnL-K141A$_{::3Ty1}$. The tetracycline concentration
349 used for *Tb*MfnL$_{::3Ty1}$ expression was reduced from 1 μg/ml to 0.05 μg/ml. Under

350 these conditions, both variants displayed comparable expression levels at 3 and 5
351 days (**Figure S10A**); however, hyper-reticulation was observed exclusively in cells
352 overexpressing *Tb*MfnL$_{::3Ty1}$ (**Figure S10B**). This clearly demonstrates that *Tb*MfnL
353 is a dynamin-related protein that relies on a functional GTPase domain to modulate
354 mitochondrial branching in trypanosomes.
355 The mitochondrial localization of ^{oe}*Tb*MfnL$_{::3Ty1}$ and ^{oe}*Tb*MfnL-K141A$_{::3Ty1}$ was also
356 confirmed by electron microscopy and immunogold-labeling using an anti-Ty1
357 antibody. After induction and immunogold-labeling, both proteins are clearly
358 localized in the mitochondrion (**Figure S11A/B-c/d**) as compared to controls with
359 non-induced cells (**Figure S11A/B-a/b**), and confirmed by gold-particles
360 quantification (**Figure S11C**).
361
362 **6 - Submitochondrial localization of *Tb*MfnL**
363 Immunofluorescence analyses showed that ^{oe}*Tb*MfnL$_{::3Ty1}$ co-localized with Tdh
364 (**Figure 6A**), as previously described for the endogenously-tagged *Tb*MfnL$_{::10HA}$
365 (**Figure 2C**). To increase the resolution of *Tb*MfnL localization we performed
366 Ultrastructure Expansion Microscopy (U-ExM), which increases the size of a sample
367 while preserving its ultrastructure [40-42]. Using this approach, we showed that
368 both ^{oe}*Tb*MfnL$_{::3Ty1}$ (**Figure 6B**) and the endogenous *Tb*MfnL$_{::10HA}$ (**Figure 6C**)
369 displayed mitochondrial localization with punctate, non-homogeneous distribution
370 patterns, which differed from the localization of the matrix marker (Tdh). These
371 findings suggest an association of the *Tb*MfnL protein with mitochondrial
372 membranes.
373
374 **7 - Mitochondrial targeting and membrane anchoring of *Tb*MfnL**
375 To investigate the mechanisms ensuring mitochondrial targeting of *Tb*MfnL, we
376 first addressed the two domains that may determine *Tb*MfnL localization: (i) the
377 N-terminal MTS which may facilitate targeting to the inner membrane,
378 intermembrane space and matrix localization, and (ii) the C-proximal/terminal TMs
379 which could mediate membrane anchoring. To investigate their capacity to target
380 proteins to mitochondria, we fused the MTS domain, or the two transmembrane
381 domains of *Tb*MfnL, to GFP. Fusion of the MTS at the N-terminus of GFP ($_{MTS::}$GFP)
382 fully targeted GFP to the mitochondria (**Figure 7A**). Interestingly, western blot
383 analyses showed that $_{MTS::}$GFP and cGFP (cytosolic GFP) have the same apparent
384 size (**Figure 7B**), suggesting that the predicted MTS (**Figure S1**) was indeed

385 cleaved by matrix processing peptidase upon import of $_{MTS::}$GFP across the inner
386 membrane. In the same line, ^{oe}*Tb*MfnL$_{::3Ty1}$ and ^{oe}*Tb*MfnL-K141A$_{::3Ty1}$ showed the
387 same apparent size as ^{oe}*Tb*MfnL-ΔMTS$_{::3Ty1}$ by western blot analyses, suggesting
388 that the MTS is also cleaved in its natural context (**Figure 7C**). In contrast,
389 western blot analyses showed that addition of the two C-proximal TMs at the C-
390 terminal extremity of GFP (GFP$_{::TM}$) induces a size shift (**Figure 7B**).
391 Immunofluorescence analyses revealed that GFP$_{::TM}$ was not targeted to the
392 mitochondrion or cytosol, but instead to others distinct structures (**Figure 7A**).
393 However, it is important to note that this localization could simply represent
394 unspecific membrane-targeting by hydrophobic TMs. This inability of *Tb*MfnL TMs
395 to mediate mitochondrial targeting indicates that they differ from the TMs of other
396 mitofusins, which are responsible for mitochondrial outer membrane localization
397 [43].
398 To confirm the role and relevance of these domains on *Tb*MfnL localization and
399 function, we overexpressed 3Ty1-tagged *Tb*MfnL-mutants without MTS (^{oe}*Tb*MfnL-
400 ΔMTS$_{::3Ty1}$) or without TMs (^{oe}*Tb*MfnL-ΔTM$_{::3Ty1}$) in PCF trypanosomes (**Figure 7D**
401 **and 7G**). Tetracycline-induced overexpression of both recombinant *Tb*MfnL was
402 confirmed by western blot, 3 to 5 days after induction (**Figure 7E/7H, Figure**
403 **S9**). In contrast to ^{oe}*Tb*MfnL$_{::3Ty1}$, ^{oe}*Tb*MfnL-ΔMTS$_{::3Ty1}$ did not colocalize with Tdh
404 revealing that the N-terminal MTS is indeed required for proper mitochondrial
405 targeting of *Tb*MfnL (**Figure 7F**). The MTS is therefore essential for the correct
406 mitochondrial localization of *Tb*MfnL. In addition, overexpression of ^{oe}*Tb*MfnL-
407 ΔMTS$_{::3Ty1}$ did not alter the mitochondrial structure, indicating that its proper, MTS-
408 mediated, mitochondrial localization is essential for *Tb*MfnL-function (**Figure**
409 **7F/Anti-Tdh, Figure S9**). Overexpression of a *Tb*MfnL truncated version missing
410 the C-proximal TMs (^{oe}*Tb*MfnL-ΔTM$_{::3Ty1}$, **Figure 7G-H, Figure S9**) did not affect
411 its mitochondrial localization (**Figure 7I**), which confirms that the N-terminal MTS
412 sequence was sufficient for mitochondrial targeting of *Tb*MfnL. However, in
413 contrast to full length *Tb*MfnL (**Figures 4C and 6A/B**), *Tb*MfnL lacking TMs did
414 not induce a modification of the mitochondrial shape (**Figure 7I, Figure S9**),
415 demonstrating that the transmembrane domains are required for proper function.
416 Altogether, our data showed that *Tb*MfnL is targeted to the mitochondrion via an
417 N-terminal MTS and that C-proximal TMs are required for the cellular function of
418 *Tb*MfnL.

419 Finally, we investigated the precise localization of *Tb*MfnL$_{::3Ty1}$ and its variants
420 (*Tb*MfnL-ΔTM$_{::3Ty1}$ and *Tb*MfnL-ΔMTS$_{::3Ty1}$) in the clone 2A11, where the
421 endogenous *Tb*MfnL alleles were tagged with 3Ty1 (**Figure S5A-D**). This was
422 achieved using a protease protection assay, a method previously used to
423 determine the submitochondrial localization of various mitochondrial proteins in
424 trypanosomes [44, 45]. Mitochondria are enriched by differential centrifugation,
425 converted into mitoplasts by digitonin-mediated permeabilization of the outer
426 membrane and finally incubated with proteinase K in the presence or absence of
427 Triton X-100 to permeabilize the inner membrane.
428 Western blot analysis revealed that the cytosolic protein Enolase was almost
429 entirely recovered in the supernatant, confirming that the generation of mitoplasts
430 had effectively released cytosolic components (**Figure 8A, Figure S12**). In
431 contrast, the *Tb*MfnL$_{::3Ty1}$ protein and its variants exhibited fractionation patterns
432 consistent with those of mitochondrial proteins, such as Atom40, Prohibitin, and
433 Tdh, which serve as markers for the outer mitochondrial membrane (OMM), inner
434 mitochondrial membrane (IMM, facing the intermembrane space), and
435 mitochondrial matrix, respectively (**Figure 8A/C, Figure S12**). Proteinase K
436 treatment of mitoplasts led to the near-complete digestion of outer membrane
437 Atom40, intermembrane space Prohibitin (bound to the inner membrane), and
438 *Tb*MfnL-ΔMTS$_{::3Ty1}$, which is no longer targeted to the mitochondrion and thus
439 unprotected. In contrast, the size and levels of *Tb*MfnL$_{::3Ty1}$, *Tb*MfnL-ΔTM$_{::3Ty1}$ and
440 Tdh remained unaffected, indicating protease protection by the inner membrane.
441 The intact state of Tdh further confirmed the integrity of the mitochondrial inner
442 membrane and the reliability of the assay (**Figure 8A/C, Figure S12**). Digestion
443 of the OMM-embedded β-barrel protein Atom40 and IMS Prohibitin, along with the
444 preservation of *Tb*MfnL$_{::3Ty1}$ and *Tb*MfnL-ΔTM$_{::3Ty1}$, suggests that *Tb*MfnL faces the
445 matrix and is protected by the inner membrane. The addition of Triton X-100,
446 which disrupts membrane integrity, exposed matrix proteins to proteinase K,
447 resulting in the degradation of *Tb*MfnL$_{::3Ty1}$, *Tb*MfnL-ΔTM$_{::3Ty1}$, and Tdh, thereby
448 confirming their localization and orientation on the matrix side (**Figure 8A/C,**
449 **Figure S12**). It should be noted that western blot revealed a size difference
450 between the full-length *Tb*MfnL$_{::3Ty1}$ and *Tb*MfnL-ΔTM$_{::3Ty1}$. Specifically, we
451 observed two bands: the upper band corresponding to the endogenously tagged
452 protein and the lower band representing to the overexpressed *Tb*MfnL-ΔTM$_{::3Ty1}$
453 protein.

454 To further investigate the localization of *Tb*MfnL, we separated the membrane and
455 matrix fractions by performing repeated freeze-thaw lysis on mitoplast
456 preparations. The membrane fraction was further divided into integral and
457 peripheral fractions via carbonate extraction. *Tb*MfnL$_{::3Ty1}$ and *Tb*MfnL-ΔTM$_{::3Ty1}$
458 were analyzed alongside control proteins, Tdh (matrix-localized) and Prohibitin
459 (inner membrane, IMS oriented). As expected, *Tb*MfnL$_{::3Ty1}$ was exclusively
460 retained in the membrane fraction, whereas *Tb*MfnL-ΔTM$_{::3Ty1}$, lacking its
461 transmembrane domains, was released from membrane (**Figure 8B/C, Figure**
462 **S12**). These data are consistent with a recent analysis of the mitochondrial
463 proteome, which proposed that the *Tb*MfnL protein is located in the inner
464 mitochondrial membrane [46].
465 Interestingly, structural predictions of *Tb*MfnL using Alphafold, supported by a very
466 high pLDDT score (**Figure S13**), suggest that the two previously identified
467 transmembrane domains form a loop. This loop may act as an anchor within the
468 inner membrane, thereby orientating the protein towards the matrix (**Figure 8C**),
469 consistent with the findings from proteinase K assay and carbonate extraction.

470 **DISCUSSION**

471 Membrane fusion and fission are often controlled by proteins of the dynamin
472 superfamily (DSP) [47, 48]. These proteins consistently have a GTPase domain
473 and contain domains required for membrane binding and oligomerization. In
474 trypanosomes, only DSPs involved in fission have been characterized, and no
475 fusion proteins similar to those of yeasts and mammals (Mfn and Opa1) have been
476 identified so far. This may suggest that trypanosome mitochondria fuse via a
477 machinery that differs from that characterized in yeasts and mammals. We have
478 identified a novel DSP, named Mfn-Like (MfnL), which first representative
479 characterized from the protozoan parasite *T. brucei* (*Tb*MfnL). We dit not establish
480 a direct role in fusion, but demonstrated that it is able to increase mitochondrial
481 interconnectivity in a GTPase-dependent manner, as previously reported for fusion
482 factors Mfn/Opa1 [43, 49]. Interestingly, *Tb*MfnL domain organization and sub-
483 mitochondrial localization differ significantly from that of Mfn and Opa1, suggesting
484 that *Tb*MfnL and possibly other MfnL members mediate and/or enhance membrane
485 branching and interconnection through a different molecular mechanism.

486 As observed for trypanosomes, many organisms including plants, lack genes
487 encoding protein similar to known fusion factors. Interestingly, the search for
488 homologous sequences to *Tb*MfnL allowed us to identify close DSP homologs in
489 several eukaryotic phyla lacking Mfn and Opa1. These new DSPs are widely
490 distributed in eukaryotes, which suggests that they represent an ancient protein
491 family. Most of these phyla belong to the Diphoda, which together with the
492 Opimoda are the two major supergroups of eukaryotes based on the most accepted
493 position of the root of the tree of eukaryotes [50]. The only opimodan sequences
494 found were the two amoeba cited above, most likely representing HGTs from
495 bacteria, and the malawimonad *Gefionella okellyi* (**Figure 1C and Figure S3**).
496 This malawimonad sequence may also reflect an HGT acquisition, in this case from
497 a diphodan ancestor. The taxonomic distribution of this protein and its phylogeny
498 support that it was ancestral at least in Diphoda. However, its presence also in
499 bacteria, with any clear evidence of an HGT-mediated eukaryotic origin of the
500 bacterial sequences, opens the possibility for an even more ancient origin before
501 the diversification of Diphoda and Opimoda, which would imply a massive loss in
502 opimodan taxa except in a few ones such as *Gefionella*. Future analysis of other
503 deep-branching opimodan taxa will help to test this hypothesis. Homologs of
504 *Tb*MfnL were also identified in several bacterial phyla, suggesting the existence in

505 these organisms of a novel machinery involved in membrane shaping and/or
506 remodeling that is different from the one found in yeasts and mammals. While
507 studies of yeast and mammalian DSPs provide information about their functions
508 and structures, little is known about bacterial DSPs, especially their cellular role.
509 Indeed, some bacterial DSPs have been associated with a variety of processes
510 involving membranes *in vivo*, such as a surveillance mechanism for membrane
511 punctures caused by antibiotics and bacteriophages [51, 52], membrane vesicle
512 formation [53] or cytokinesis by promoting membrane curvature at the septum
513 [54, 55]. In addition, studies of the *Bacillus subtilis* DSP DynA have shown that
514 this protein can promote membrane fusion *in vitro* [56]. The mechanism by which
515 the fusion operates is not yet known, but bacterial DSPs are probably recruited to
516 the sites where membrane fusion is needed [55, 57]. Interestingly, structural
517 analysis of *Campylobacter jejuni* DLP1/DLP2 proteins allowed to propose a
518 mechanism explaining how these proteins attach and bind distant and opposing
519 membranes [58]. Unfortunately, the cellular function of *C. jejuni* DLP1/DLP2 is
520 currently unknown. DSPs identified in this study have not yet been characterized
521 and no information on their localization and function is available. However, among
522 the identified organisms, we found bacteria of the phylum Planctomycetes, which
523 are unusual organisms. Indeed, these bacteria contain a compartmentalized
524 cytosol, separated by an intracytoplasmic membrane [59], in some cases
525 surrounding the DNA [60] or forming an anammoxosome, a membrane-bound
526 organelle responsible for the production of energy [61, 62]. It is then conceivable
527 that the identified protein in Planctomycetes (*Pb*DBF, **Figure 1 and S2**) is involved
528 in membrane structuring.
529 The role of *Tb*MfnL in mitochondrial shaping was observed by its overexpression in
530 PCF trypanosomes, which induced a very strong increase in number of connections
531 in the single branched mitochondrion. Moreover, the inactivation of its GTPase
532 domain via mutation of the G1 motif also confirms its belonging to the large family
533 of dynamins. Interestingly, a link between hyperconnection of a branching network
534 and increased fusion processes has been reported in a highly different biological
535 system, filamentous fungi, which grow as interconnected branching networks [63].
536 This raises the intriguing possibility that an excess of *Tb*MfnL in PCF trypanosomes
537 enhances the interconnectivity of mitochondrial networks by inducing
538 mitochondrial fusion.

539 The absence of fragmentation observed upon partial or total inactivation of *Tb*MfnL
540 expression is in agreement with the absence or a very low level of constitutive
541 mitochondrial fission. In contrast, in mammals and yeast, inhibition of fusion
542 results in mitochondrial fragmentation by constitutive fission [16, 64]. Thus, our
543 results are in agreement with previous studies suggesting that fission only occurs
544 during cell division [19, 28]. The lack of observable mitochondrial alterations may
545 also be attributed to the involvement of other proteins in mitochondrial structuring,
546 as suggested by studies on the mitochondrial outer membrane proteome in *T.*
547 *brucei* [65, 66] and the presence of mitochondrial complexes such as the recently
548 characterized MICOS [44]. Additionally, subtle changes in mitochondrial structure
549 may exist but could have gone undetected using our current approaches. It is
550 worth noting that *Tb*MfnL seems to participate in a unique membrane-structuring
551 mechanism, and its inactivation may not produce effects similar to those observed
552 for Mfn or Opa1.
553 Another intriguing point was the discrepancy with the results reported by
554 Vanwalleghem et al. [30]. Indeed, they describe fenestration of the mitochondrion
555 in BSF cells with down-regulated *Tb*MfnL, whereas in our studies, involving
556 inactivation by CRISPR/Cas9 or down-regulation by RNAi in BSF cells, we did not
557 observe any alterations in mitochondrial structure. The only modification (hyper-
558 reticulation) of the mitochondrial structure was observed exclusively during the
559 overexpression of *Tb*MfnL and only in PCF forms. This discrepancy may arise from
560 differences in cell lines, culturing conditions, sample preparation methods, or
561 mitochondrial staining protocols. We used rhodamine staining on live cells and
562 immunofluorescence labeling to visualize the mitochondrial network, whereas
563 Vanwalleghem et al. [30] employed FIB-SEM tomography. It is also possible that
564 *Tb*MfnL knockdown affects mitochondrial import, since disruptions in mitochondrial
565 import have been reported to influence mitochondrial structure [65].
566 Using several microscopy approaches, we have demonstrated that *Tb*MfnL is
567 localized within the mitochondrial membranes, with two domains involved in its
568 accurate mitochondrial addressing, a canonical N-terminal MTS and two adjacent
569 C-terminal transmembrane domains. Expression of MTS-less *Tb*MfnL or MTS-GFP
570 recombinant proteins in PCF trypanosomes confirmed the role of this 41 aa-long
571 MTS for mitochondrial import. Proteins with an N-terminal MTS are typically
572 imported into the mitochondrial matrix, with a few exceptions, such as Opa1 and
573 Apoptosis-inducing factor (AIF) face the intermembrane space [67]. Indeed, Opa1

574 and AIF localize mainly to the IMS due to their TM domains located in close
575 proximity to the MTS (**Figure 1A**), interrupting transport across the inner
576 membrane. The C-proximal localization of the transmembrane domains of *Tb*MfnL
577 is not compatible with such import interruption, but more presumably suggested
578 that its C-terminus is also exposed to the matrix, as predicted by Alphafold (**Figure**
579 **8C**). This model is consistent with the proteinase K resistance of *Tb*MfnL in
580 mitoplasts. This orientation is also probably similar to that of the prokaryotic MfnLs
581 identified in this study, which could also be anchored in the plasma membrane and
582 orientated towards the cytosol. Interestingly, recent publications describe
583 mitochondrial remodeling originating from the matrix side of the mitochondria.
584 Sheikh *et al.* [68] demonstrated that expressing a potential DSP from a giant virus
585 in *T. brucei* PCF significantly affects mitochondrial morphology within the matrix,
586 with a notable association with the inner membrane. Additionally, Kumar *et al.*
587 [69, 70] showed that a dynamin superfamily-like pseudoenzyme, a distant relative
588 of the dynamin superfamily, stabilizes cristae architecture through interactions on
589 the matrix side of the mitochondrial inner membrane. This contrasts with the mode
590 of action of human or yeast mitofusins, which are involved in the remodeling of
591 mitochondrial outer and inner membranes, but never via the matrix side.
592 In conclusion, the data presented here uncover a new family of DSPs and suggest
593 the existence of a novel membrane-structuring mechanism found in both
594 eukaryotes and prokaryotes, but distinct from those involved in mitochondrial
595 membrane fusion in mammals and fungi.
596

ACKNOWLEDGMENTS AND FUNDING SOURCES

We thank Hassan Hashimi (University of South Bohemia) for providing us the anti-Prohibitin antibody, André Schneider (University of Bern) for providing us the anti-Atom40 antibody, Keith Gull (University of Manchester) for providing us the anti-Ty1 antibody and Derrick Robinson, Mélanie Bonhivers, Elina Casas and Nicolas Landrein (University of Bordeaux) for the pPOTv7 expression vector and extremely valuable help in the expansion microscopy experiment. Cell sorter analyses were performed at the TBMCore facility (FACSility) on BD FACSAria™ III Sorter and we thank Atika Zouine for data acquisition and interpretation. We also thanks Bordeaux Imaging Center (BIC), which is a member of the FranceBioImaging national infrastructure (ANR10-INBS-04), for helping us to design the ImageJ macro and microscopy acquisitions. The Bringaud team is supported by the Centre National de la Recherche Scientifique (CNRS, https://www.cnrs.fr/), the Université de Bordeaux (https://www.u-bordeaux.fr/) and the Agence Nationale de la Recherche (ANR, https://anr.fr/) through the ParaFrap "Laboratoire d'Excellence" (LabEx, https://www.enseignementsup-recherche.gouv.fr/cid51355/laboratoires-d-excellence.html) (ANR-11-LABX-0024). This work was supported by the "Fondation pour la Recherche Médicale" (FRM, https://www.frm.org/) ("Equipe FRM", grant n°EQU201903007845) and the ANR grant ADIPOTRYP (ANR19-CE15-0004-01) to FB and the ERC Advanced grant 787904 to D.M. Portions of this manuscript were based on Dr. Morel's thesis defended at the University of Bordeaux.

AUTHOR CONTRIBUTIONS

C.A.M. conceptualized the study, performed experiments, contributed to analysis and writing. C.A. performed experiments and contributed to analysis. D.M. performed all the phylogenic analysis. C.B., B.S. and E.G. performed the EM and SBF-SEM experiments and contributed to their analysis. S.D-C., M.R., F.B. and E.T. conceptualized the study, contributed to analysis and wrote the manuscript, with also an input from all the authors.

COMPETING INTEREST STATEMENT

The authors declare no competing interest.

632 **FIGURE LEGENDS**

633

634 **Figure 1 - Sequences homologous to *Tb*MfnL and domain organization of**
635 **the proteins. (A)** Structure comparison between mitochondrial dynamin-
636 superfamily proteins (DSPs): *T. brucei Tb*MfnL, human mitofusin 1 or 2
637 (*Hs*Mfn1/2), yeast Fzo1 (*Sc*Fzo1) and human Opa1 (*Hs*Opa1). MTS, predicted
638 mitochondrial targeting sequence; CC, coiled coil region; green box, GTPase
639 domain with the four GTP-binding motifs in yellow; TM, transmembrane span; BSE,
640 bundle signaling element; Stalk domain; Paddle domain. Two TM domains were
641 initially proposed for Mfn1/2, but recently, Mattie et al. (2018) [71] reported the
642 presence of only a single TM domain, with the C-terminus extending into the IMS.
643 This contrasts with Fzo1 and *Tb*MfnL, which are proposed to have a U-shaped
644 structure. Therefore, we have indicated this as TM? in the figure. Structure
645 predictions were performed using PSIPRED [72]. More details and sequence
646 alignment are shown in **Figure S2**. **(B)** Domain organization of several identified
647 proteins from various organisms. MTS, predicted mitochondrial targeting
648 sequence; CC, coiled-coil region; green box, GTPase domain with the four GTP-
649 binding motifs in yellow; TM, transmembrane span; Structure predictions were
650 performed using PSIPRED. More details and sequence alignment are shown in
651 **Figure S2**. *Tb*MfnL, *Trypanosoma brucei* (ID: Tb927.7.2410); *El*MfnL, *Euglena*
652 *longa* (ID: EP00668_Euglena_longa_P029018); *Dp*MfnL, *Diplonema papillatum*
653 (ID: KAJ9468802.1); *Pg*MfnL, *Polarella glacialis* (ID: CAE8737761.1); *Ah*MfnL,
654 *Achlya hypogyna* (ID: OQR970001); *Ct*MfnL, *Chaetoceros tenuissimus* (ID:
655 GFH50037.1); *Hf*MfnL, *Hondaea fermentalgiana* (ID: GBG23909.1); *Cht*MfnL,
656 *Chrysochromulina tobinii* (ID: KOO35358.1); *Pb*MfnL, *Planctomycetaceae*
657 *bacterium* (ID: MBV8881356.1); *Ps*MfnL, *Pedosphaera* sp. (ID: MCH2381658.1);
658 *Rc*MfnL, *Rubrimonas cliftonensis* (ID: WP_093253540.1); *Gp*MfnL,
659 *Gammaproteobacteria* bacterium (ID: RTZ59088.1); *Mb*MfnL, *Myxococcales*
660 bacterium (ID: MCA9558847.1); *Ld*MfnL, *Lentisphaerae* bacterium (ID:
661 NLB69313.1); *Kb*MfnL, *Kiritimatiellae* bacterium (ID: MBO7223041.1). The
662 accession number for *Euglena longa* was obtained from Eukprot V3 web site. **(C)**
663 Maximum likelihood phylogenetic tree of eukaryotic and prokaryotic DSPs. The
664 tree was reconstructed using the LG+C60+G4 model of sequence evolution.
665 Ultrafast bootstrap support values are shown on each branch. Taxa are colored

666 according to their taxonomic affiliation. Groups of sequences belonging to the
667 same phylum are collapsed (see **Figure S3** for the complete tree).
668
669 **Figure 2 - Subcellular localization of *Tb*MfnL. (A)** Schematic representation
670 of *Tb*MfnL endogenously tagged at its C-terminus extremity with 10xHA. Only one
671 of the two alleles is tagged. **(B)** Western blotting of whole-cell extracts ($5x10^6$
672 cells) of *T. brucei* PCF or BSF wild-type cells and PCF or BSF cells expressing
673 *Tb*MfnL$_{::10HA}$ revealed with an anti-HA antibody. It should be noted that Enolase
674 used as a loading control is about 3 to 4 times more expressed in BSF than in PCF
675 according to Hannaert *et al*. 2003 [73]. **(C)** Subcellular localization of *Tb*MfnL$_{::10HA}$
676 in PCF and BSF. Colocalization of *Tb*MfnL$_{::10HA}$ (anti-HA antibody) with matrix
677 mitochondrial threonine dehydrogenase for PCF (Anti-Tdh) and mitochondrial
678 HSP60 for BSF (Anti-HSP60) analyzed by standard immunofluorescence. n,
679 nucleus; k, kinetoplast. The scale bar represents 5 µm.
680
681 **Figure 3 - Inactivation of the *Tb*MfnL gene. (A)** Schematic representation of
682 *Tb*MfnL inactivation by insertion of the puromycine resistant marker (PAC). **(B)**
683 PCR confirmation of *Tb*MfnL gene inactivation on both alleles in BSF and PCF. **(C)**
684 The mitochondrial shape of living parental (WT) and *Tb*MfnL$^{-/-}$ PCF cells (right
685 panel) were designed by an ImageJ macro (Mitochondrial Junctions) from
686 rhodamine 123 staining (left panel). **(D)** Antibody directed against HSP60 was
687 used to label and visualized mitochondrial shape in BSF cells. Top panel: BSF
688 parental cell (WT); bottom panel: BSF *Tb*MfnL$^{-/-}$ cell. n, nucleus; k, kinetoplast.
689 **(E)** Corresponding mitochondrial junctions' quantification. Small red circles in the
690 skeleton image indicate the junctions where three tubules converge. The scale bar
691 represents 5 µm. Statistic: t test - Confidence interval 95% - P-value style: 0.1234
692 (ns); 0.0332 (*); 0.0021 (**); 0.0002 (***); <0.0001 (****).
693
694 **Figure 4 - Overexpression of *Tb*MfnL and GTPase mutant. (A)** Schematic
695 representation of the overexpressing *Tb*MfnL protein tagged with 3Ty1 peptide at
696 the C-terminus of the protein (^{oe}*Tb*MfnL$_{::3Ty1}$). **(B)** Western blotting of whole-cell
697 extracts of *T. brucei* PCF cells overexpressing *Tb*MfnL$_{::3Ty1}$. Non-induced (-Tet) and
698 induced (+Tet) cells after 3 to 5 days (d3 and d5) were revealed with an anti-Ty1
699 antibody. Antibody directed against Enolase protein was used as loading control.
700 **(C)** Mitochondrial structure analysis using rhodamine 123 staining on living cells;

701 mitochondrial structure of PCF parental (WT) and PCF ^{oe}*Tb*MfnL$_{::3Ty1}$ cells before (-
702 Tet) and 5 days after (+Tet) tetracycline induction. **(D)** Quantification of
703 mitochondrial junctions' number using Rhodamine 123 microscopy images.
704 Mitochondrial junctions number: WT, 9.4 ± 4.3; -Tet ^{oe}*Tb*MfnL$_{::3Ty1}$ 8.7 ± 3.6; +Tet
705 ^{oe}*Tb*MfnL$_{::3Ty1}$ 20.4 ± 8.9; -Tet ^{oe}*Tb*MfnL-K141A$_{::3Ty1}$ 8.6 ± 4.8 and +Tet ^{oe}*Tb*MfnL-
706 K141A$_{::3Ty1}$ 10 ± 5.2. **(E)** Surface rendering of segmented PCF using SBF-SEM.
707 Surface rendering of segmented PCF WT and ^{oe}*Tb*MfnL cells, with ^{e}*Tb*MfnL induced
708 by tetracycline for 5 days, showing the cell body (transparent), nucleus (blue),
709 mitochondrion (green), and flagellar pocket (red). 5 WT and 4 ^{oe}*Tb*MfnL cells were
710 analyzed. A magnified view of the upper images, enclosed in a box, was shown.
711 Small white arrows mark the mitochondria-free areas within the mitochondrial
712 network. **(F)** Determination of mitochondrial volume (μm^3) in both WT and
713 ^{oe}*Tb*MfnL cells; WT 4.9±1 and ^{oe}*Tb*MfnL 8.3±1.9. Statistic: t test - Confidence
714 interval 95% - P-value style: 0.1234 (ns); 0.0332 (*); 0.0021 (**); 0.0002 (***);
715 <0.0001 (****). **(G)** Western blotting of whole-cell extracts of *T. brucei* BSF
716 overexpressing *Tb*MfnL$_{::3Ty1}$ cells. Non-induced (-Tet) and induced (+Tet) cells after
717 3 to 7 days (d3, d5 and d7) were revealed with an anti-Ty1 antibody. Antibody
718 directed against Enolase protein was used as loading control. **(H)** Subcellular
719 localization of ^{oe}*Tb*MfnL$_{::3Ty1}$ in BSF by immunofluorescence. Antibody directed
720 against HSP60 was used to label and visualized mitochondrial shape in parental
721 (WT) and *Tb*MfnL$_{::3Ty1}$ overexpressing cells. n, nucleus; k, kinetoplast. The scale
722 bar represents 5 μm.
723
724 **Figure 5 - Overexpression of GTPase mutant(A)** Schematic representation of
725 the overexpressing *Tb*MfnL-K141A$_{::3Ty1}$ mutant protein tagged with 3Ty1 peptide
726 at the C-terminus of the protein (^{oe}*Tb*MfnL-K141A$_{::3Ty1}$). **(B)** Western blotting of
727 whole-cell extracts of *T. brucei* PCF overexpressing *Tb*MfnL-K141A$_{::3Ty1}$ cells; (-Tet)
728 non-induced and (+Tet) induced cells for 3 or 5 days (d3 and d5). Antibody
729 directed against glycosomal Fumarate reductase protein (Frdg) was used as
730 loading control. **(C)** Submitochondrial localization of ^{oe}*Tb*MfnL-K141A$_{::3Ty1}$ in PCF
731 by immunofluorescence; Colocalization of ^{oe}*Tb*MfnL-K141A$_{::3Ty1}$ (anti-Ty1) with
732 matrix mitochondrial Threonine dehydrogenase (Anti-Tdh) was analyzed by
733 standard immunofluorescence, after 5 days induction (d5+Tet). n, nucleus; k,
734 kinetoplast. **(D)** Mitochondrial structure analysis using rhodamine 123 staining on
735 living cells; mitochondrial structure of PCF parental (WT) and PCF ^{oe}*Tb*MfnL-

736 K141A$_{::3Ty1}$ cells before (-Tet) and 5 days after (+Tet) tetracycline induction. The
737 scale bar represents 5 µm.
738
739 **Figure 6 – Submitochondrial localization of *Tb*MfnL.** Subcellular localization
740 of ^{oe}*Tb*MfnL$_{::3Ty1}$ in PCF by immunofluorescence and Ultra Expansion Microscopy
741 (UExM); Colocalization of ^{oe}*Tb*MfnL$_{::3Ty1}$ (anti-Ty1) with matrix mitochondrial
742 Threonine dehydrogenase (Anti-Tdh) was analyzed by standard
743 immunofluorescence **(A)** and by UExM with an expansion factor of ~4.4 **(B)**, after
744 5 days induction (d5+Tet). **(C)** Subcellular localization of ^{oe}*Tb*MfnL$_{::10HA}$ in PCF
745 analyzed by UExM. n, nucleus; k, kinetoplast. The scale bar represents 5 µm.
746
747 **Figure 7 - Role of *Tb*MfnL domains. (A)** Localization of the GFP according to
748 the different tags fused. Colocalization of GFP with the mitochondrial matrix
749 marker threonine dehydrogenase (Anti-Tdh) was assessed by standard
750 immunofluorescence after 5 days of tetracycline induction for MTS$_{::GFP}$ and GFP$_{::TM}$.
751 The "c" in cGFP stands for constitutive expression, resulting in the cytosolic
752 localization of GFP. MTS, mitochondrial targeting signal; TM, transmembrane
753 domains. **(B)** Western blot analysis of GFP expression. cGFP, constitutive and
754 cytosolic GFP. Non-induced (-Tet) and induced (+Tet) cells after 5 days. **(C)**
755 *Tb*MfnL size analysis by western blot using anti-Ty1 antibody. **(D)** Schematic
756 representation of N-terminus truncated *Tb*MfnL protein (first 41 amino acids)
757 tagged with 3Ty1 peptide at the C-terminus of the protein (^{oe}*Tb*MfnL-ΔMTS$_{::3Ty1}$).
758 **(E)** Western blotting of whole-cell extracts of *T. brucei* PCF overexpressing
759 *Tb*MfnL-ΔMTS$_{::3Ty1}$ cells; (-Tet) non-induced and (+Tet) induced cells for 3 or 5
760 days. **(F)** Subcellular localization of ^{oe}*Tb*MfnL-ΔMTS$_{::3Ty1}$ in PCF after 5 days
761 induction. Colocalization of ^{oe}*Tb*MfnL-ΔMTS$_{::3Ty1}$ (anti-Ty1) with matrix
762 mitochondrial Threonine dehydrogenase (Anti-Tdh) analyzed by standard
763 immunofluorescence. **(G)** Schematic representation of truncated transmembrane
764 domains of *Tb*MfnL protein (45 amino acids) tagged with 3Ty1 peptide at the C-
765 terminus of the protein (^{oe}*Tb*MfnL-ΔTM$_{::3Ty1}$). **(H)** Western blotting of whole-cell
766 extracts of *T. brucei* PCF overexpressing *Tb*MfnL-ΔTM$_{::3Ty1}$ cells; (-Tet) non-induced
767 and (+Tet) induced cells for 3 days. **(I)** Subcellular localization of ^{oe}*Tb*MfnL-
768 ΔTM$_{::3Ty1}$ in PCF after 3 days induction, analyzed by standard immunofluorescence.
769 n, nucleus; k, kinetoplast. The scale bar represents 5 µm.
770

771 **Figure 8 – Membrane topology of *Tb*MfnL. (A**) The Proteinase K protection
772 assay involved incubating mitoplasts with Proteinase K and Triton X100, as
773 denoted by the "+" symbol. TF represents the total fraction containing both
774 cytoplasmic and membrane components; S denotes the supernatant, comprising
775 the cytosolic contents; and Pellet represents the organelle fraction. **(B)** Carbonate
776 extraction of mitochondria isolated from ^{oe}*Tb*MfnL$_{::3Ty1}$ and ^{oe}*Tb*MfnL-ΔTM$_{::3Ty1}$ cells.
777 Mem, membrane fraction; Matrix, matrix fraction; Int. Mem, integral membrane
778 fraction; Per. Mem, peripheral membrane fraction. **(C)** Predicted structure of
779 *Tb*MfnL, from AlphaFold protein structure database. *Tb*MfnL was embedded in
780 mitochondrial inner membrane (IMM). The color coding corresponds to the
781 predicted secondary structure depicted on the top of the figure. The first 41 N-
782 terminal amino acids corresponding to the MTS are not shown as they are cleaved.
783 The N- and C-termini are marked by small black spheres. The AlphaFold model
784 score of *Tb*MfnL is between confident to very high for most of the structured
785 domains (https://alpha- fold.ebi.ac.uk/entry/Q57XN3, **Figure S13**).

786 **MATERIALS AND METHODS**

787

788 **Trypanosomes and cell cultures**

789 The PCF of *T. brucei* EATRO1125.T7T (TetR-HYG-T7RNAPOL-NEO, where TetR
790 stands for tetracycline resistance, HYG for hygromycin, T7RNAPOL for RNA
791 polymerase T7, and NEO for neomycin) was cultured at 27°C with 5% CO_2 in
792 SDM79 medium containing 10% (vol/vol) heat-inactivated fetal calf serum, 5
793 µg/ml hemin, 25 µg/ml hygromycin and 10 µg/mL neomycin. PCF cells were also
794 cultured in SDM80 medium containing either glucose (10 mM) as the sole carbon
795 source or proline (5 mM) supplemented with N-acetyl-glucosamine (50 mM) to
796 inhibit the glucose transporter. The bloodstream form of *T. brucei* 427 90-13
797 (TetR-HYG-T7RNAPOLNEO) was cultured at 37°C with 5% CO_2 in Iscove's modified
798 Dulbecco's medium (IMDM) supplemented with 10% (vol/vol) heat-inactivated
799 fetal calf serum, 0.2 mM β-mercaptoethanol, 36 mM $NaHCO_3$, 1 mM hypoxanthine,
800 0.16 mM thymidine, 1 mM sodium pyruvate, 0.05 mM bathocuproine, 1.5 mM L-
801 cysteine [74], 5 µg/ml hygromycin and 2.5 µg/mL neomycin. Overexpression cell
802 lines were induced with tetracycline (10 µg/mL for BSF and 1 µg/mL for PCF).
803 Growth was monitored by daily cell counting with the cytometer Guava® Muse®
804 and Guava® easyCyte™.

805 **Endogenous tagging and inactivation of *Tb*MfnL by CRISPR-Cas9**

806 Endogenous tagging and inactivation of *Tb*MfnL were achieved by CRISPR Cas9
807 technology [36]. Briefly, inactivation of the *Tb*MfnL was achieved by inserting the
808 resistant marker puromycin (Pac) or a small sequence encoding for a *Bam*HI
809 restriction site plus 6 successive stop codons, flanked by 50 bp homologous to the
810 5' and 3' *Tb*MfnL sequences from the Cas9 cutting site. Similar approaches have
811 been performed for endogenous tagging with the insertion of a sequence encoding
812 3xTy1 or 3xHA. The EATRO1125.T7T PCF and the 427 90.13 BSF ($1x10^6$ cells)
813 were respectively transfected, using Amaxa nucleofectorII, with 1 µg of purified
814 cassette (puromycin resistance marker, Stop*Bam*H1Stop, 3xTy1 or 3xHA), 30 µg
815 Cas9 protein from IDT and pre-annealing TracrRNA (0.4 µmol) and gRNA (0.4
816 µmol). Cells were transfected using program X-001 and selected or not with
817 puromycin (SDM79, 1 µg/mL, or IMDM 0.1 µg)/mL). Cells were cloned by using a
818 cell sorter (TBM Core facility), and selection of double inactivated *Tb*MfnL gene
819 (*Tb*MfnL$^{-/-}$) or endogenously tagged clones was done by DNA extraction, with
820 NucleoSpin Blood (Macherey-Nagel) and PCR amplification, see supplemental

821 **Table S2**. Guide RNAs were designed using EuPaGDT, from http://tritrypdb.org.
822 Primers and guide RNAs used were synthetized by Integrated DNA Technologies
823 (IDT) and are listed in supplemental **Table S2**.

824 **Immunofluorescence**

825 Cells were washed twice with PBS, then fixed with 2% paraformaldehyde (PFA) for
826 10 min at room temperature and 0.1mM glycine was added 10 min to stop the
827 reaction. The cells were spread on slides and permeabilized with 0.05% triton X-
828 100. After incubation in PBS containing 4% bovine serum albumin (BSA) 20 min,
829 cells were incubated for 1 hour with primary antibodies diluted in PBS-BSA 4%,
830 washed 4 times with PBS and incubated for 45 min with secondary antibodies
831 diluted in PBS-BSA 4% followed by three washes. Then, kinetoplasts and nuclei
832 were labelled with DAPI (10 µg/mL) for 5 min. Slides were washed 3 times with
833 PBS and mounted with SlowFade Gold (Molecular probes). Images were acquired
834 with MetaMorph software on Zeiss Imager Z1 or an Axioplan 2 microscope and
835 processed with ImageJ.

836 **Mitochondria staining in live cells**

837 Rhodamine-123 (30 µg/mL) was added on cell culture ($5x10^6$ - $1x10^7$ cells per mL)
838 for 15 min at room temperature, then cells were washed twice with PBS and spread
839 on slides. As an alternative to labeling mitochondria in living cells with Rhodamine-
840 123, Mitotracker (MitoTracker Green FM) was used. Cells were washed once with
841 PBS, incubated for 10 minutes with 10 µM MitoTracker Green FM, washed again
842 with PBS, and then spread onto slides. Images were acquired with MetaMorph
843 software on an Axioplan 2 microscope and processed with ImageJ.

844 **Ultrastructure Expansion Microscopy (UExM)**

845 The protocol of UExM was realized exactly as described by Casas et *al.* 2022
846 (dx.doi.org/10.17504/protocols.io.bvwqn7dw). An expansion factor was
847 determined using the ratio between the size of the coverslip (12 mm) and the size
848 of the gels after the first expansion. Images were acquired on a confocal Leica
849 SP5-MP (Bordeaux Imaging Center) using a 63X oil objective and processed with
850 ImageJ.

851 **Quantification of Mitochondrial junctions - ImageJ macro**

852 To quantify the number of mitochondrial junctions, an ImageJ macro was
853 developed with the help of the Bordeaux Imaging Center (BIC). The script is
854 presented in supplemental (**Data S1**).

855 **Endogenous tagging and overexpression of *Tb*MfnL**

856 For endogenous gene tagging, primers were designed as described in [75] and
857 PCR was performed using pPOTv7 vector as template. The pPOT used here was
858 pPOTv7 for C-terminus 10xHA tagging (blasticidin resistance). For overexpression,
859 *MfnL* gene (Tb427.7.2410) was inserted in both pLew100 (phleomycine resistance)
860 [76] and pHD1336 (blasticidin resistance) [77] expression vectors. Fragments
861 were amplified and cloned into *Hin*dIII and *Xba*I restrictions sites of the pLew100
862 and into *Hin*dIII and *Bam*HI restrictions sites of the pHD1336 expression vectors.
863 In addition, a 3xTy1 tag was added at the C-terminus of the protein in the
864 pLew100-*Tb*MfnL, using the *Xba*I and *Bam*HI restrictions sites. The truncated
865 version of *Tb*MfnL without the first 41 amino acids (*Tb*MfnL-DMTS) and without the
866 two trans-membranes domain (*Tb*MfnL-DTM) were amplified and cloned in the
867 pLew100 with a 3xTy1 tag as previously described. Catalytic lysine (K141) was
868 replaced by an alanine, using PCR approach [78] and PCR product cloned in the
869 pLew100 with a 3xTy1 tag (*Tb*MfnL-K141A). EATRO1125.T7T PCF was transfected
870 using Amaxa Nucleofector®II, program X-001 and selected in SDM79 containing
871 25 µg/ml hygromycin 10 µg/mL neomycin and 5 µg/mL phleomycin. 427 90-13
872 BSF was transfected using the same conditions and selected in IMDM containing 5
873 µg/ml hygromycin, 2.5 µg/mL neomycin and 5 µg/mL blasticidin. Primers used for
874 the constructions are presented in supplemental **Table S2**.

875 **Down-regulation of *Tb*MfnL gene expression**

876 Down-regulation of *Tb*MfnL expression by RNAi in PCF was achieved by expression
877 of stemloop "sense/antisense" RNA molecules targeting a 400-bp fragment of the
878 *Tb*MfnL gene introduced into the pLew100 tetracycline-inducible expression vector.
879 A PCR-amplified 450-bp fragment, containing the antisense *Tb*MfnL sequence was
880 inserted between *Xho*I and *Bam*HI restriction sites of the pLew100 plasmid. Then,
881 the separate 400-bp PCR-amplified fragment containing the sense *Tb*MfnL
882 sequence was inserted upstream of the antisense sequence, using *Hin*dIII and
883 *Xho*I restriction sites. The resulting plasmid, pLew100-*Tb*MfnL-SAS, contains a
884 sense and antisense version of the *Tb*MfnL fragment separated by a 50-bp
885 fragment. The EATRO1125 PCF was transfected with the pLew100-*Tb*MfnL-SAS
886 and cells were selected in SDM79 medium containing 25 µg/ml hygromycin, 10
887 µg/mL neomycin and 5 µg/mL phleomycin. Expression of the RNAi was induced by
888 tetracycline (1 µg/mL). Down-regulation of *Tb*MfnL expression by RNAi in BSF was
889 achieved exactly as described [30] with a 280-bp fragment derived from the
890 *Tb*MfnL open reading frame inserted into the p2T7-177 plasmid [79]. Linearized

891 plasmid was transfected in *T. brucei* 427 90-13 (TetR-HYG-T7RNAPOL-NEO) BSF
892 cells. Expression of the RNAi was induced by tetracycline (10 µg/mL). Primers used
893 for the constructions are presented in supplemental **Table S2**.

894 **Serial Block-Face Scanning Electron Microscopy (SBF-SEM)**

895 The entire procedure is detailed and has been carried out as described in the
896 article: Advancing yeast cell analysis: A cryomethod for serial block-face scanning
897 electron microscopy imaging in mitochondrial morphology studies [80].

898 **Immunoelectron microscopy**

899 Harvested cells were placed on the surface of formvar-coated copper grids (400
900 mesh). Each loop was quickly submersed in liquid propane (−180°C) and
901 transferred into a precooled solution of 0.1% uranyl acetate in dry acetone for 3
902 days at -82°C. Samples were rinsed with acetone at -20°C, and embedded
903 progressively at -20°C in LR Gold resin (EMS, USA). Resin polymerization was
904 carried out at -20°C for 7 days under UV illumination. Ultrathin LR Gold sections
905 were collected on nickel grids coated with formvar. Sections were first incubated
906 for 15 min with 500mM NH_4Cl in Tris-buffered saline (TBS) pH7.8, blocked 2x10
907 min with 2% BSA in TBS pH 7.8. The grids were incubated 1 hour at room
908 temperature with anti Ty1 antibody diluted to 1:200 in TBS containing 2% BSA
909 rinsed with TBS containing 2% BSA and with TBS containing 1% BSA. The samples
910 were then incubated for 1 hour at room temperature with anti-mouse IgG diluted
911 to 1:20 conjugated to 10 nm gold particles (BioCell). The sections were rinsed with
912 TBS containing 1% BSA, and fix with 1% glutaraldehyde in TBS. After rinsing with
913 TBS, grids were contrasted through a 5 min incubation with 2% uranyl acetate in
914 water, followed by 1 min incubation with 1% lead citrate. Observations were
915 performed on a HITACHI H7650 transmission electron microscope operated at 80
916 KV with an Orius 1000-11 MPx camera (Gatan, Abingdon, UK).

917 **Transmission electron microscopy (TEM)**

918 The entire procedure is thoroughly detailed and has been carried out precisely as
919 described in the article: Plunge Freezing: A Tool for the Ultrastructural and
920 Immunolocalization Studies of Suspension Cells in Transmission Electron
921 Microscopy [81].

922 **Western blot analyses**

923 Total protein extracts ($5x10^6$ cells) were separated by SDS-PAGE (10%) and
924 immunoblotted on TransBlot Turbo Midi-size PVDF Membranes (Bio-Rad).
925 Immunodetection was performed using the primary antibodies, diluted in PBS-

926 Tween Milk (0.05% Tween20, 5% skimmed milk powder), summarized in
927 supplemental **Table S3**. Revelation was performed using a second antibody
928 coupled to the horseradish peroxidase and the Clarity western enhanced-
929 chemiluminescence (ECL) substrate as describes by the manufacturer (Bio-Rad).
930 Images were acquired and analyzed with the ImageQuant Las 4000 luminescent
931 image analyzer.

932 **Mitochondria-enriched preparation, proteinase K protection assays and**
933 **carbonate extraction**

934 This procedure has been well established and allows the determination of the
935 submitochondrial localization of trypanosome proteins [44, 45, 82]. 10^8 cells were
936 lysed in SoTE buffer (20 mM Tris-HCl, pH 7.5, 0.6 mL sorbitol, and 2 mM
937 ethylenediaminetetraacetic acid), supplemented with 0.02% (w/v) digitonin
938 (D141-100MG, Sigma-Aldrich) for 5 min at 4°C. A portion of the resulting
939 suspension was collected as the total fraction (TF), while the remaining suspension
940 underwent centrifugation at 6,000 x g for 3 minutes at 4°C to isolate a
941 mitochondria-enriched pellet. This pellet was then resuspended in SoTE
942 supplemented with 0.2% (w/v) digitonin and incubated on ice for 15 minutes. The
943 resuspended mixture was divided into three tubes and subjected to centrifugation
944 at 6,000 × g for 3 minutes at 4°C, resulting in the separation of mitoplasts and
945 soluble protein in the supernatant (S). Each mitoplast pellet was resuspended in
946 SoTE and subjected to the proteinase K protection assay. Proteinase K (50 µg)
947 was added to two tubes, one supplemented with 1% Triton-X100 (v/v), while the
948 third tube remained untreated as a control. All tubes were then incubated on ice
949 for 30 minutes, followed by addition of 5 mM phenylmethylsulfonyl fluoride to stop
950 the reaction. Proteins from all fractions were precipitated with trichloroacetic acid
951 before undergoing resolution by SDS-PAGE.

952 For the extraction of integral membrane proteins using the carbonate method, the
953 procedure begins with a mitochondria-enriched pellet. The pellet is resuspended
954 in 500 µL of 10 mM $MgCl_2$ and subjected to a freeze-thaw cycle repeated ten times,
955 involving freezing in liquid nitrogen and thawing at room temperature.
956 Subsequently, the suspension is divided into two fractions: 50 µL and 450 µL. The
957 450 µL fraction is centrifuged at 10,000 × g for 5 minutes at 4 °C, with the
958 supernatant designated as the matrix fraction. The 50 µL fraction is centrifuged
959 under the same conditions, and the resulting pellet is resuspended in 50 µL of 10
960 mM $MgCl_2$, representing the membrane fraction. The remaining pellet from the 450

961 μL sample is further processed by resuspending it in 400 μL of 0.1 M Na_2CO_3 (pH
962 11). This mixture is incubated on ice for 30 minutes, sonicated four times, and
963 centrifuged at 20,000 × g for 20 minutes at 4 °C. The supernatant is collected as
964 the peripheral membrane protein fraction. The pellet is washed by resuspension in
965 400 μL of 0.1 M Na_2CO_3 and subjected to another centrifugation under the same
966 conditions. This final pellet constitutes the integral membrane protein fraction. All
967 protein fractions are precipitated using trichloroacetic acid, resuspended in 50 to
968 100 μL of 2% SDS, and analyzed by SDS–PAGE.

969 **Sequence database searches and phylogenetic analysis**

970 Two databases were used to identify sequences homologous to the *T. brucei*
971 *Tb*MfnL sequence (Tb927.7.2410). The first search was conducted using Blastp
972 [83] (protein-protein BLAST, https://blast.ncbi.nlm.nih.gov/Blast.cgi) on the NCBI
973 nr protein database, with *Tb*MfnL as the query and kinetoplastids excluded from
974 the search. The parameters included a maximum of 5000 target sequences and
975 the Blosum62 matrix. For the EuKProt v3 database [84] search
976 (https://evocellbio.com/eukprot/), the Blastp server was used with the entire
977 database (993 species) and *Tb*MfnL as the query, without applying advanced
978 parameters. The selection of sequences was then performed manually, retaining
979 only those sequences that exhibited homology across the entire *Tb*MfnL protein.
980 Sequences corresponding solely to the highly conserved GTPase domain were
981 excluded. A total of 315 sequences were selected for phylogenetic analysis. An
982 additional 23 sequences were included from well-characterized dynamins involved
983 in fission (Dnm1), fusion (Opa1, Mfn1/2, Fzo1), BDLP (the cyanobacterial Mfn
984 homolog), and dynamins associated with clathrin-mediated endocytosis (Dyn1/2)
985 to be used as an outgroup.

986 The sequences were aligned with MAFFT L-INS-i v7.450 [85] and trimmed with
987 BMGE v1.12 (-m BLOSUM30 -b 3 -g 0.2 -h 0.5) [86]. A maximum likelihood
988 phylogenetic tree was then reconstructed with IQ-TREE v.2.0.3 [87] using its
989 model finder (-m TEST) option, including complex mixture models, to select the
990 best fit substitution model, as well as 1000 ultrafast bootstrap replicates to
991 estimate branch statistical support.

992 **Structural prediction software and sequence analysis**

993 Structure predictions were performed using PSIPRED
994 ("http://bioinf.cs.ucl.ac.uk/psipred/") [72] and prediction of mitochondrial

995 targeting sequences by various algorithms (MitoFates, PSORT II and TargetP-2.0)
996 [88].

997 **Statistical analysis**

998 Experiments were performed at least in triplicates. Statistical analyses were
999 performed using Prism (GraphPad) software. The results are presented as mean ±
1000 S.D. Where indicated the results were subjected to two-sided Student's t-test to
1001 determine statistical differences against the indicated group (Confidence interval
1002 95% - P-value style: 0.1234 (ns); 0.0332 (*); 0.0021 (**); 0.0002 (***);
1003 <0.0001 (****)).

1004 **SUPPLEMENTAL INFORMATION**

1005 **Figure S1**: Alignment of various kinetoplastid MfnL proteins.

1006 **Figure S2**: Alignment between *Tb*MfnL and various eukaryotic and prokaryotic MfnLs.

1007 **Figure S3**: Complete maximum likelihood phylogenetic tree of eukaryotic and prokaryotic DSPs.

1008 **Figure S4**: Growth curves of parental, over-expressing, and mutant cells.

1009 **Figure S5**: Inactivation of *Tb*MfnL expression using the CRISPR/Cas9 system.

1010 **Figure S6**: TEM analysis of cells cultured on glucose or proline.

1011 **Figure S7**: Down-regulation of *Tb*MfnL expression by RNAi.

1012 **Figure S8**: Results of the ImageJ plugin applied to rhodamine-stained cells.

1013 **Figure S9**: Overexpression levels of different *Tb*MfnL variants.

1014 **Figure S10**: Variation in *Tb*MfnL expression levels upon tetracycline induction.

1015 **Figure S11**: Mitochondrial localization of *Tb*MfnL as shown by immunoelectron microscopy.

1016 **Figure S12**: Full gel results shown for the PK and carbonate assays.

1017 **Figure S13**: pLDDT score for *Tb*MfnL protein derived from AlphaFold predictions.

1018 **Data S1**: ImageJ code used in the study.

1019 **Table S1**: BLASTp analysis results for several identified organisms.

1020 **Table S2**: List of all primers and guide RNAs utilized in this study.

1021 **Table S3**: List of all antibodies used in this study.

1022

1023 **REFERENCES**

1024 1. Bohringer, S., and Hecker, H. (1975). Quantitative ultrastructural
1025 investigations of the life cycle of Trypanosoma brucei: a morphometric
1026 analysis. J Protozool *22*, 463-467.
1027 2. Bily, T., Sheikh, S., Mallet, A., Bastin, P., Perez-Morga, D., Lukes, J., and
1028 Hashimi, H. (2021). Ultrastructural Changes of the Mitochondrion During
1029 the Life Cycle of Trypanosoma brucei. The Journal of eukaryotic
1030 microbiology, e12846.
1031 3. Priest, J.W., and Hajduk, S.L. (1994). Developmental regulation of
1032 Trypanosoma brucei cytochrome c reductase during bloodstream to
1033 procyclic differentiation. Mol Biochem Parasitol *65*, 291-304.
1034 4. van Hellemond, J.J., Opperdoes, F.R., and Tielens, A.G. (2005). The
1035 extraordinary mitochondrion and unusual citric acid cycle in Trypanosoma
1036 brucei. Biochem Soc Trans *33*, 967-971.
1037 5. Michels, P.A., Bringaud, F., Herman, M., and Hannaert, V. (2006). Metabolic
1038 functions of glycosomes in trypanosomatids. Biochim Biophys Acta *1763*,
1039 1463-1477.
1040 6. Bringaud, F., Riviere, L., and Coustou, V. (2006). Energy metabolism of
1041 trypanosomatids: adaptation to available carbon sources. Mol Biochem
1042 Parasitol *149*, 1-9.
1043 7. Duvezin-Caubet, S., Jagasia, R., Wagener, J., Hofmann, S., Trifunovic, A.,
1044 Hansson, A., Chomyn, A., Bauer, M.F., Attardi, G., Larsson, N.G., et al.
1045 (2006). Proteolytic processing of OPA1 links mitochondrial dysfunction to
1046 alterations in mitochondrial morphology. J Biol Chem *281*, 37972-37979.
1047 8. Sauvanet, C., Duvezin-Caubet, S., di Rago, J.P., and Rojo, M. (2010).
1048 Energetic requirements and bioenergetic modulation of mitochondrial
1049 morphology and dynamics. Semin Cell Dev Biol *21*, 558-565.
1050 9. Silva Ramos, E., Larsson, N.G., and Mourier, A. (2016). Bioenergetic roles
1051 of mitochondrial fusion. Biochim Biophys Acta *1857*, 1277-1283.
1052 10. Chan, D.C. (2012). Fusion and fission: interlinked processes critical for
1053 mitochondrial health. Annual review of genetics *46*, 265-287.
1054 11. Westermann, B. (2010). Mitochondrial fusion and fission in cell life and
1055 death. Nat Rev Mol Cell Biol *11*, 872-884.

1056 12. Sesaki, H., Adachi, Y., Kageyama, Y., Itoh, K., and Iijima, M. (2014). In vivo
1057 functions of Drp1: lessons learned from yeast genetics and mouse
1058 knockouts. Biochim Biophys Acta *1842*, 1179-1185.
1059 13. Otera, H., Ishihara, N., and Mihara, K. (2013). New insights into the function
1060 and regulation of mitochondrial fission. Biochim Biophys Acta *1833*, 1256-
1061 1268.
1062 14. Malka, F., Guillery, O., Cifuentes-Diaz, C., Guillou, E., Belenguer, P.,
1063 Lombes, A., and Rojo, M. (2005). Separate fusion of outer and inner
1064 mitochondrial membranes. EMBO Rep *6*, 853-859.
1065 15. Song, Z., Ghochani, M., McCaffery, J.M., Frey, T.G., and Chan, D.C. (2009).
1066 Mitofusins and OPA1 mediate sequential steps in mitochondrial membrane
1067 fusion. Mol Biol Cell *20*, 3525-3532.
1068 16. Legros, F., Lombes, A., Frachon, P., and Rojo, M. (2002). Mitochondrial
1069 fusion in human cells is efficient, requires the inner membrane potential,
1070 and is mediated by mitofusins. Mol Biol Cell *13*, 4343-4354.
1071 17. Bertholet, A.M., Delerue, T., Millet, A.M., Moulis, M.F., David, C., Daloyau,
1072 M., Arnaune-Pelloquin, L., Davezac, N., Mils, V., Miquel, M.C., et al. (2016).
1073 Mitochondrial fusion/fission dynamics in neurodegeneration and neuronal
1074 plasticity. Neurobiol Dis *90*, 3-19.
1075 18. Hughes, L., Borrett, S., Towers, K., Starborg, T., and Vaughan, S. (2017).
1076 Patterns of organelle ontogeny through a cell cycle revealed by whole-cell
1077 reconstructions using 3D electron microscopy. J Cell Sci *130*, 637-647.
1078 19. Chanez, A.L., Hehl, A.B., Engstler, M., and Schneider, A. (2006). Ablation
1079 of the single dynamin of T. brucei blocks mitochondrial fission and
1080 endocytosis and leads to a precise cytokinesis arrest. J Cell Sci *119*, 2968-
1081 2974.
1082 20. Jakob, M., Hoffmann, A., Amodeo, S., Peitsch, C., Zuber, B., and
1083 Ochsenreiter, T. (2016). Mitochondrial growth during the cell cycle of
1084 Trypanosoma brucei bloodstream forms. Sci Rep *6*, 36565.
1085 21. Esseiva, A.C., Chanez, A.L., Bochud-Allemann, N., Martinou, J.C., Hemphill,
1086 A., and Schneider, A. (2004). Temporal dissection of Bax-induced events
1087 leading to fission of the single mitochondrion in Trypanosoma brucei. EMBO
1088 Rep *5*, 268-273.

1089 22. Gibson, W., Crow, M., and Kearns, J. (1997). Kinetoplast DNA minicircles
1090 are inherited from both parents in genetic crosses of Trypanosoma brucei.
1091 Parasitol Res *83*, 483-488.
1092 23. DiMaio, J., Ruthel, G., Cannon, J.J., Malfara, M.F., and Povelones, M.L.
1093 (2018). The single mitochondrion of the kinetoplastid parasite Crithidia
1094 fasciculata is a dynamic network. PLoS ONE *13*, e0202711.
1095 24. van der Bliek, A.M., Shen, Q., and Kawajiri, S. (2013). Mechanisms of
1096 mitochondrial fission and fusion. Cold Spring Harb Perspect Biol *5*.
1097 25. Logan, D.C. (2006). Plant mitochondrial dynamics. Biochim Biophys Acta
1098 *1763*, 430-441.
1099 26. Arimura, S.I. (2018). Fission and Fusion of Plant Mitochondria, and Genome
1100 Maintenance. Plant Physiol *176*, 152-161.
1101 27. Gao, H., Sage, T.L., and Osteryoung, K.W. (2006). FZL, an FZO-like protein
1102 in plants, is a determinant of thylakoid and chloroplast morphology. Proc
1103 Natl Acad Sci U S A *103*, 6759-6764.
1104 28. Morgan, G.W., Goulding, D., and Field, M.C. (2004). The single dynamin-
1105 like protein of Trypanosoma brucei regulates mitochondrial division and is
1106 not required for endocytosis. J Biol Chem *279*, 10692-10701.
1107 29. Benz, C., Stribrna, E., Hashimi, H., and Lukes, J. (2017). Dynamin-like
1108 proteins in Trypanosoma brucei: A division of labour between two paralogs?
1109 PLoS ONE *12*, e0177200.
1110 30. Vanwalleghem, G., Fontaine, F., Lecordier, L., Tebabi, P., Klewe, K., Nolan,
1111 D.P., Yamaryo-Botte, Y., Botte, C., Kremer, A., Burkard, G.S., et al. (2015).
1112 Coupling of lysosomal and mitochondrial membrane permeabilization in
1113 trypanolysis by APOL1. Nature communications *6*, 8078.
1114 31. Urbaniak, M.D., Guther, M.L., and Ferguson, M.A. (2012). Comparative
1115 SILAC proteomic analysis of Trypanosoma brucei bloodstream and procyclic
1116 lifecycle stages. PLoS ONE *7*, e36619.
1117 32. Siegel, T.N., Hekstra, D.R., Wang, X., Dewell, S., and Cross, G.A. (2010).
1118 Genome-wide analysis of mRNA abundance in two life-cycle stages of
1119 Trypanosoma brucei and identification of splicing and polyadenylation sites.
1120 Nucleic Acids Res *38*, 4946-4957.
1121 33. Millerioux, Y., Ebikeme, C., Biran, M., Morand, P., Bouyssou, G., Vincent,
1122 I.M., Mazet, M., Riviere, L., Franconi, J.M., Burchmore, R.J., et al. (2013).
1123 The threonine degradation pathway of the Trypanosoma brucei procyclic

1124 form: the main carbon source for lipid biosynthesis is under metabolic
1125 control. Mol Microbiol *90*, 114-129.
1126 34. Billington, K., Halliday, C., Madden, R., Dyer, P., Barker, A.R., Moreira-Leite,
1127 F.F., Carrington, M., Vaughan, S., Hertz-Fowler, C., Dean, S., et al. (2023).
1128 Genome-wide subcellular protein map for the flagellate parasite
1129 Trypanosoma brucei. Nat Microbiol *8*, 533-547.
1130 35. Nunnari, J., Marshall, W.F., Straight, A., Murray, A., Sedat, J.W., and
1131 Walter, P. (1997). Mitochondrial transmission during mating in
1132 Saccharomyces cerevisiae is determined by mitochondrial fusion and fission
1133 and the intramitochondrial segregation of mitochondrial DNA. Mol Biol Cell
1134 *8*, 1233-1242.
1135 36. Asencio, C., Herve, P., Morand, P., Oliveres, Q., Morel, C.A., Prouzet-
1136 Mauleon, V., Biran, M., Monic, S., Bonhivers, M., Robinson, D.R., et al.
1137 (2024). Streptococcus pyogenes Cas9 ribonucleoprotein delivery for
1138 efficient, rapid and marker-free gene editing in Trypanosoma and
1139 Leishmania. Mol Microbiol.
1140 37. Hales, K.G., and Fuller, M.T. (1997). Developmentally regulated
1141 mitochondrial fusion mediated by a conserved, novel, predicted GTPase. Cell
1142 *90*, 121-129.
1143 38. Hermann, G.J., Thatcher, J.W., Mills, J.P., Hales, K.G., Fuller, M.T., Nunnari,
1144 J., and Shaw, J.M. (1998). Mitochondrial fusion in yeast requires the
1145 transmembrane GTPase Fzo1p. J Cell Biol *143*, 359-373.
1146 39. Santel, A., Frank, S., Gaume, B., Herrler, M., Youle, R.J., and Fuller, M.T.
1147 (2003). Mitofusin-1 protein is a generally expressed mediator of
1148 mitochondrial fusion in mammalian cells. J Cell Sci *116*, 2763-2774.
1149 40. Gambarotto, D., Hamel, V., and Guichard, P. (2021). Ultrastructure
1150 expansion microscopy (U-ExM). Methods in cell biology *161*, 57-81.
1151 41. Amodeo, S., Kalichava, A., Fradera-Sola, A., Bertiaux-Lequoy, E., Guichard,
1152 P., Butter, F., and Ochsenreiter, T. (2021). Characterization of the novel
1153 mitochondrial genome segregation factor TAP110 in Trypanosoma brucei. J
1154 Cell Sci *134*.
1155 42. Gorilak, P., Pruzincova, M., Vachova, H., Olsinova, M., Schmidt
1156 Cernohorska, M., and Varga, V. (2021). Expansion microscopy facilitates
1157 quantitative super-resolution studies of cytoskeletal structures in
1158 kinetoplastid parasites. Open Biol *11*, 210131.

1159 43. Rojo, M., Legros, F., Chateau, D., and Lombes, A. (2002). Membrane
1160 topology and mitochondrial targeting of mitofusins, ubiquitous mammalian
1161 homologs of the transmembrane GTPase Fzo. J Cell Sci *115*, 1663-1674.
1162 44. Kaurov, I., Vancova, M., Schimanski, B., Cadena, L.R., Heller, J., Bily, T.,
1163 Potesil, D., Eichenberger, C., Bruce, H., Oeljeklaus, S., et al. (2018). The
1164 Diverged Trypanosome MICOS Complex as a Hub for Mitochondrial Cristae
1165 Shaping and Protein Import. Curr Biol *28*, 3393-3407 e3395.
1166 45. Wenger, C., Oeljeklaus, S., Warscheid, B., Schneider, A., and Harsman, A.
1167 (2017). A trypanosomal orthologue of an intermembrane space chaperone
1168 has a non-canonical function in biogenesis of the single mitochondrial inner
1169 membrane protein translocase. PLoS Pathog *13*, e1006550.
1170 46. Pyrih, J., Hammond, M., Alves, A., Dean, S., Sunter, J.D., Wheeler, R.J.,
1171 Gull, K., and Lukes, J. (2023). Comprehensive sub-mitochondrial protein
1172 map of the parasitic protist Trypanosoma brucei defines critical features of
1173 organellar biology. Cell reports *42*, 113083.
1174 47. Daumke, O., and Praefcke, G.J. (2016). Invited review: Mechanisms of GTP
1175 hydrolysis and conformational transitions in the dynamin superfamily.
1176 Biopolymers *105*, 580-593.
1177 48. Ramachandran, R., and Schmid, S.L. (2018). The dynamin superfamily.
1178 Curr Biol *28*, R411-R416.
1179 49. Shepard, K.A., and Yaffe, M.P. (1999). The yeast dynamin-like protein,
1180 Mgm1p, functions on the mitochondrial outer membrane to mediate
1181 mitochondrial inheritance. J Cell Biol *144*, 711-720.
1182 50. Derelle, R., Torruella, G., Klimes, V., Brinkmann, H., Kim, E., Vlcek, C.,
1183 Lang, B.F., and Elias, M. (2015). Bacterial proteins pinpoint a single
1184 eukaryotic root. Proc Natl Acad Sci U S A *112*, E693-699.
1185 51. Sawant, P., Eissenberger, K., Karier, L., Mascher, T., and Bramkamp, M.
1186 (2016). A dynamin-like protein involved in bacterial cell membrane
1187 surveillance under environmental stress. Environ Microbiol *18*, 2705-2720.
1188 52. de Sousa Borges, A., and Scheffers, D.J. (2016). Bacterial dynamin as a
1189 membrane puncture repair kit. Environ Microbiol *18*, 2298-2301.
1190 53. Michie, K.A., Boysen, A., Low, H.H., Moller-Jensen, J., and Lowe, J. (2014).
1191 LeoA, B and C from enterotoxigenic Escherichia coli (ETEC) are bacterial
1192 dynamins. PLoS ONE *9*, e107211.

1193 54. Schlimpert, S., Wasserstrom, S., Chandra, G., Bibb, M.J., Findlay, K.C.,
1194 Flardh, K., and Buttner, M.J. (2017). Two dynamin-like proteins stabilize
1195 FtsZ rings during Streptomyces sporulation. Proc Natl Acad Sci U S A *114*,
1196 E6176-E6183.
1197 55. Bramkamp, M. (2012). Structure and function of bacterial dynamin-like
1198 proteins. Biol Chem *393*, 1203-1214.
1199 56. Burmann, F., Ebert, N., van Baarle, S., and Bramkamp, M. (2011). A
1200 bacterial dynamin-like protein mediating nucleotide-independent membrane
1201 fusion. Mol Microbiol *79*, 1294-1304.
1202 57. Jimah, J.R., and Hinshaw, J.E. (2019). Structural Insights into the
1203 Mechanism of Dynamin Superfamily Proteins. Trends Cell Biol *29*, 257-273.
1204 58. Liu, J., Noel, J.K., and Low, H.H. (2018). Structural basis for membrane
1205 tethering by a bacterial dynamin-like pair. Nature communications *9*, 3345.
1206 59. Lindsay, M.R., Webb, R.I., and Fuerst, J.A. (1997). Pirellulosomes: a new
1207 type of membrane-bounded cell compartment in planctomycete bacteria of
1208 the genus Pirellula. Microbiology (Reading) *143*, 739-748.
1209 60. Fuerst, J.A., and Webb, R.I. (1991). Membrane-bounded nucleoid in the
1210 eubacterium Gemmata obscuriglobus. Proc Natl Acad Sci U S A *88*, 8184-
1211 8188.
1212 61. Jogler, C. (2014). The bacterial 'mitochondrium'. Mol Microbiol *94*, 751-755.
1213 62. Neumann, S., Wessels, H.J., Rijpstra, W.I., Sinninghe Damste, J.S., Kartal,
1214 B., Jetten, M.S., and van Niftrik, L. (2014). Isolation and characterization of
1215 a prokaryotic cell organelle from the anammox bacterium Kuenenia
1216 stuttgartiensis. Mol Microbiol *94*, 794-802.
1217 63. Herzog, S., Schumann, M.R., and Fleissner, A. (2015). Cell fusion in
1218 Neurospora crassa. Current opinion in microbiology *28*, 53-59.
1219 64. Sesaki, H., and Jensen, R.E. (1999). Division versus fusion: Dnm1p and
1220 Fzo1p antagonistically regulate mitochondrial shape. J Cell Biol *147*, 699-
1221 706.
1222 65. Niemann, M., Wiese, S., Mani, J., Chanfon, A., Jackson, C., Meisinger, C.,
1223 Warscheid, B., and Schneider, A. (2013). Mitochondrial outer membrane
1224 proteome of Trypanosoma brucei reveals novel factors required to maintain
1225 mitochondrial morphology. Mol Cell Proteomics *12*, 515-528.

1226 66. Povelones, M.L., Tiengwe, C., Gluenz, E., Gull, K., Englund, P.T., and
1227 Jensen, R.E. (2013). Mitochondrial shape and function in trypanosomes
1228 requires the outer membrane protein, TbLOK1. Mol Microbiol *87*, 713-729.
1229 67. Otera, H., Ohsakaya, S., Nagaura, Z., Ishihara, N., and Mihara, K. (2005).
1230 Export of mitochondrial AIF in response to proapoptotic stimuli depends on
1231 processing at the intermembrane space. EMBO J *24*, 1375-1386.
1232 68. Sheikh, S., Panek, T., Gahura, O., Tyc, J., Zahonova, K., Lukes, J., Elias,
1233 M., and Hashimi, H. (2023). A Novel Group of Dynamin-Related Proteins
1234 Shared by Eukaryotes and Giant Viruses Is Able to Remodel Mitochondria
1235 From Within the Matrix. Mol Biol Evol *40*.
1236 69. Kumar, A., Gok, M.O., Nguyen, K.N., Connor, O.M., Reese, M.L., Wideman,
1237 J.G., Munoz-Gomez, S.A., and Friedman, J.R. (2024). A dynamin
1238 superfamily-like pseudoenzyme coordinates with MICOS to promote cristae
1239 architecture. Curr Biol *34*, 2606-2622 e2609.
1240 70. Mears, J.A. (2024). Mitochondrial biology: Unique membrane remodeling
1241 from the matrix. Curr Biol *34*, R581-R583.
1242 71. Mattie, S., Riemer, J., Wideman, J.G., and McBride, H.M. (2018). A new
1243 mitofusin topology places the redox-regulated C terminus in the
1244 mitochondrial intermembrane space. J Cell Biol *217*, 507-515.
1245 72. Jones, D.T. (1999). Protein secondary structure prediction based on
1246 position-specific scoring matrices. J Mol Biol *292*, 195-202.
1247 73. Hannaert, V., Albert, M.A., Rigden, D.J., da Silva Giotto, M.T., Thiemann,
1248 O., Garratt, R.C., Van Roy, J., Opperdoes, F.R., and Michels, P.A. (2003).
1249 Kinetic characterization, structure modelling studies and crystallization of
1250 Trypanosoma brucei enolase. Eur J Biochem *270*, 3205-3213.
1251 74. Hirumi, H., and Hirumi, K. (1989). Continuous cultivation of Trypanosoma
1252 brucei blood stream forms in a medium containing a low concentration of
1253 serum protein without feeder cell layers. J Parasitol *75*, 985-989.
1254 75. Dean, S., Sunter, J., Wheeler, R.J., Hodkinson, I., Gluenz, E., and Gull, K.
1255 (2015). A toolkit enabling efficient, scalable and reproducible gene tagging
1256 in trypanosomatids. Open Biol *5*, 140197.
1257 76. Wirtz, E., Leal, S., Ochatt, C., and Cross, G.A. (1999). A tightly regulated
1258 inducible expression system for conditional gene knock-outs and dominant-
1259 negative genetics in Trypanosoma brucei. Mol Biochem Parasitol *99*, 89-
1260 101.

1261 77. Biebinger, S., Wirtz, L.E., Lorenz, P., and Clayton, C. (1997). Vectors for
1262 inducible expression of toxic gene products in bloodstream and procyclic
1263 Trypanosoma brucei. Mol Biochem Parasitol *85*, 99-112.
1264 78. Ling, M.M., and Robinson, B.H. (1997). Approaches to DNA mutagenesis:
1265 an overview. Anal Biochem *254*, 157-178.
1266 79. Wickstead, B., Ersfeld, K., and Gull, K. (2002). Targeting of a tetracycline-
1267 inducible expression system to the transcriptionally silent minichromosomes
1268 of Trypanosoma brucei. Mol Biochem Parasitol *125*, 211-216.
1269 80. Blancard, C., Decoeur, F., Duvezin-Caubet, S., Giraud, M.F., and Salin, B.
1270 (2024). Advancing yeast cell analysis: A cryomethod for serial block-face
1271 scanning electron microscopy imaging in mitochondrial morphology studies.
1272 Biology of the cell / under the auspices of the European Cell Biology
1273 Organization, e202400038.
1274 81. Blancard, C., and Salin, B. (2017). Plunge Freezing: A Tool for the
1275 Ultrastructural and Immunolocalization Studies of Suspension Cells in
1276 Transmission Electron Microscopy. J Vis Exp, e54874.
1277 82. Bochud-Allemann, N., and Schneider, A. (2002). Mitochondrial substrate
1278 level phosphorylation is essential for growth of procyclic Trypanosoma
1279 brucei. J Biol Chem *277*, 32849-32854.
1280 83. Altschul, S.F., Gish, W., Miller, W., Myers, E.W., and Lipman, D.J. (1990).
1281 Basic local alignment search tool. J Mol Biol *215*, 403-410.
1282 84. Richter, D.J., Berney, C., Strassert, J.F.H., Poh, Y.-P., Herman, E.K., Muñoz-
1283 Gómez, S.A., Wideman, J.G., Burki, F., and de Vargas, C. (2022). EukProt:
1284 A database of genome-scale predicted proteins across the diversity of
1285 eukaryotes. bioRxiv, 2020.2006.2030.180687.
1286 85. Katoh, K., and Standley, D.M. (2013). MAFFT multiple sequence alignment
1287 software version 7: improvements in performance and usability. Mol Biol
1288 Evol *30*, 772-780.
1289 86. Criscuolo, A., and Gribaldo, S. (2010). BMGE (Block Mapping and Gathering
1290 with Entropy): a new software for selection of phylogenetic informative
1291 regions from multiple sequence alignments. BMC Evol Biol *10*, 210.
1292 87. Minh, B.Q., Schmidt, H.A., Chernomor, O., Schrempf, D., Woodhams, M.D.,
1293 von Haeseler, A., and Lanfear, R. (2020). IQ-TREE 2: New Models and
1294 Efficient Methods for Phylogenetic Inference in the Genomic Era. Mol Biol
1295 Evol *37*, 1530-1534.

1296 88. Claros, M.G., and Vincens, P. (1996). Computational method to predict
1297 mitochondrially imported proteins and their targeting sequences. Eur J
1298 Biochem *241*, 779-786.
1299

Figure

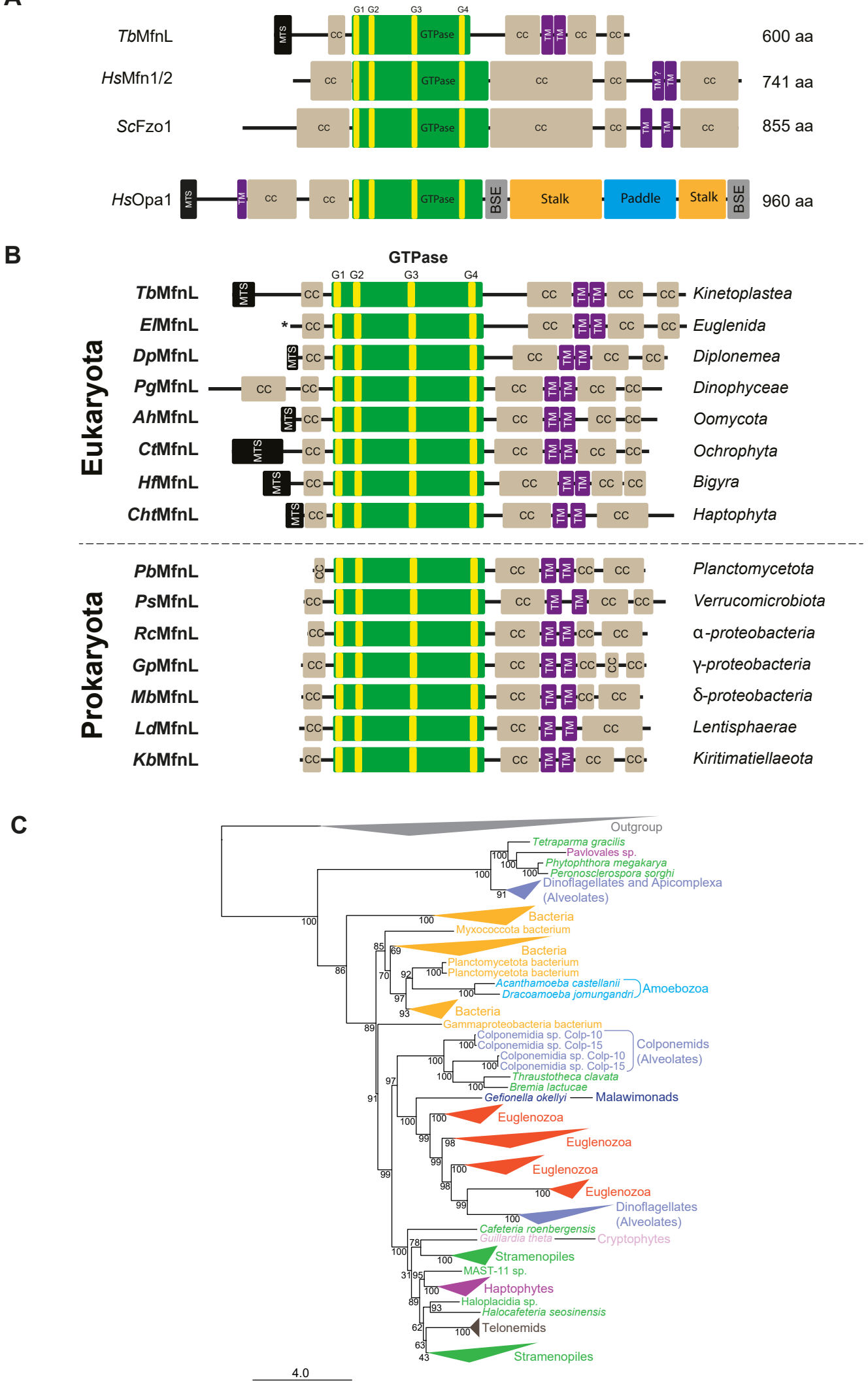

Figure 1

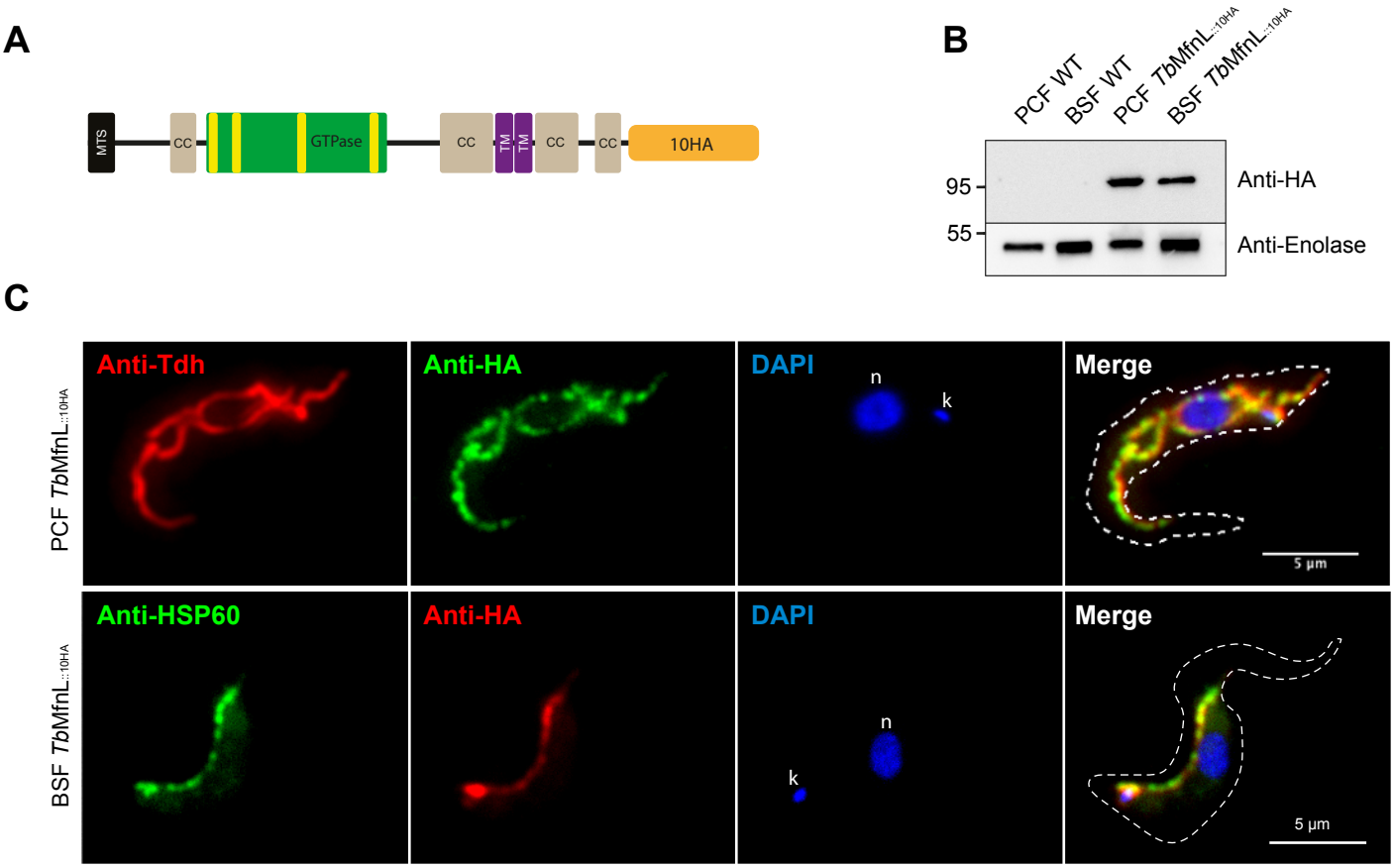
A
MTS
CC
GTPase
CC
TM
TM
CC
CC
10HA
B
PCF WT
BSF WT
PCF TbMfnL::10HA
BSF TbMfnL::10HA
95
55
Anti-HA
Anti-Enolase
C
PCF TbMfnL::10HA
Anti-Tdh
Anti-HA
DAPI
n
k
Merge
5 µm
BSF TbMfnL::10HA
Anti-HSP60
Anti-HA
DAPI
n
k
Merge
5 µm

Figure 2

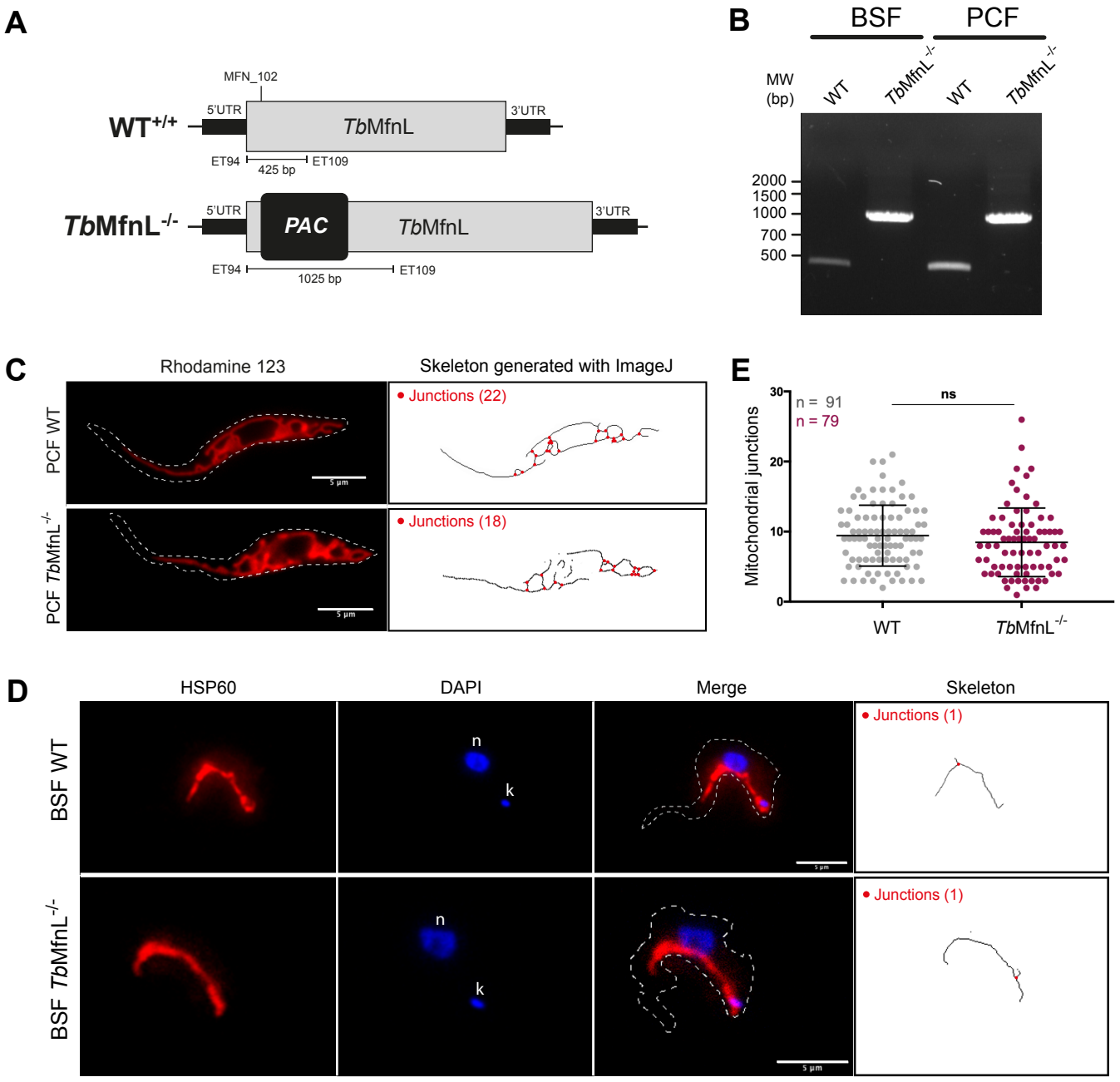
A
MFN_102
WT+/+
5'UTR
TbMfnL
3'UTR
ET94
425 bp
ET109
TbMfnL-/-
5'UTR
PAC
TbMfnL
3'UTR
ET94
1025 bp
ET109
B
BSF
PCF
MW (bp)
WT
TbMfnL-/-
WT
TbMfnL-/-
2000
1500
1000
700
500
C
Rhodamine 123
Skeleton generated with ImageJ
PCF WT
Junctions (22)
PCF TbMfnL-/-
Junctions (18)
5 µm
E
n = 91
n = 79
ns
Mitochondrial junctions
30
20
10
0
WT
TbMfnL-/-
D
HSP60
DAPI
Merge
Skeleton
BSF WT
n
k
Junctions (1)
BSF TbMfnL-/-
n
k
Junctions (1)
5 µm

Figure 3

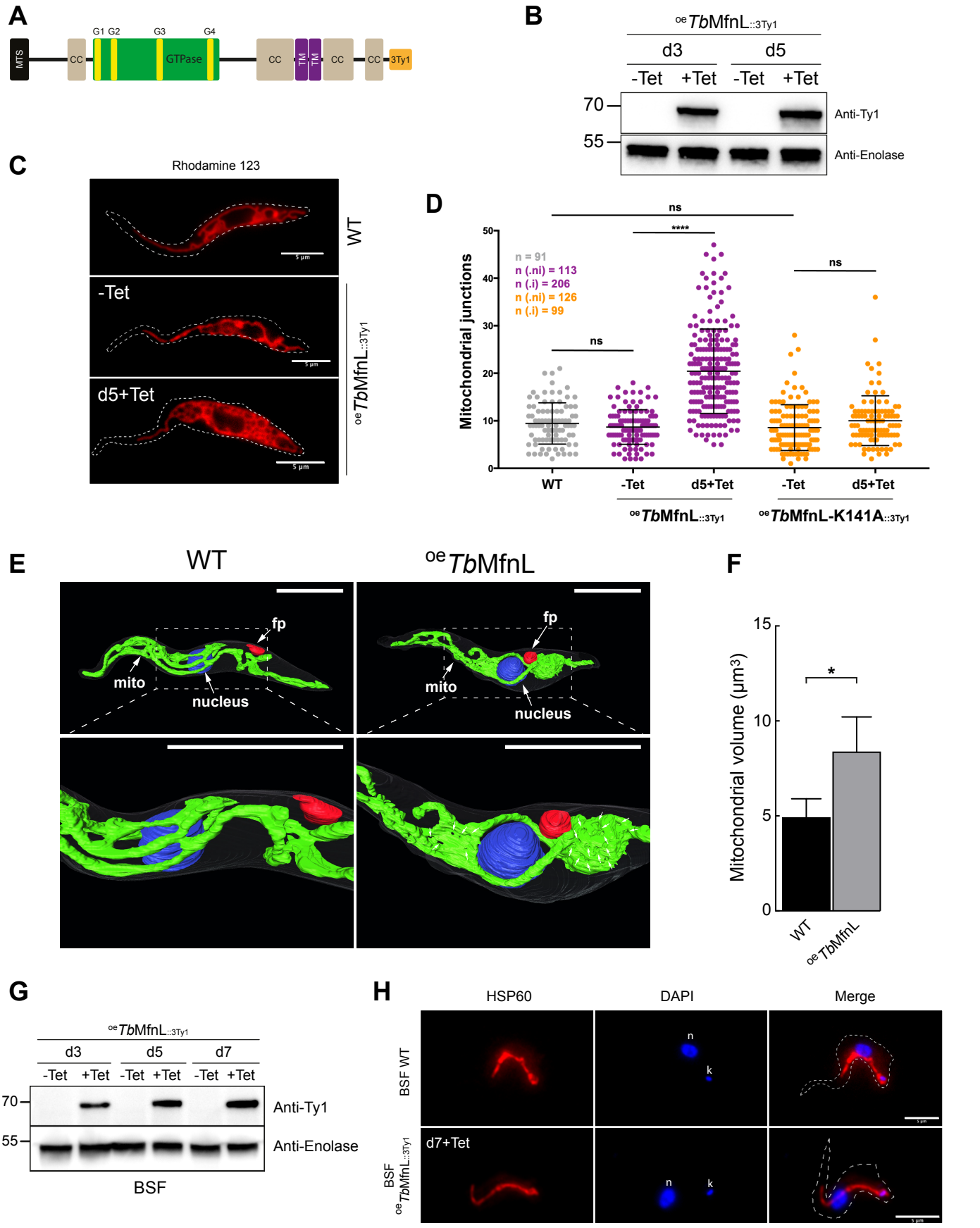
A
MTS
CC
G1 G2
G3
G4
GTPase
CC
TM
TM
CC
CC
3Ty1
B
oeTbMfnL::3Ty1
d3
d5
-Tet
+Tet
-Tet
+Tet
70
55
Anti-Ty1
Anti-Enolase
C
Rhodamine 123
WT
-Tet
d5+Tet
oeTbMfnL::3Ty1
D
Mitochondrial junctions
n = 91
n (.ni) = 113
n (.i) = 206
n (.ni) = 126
n (.i) = 99
ns
****
ns
ns
WT
-Tet
d5+Tet
-Tet
d5+Tet
oeTbMfnL::3Ty1
oeTbMfnL-K141A::3Ty1
E
WT
oeTbMfnL
fp
mito
nucleus
fp
mito
nucleus
F
Mitochondrial volume (µm³)
*
WT
oeTbMfnL
G
oeTbMfnL::3Ty1
d3
d5
d7
-Tet
+Tet
-Tet
+Tet
-Tet
+Tet
70
55
Anti-Ty1
Anti-Enolase
BSF
H
HSP60
DAPI
Merge
BSF WT
n
k
d7+Tet
BSF oeTbMfnL::3Ty1
n
k

Figure 4

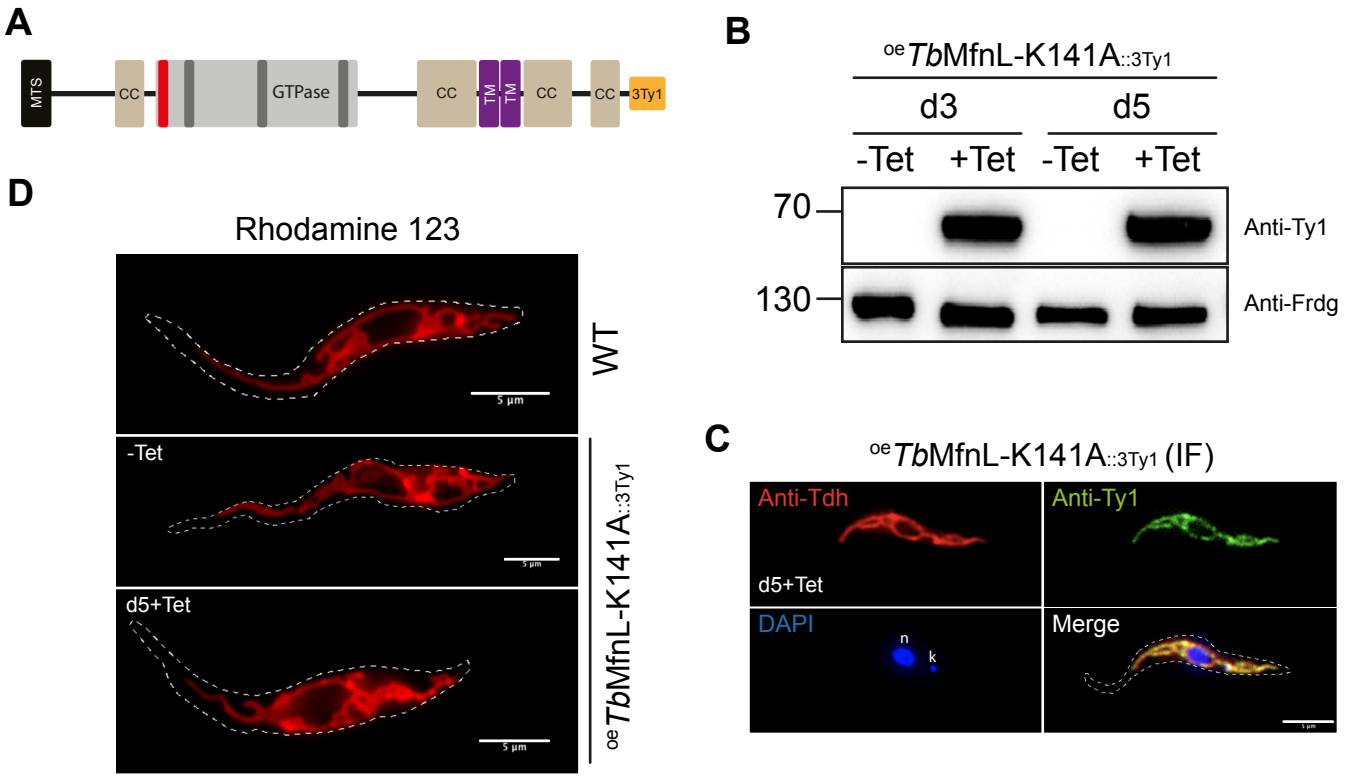
A
MTS
CC
GTPase
CC
TM
TM
CC
CC
3Ty1
B
oeTbMfnL-K141A::3Ty1
d3
d5
-Tet
+Tet
-Tet
+Tet
70
130
Anti-Ty1
Anti-Frdg
C
oeTbMfnL-K141A::3Ty1 (IF)
Anti-Tdh
Anti-Ty1
d5+Tet
DAPI
n
k
Merge
D
Rhodamine 123
WT
-Tet
d5+Tet
5 µm
oeTbMfnL-K141A::3Ty1

Figure 5

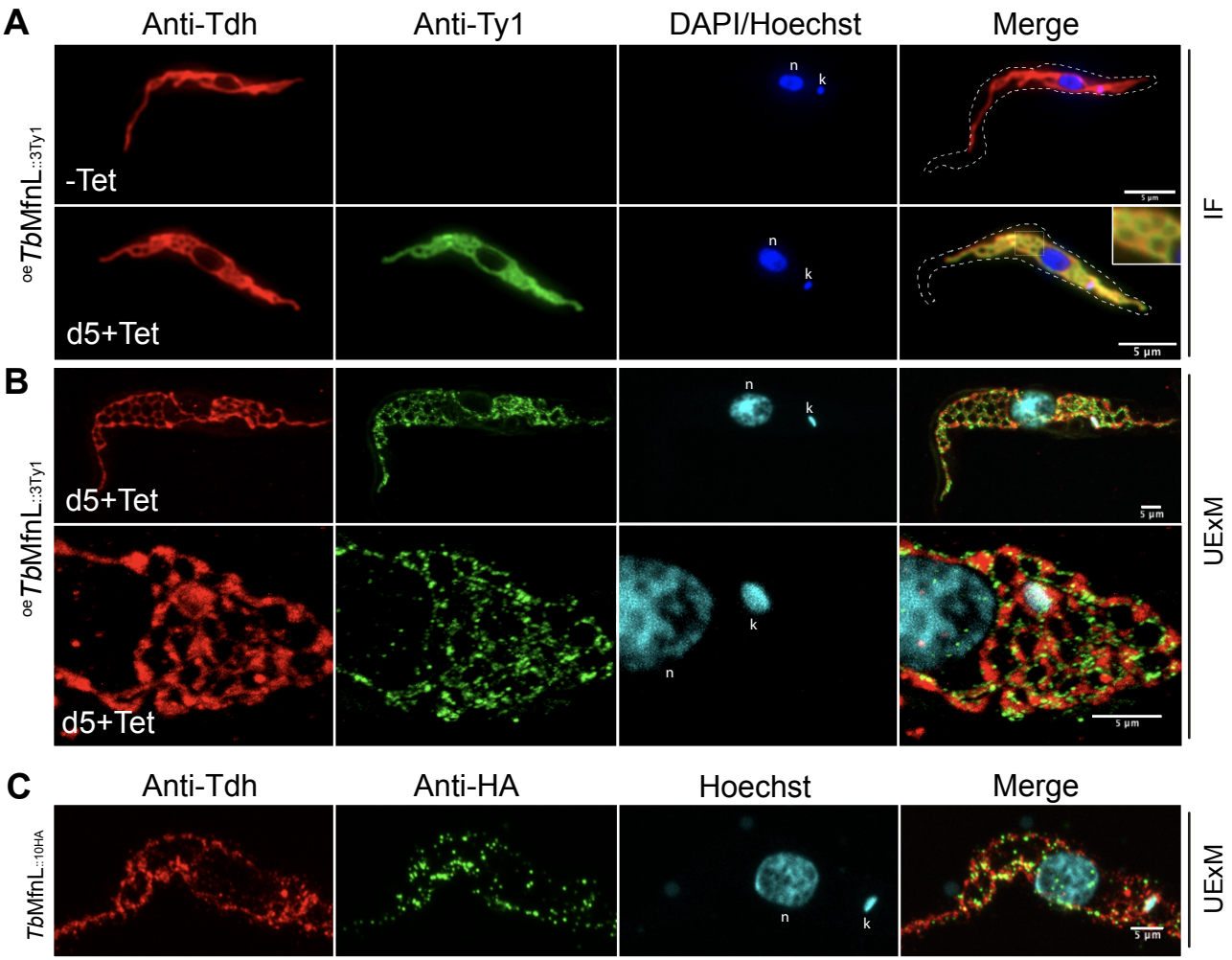
A
Anti-Tdh
Anti-Ty1
DAPI/Hoechst
Merge
oeTbMfnL::3Ty1
-Tet
d5+Tet
n
k
5 µm
IF
B
d5+Tet
UExM
C
Anti-Tdh
Anti-HA
Hoechst
Merge
TbMfnL::10HA

Figure 6

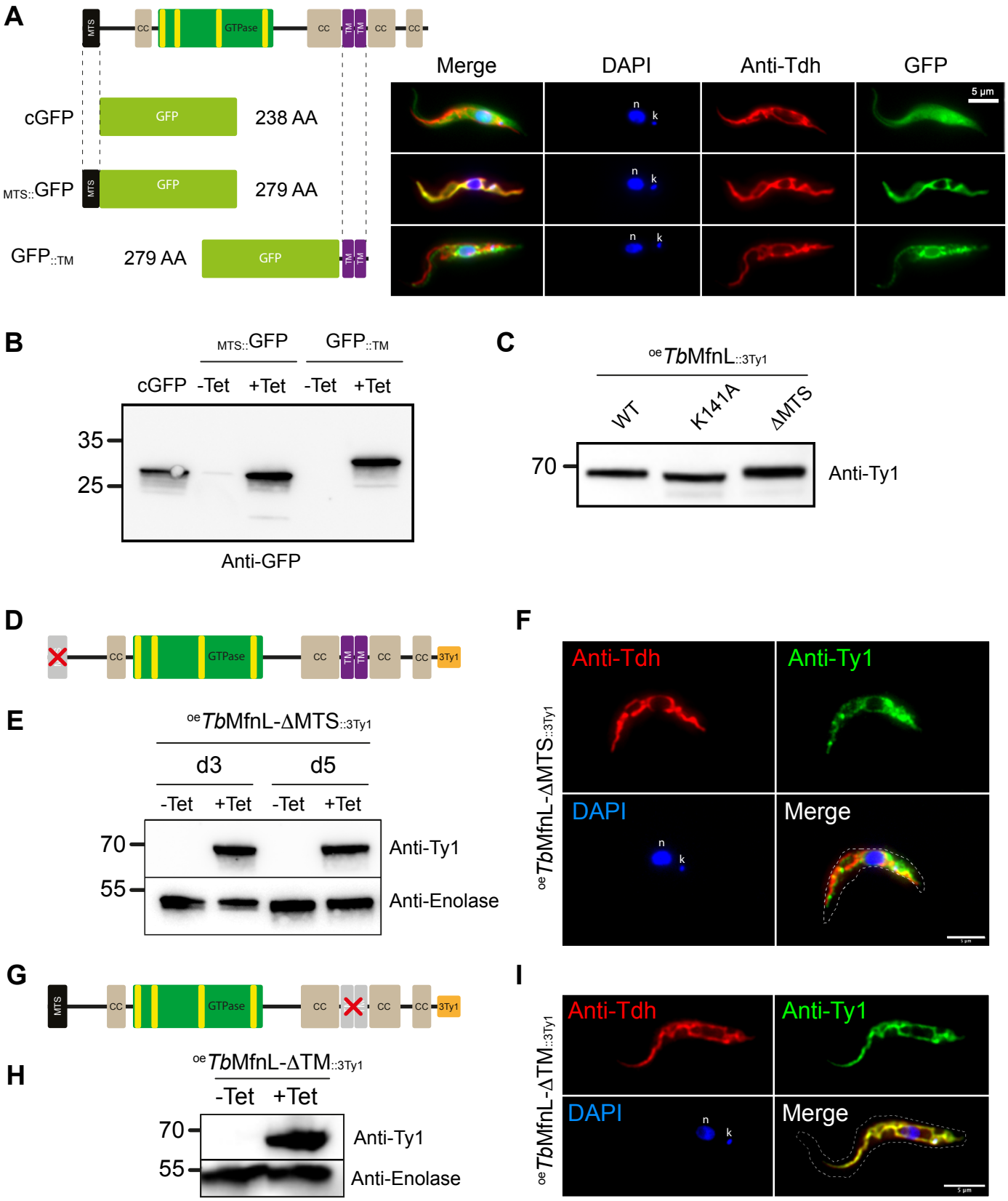
A
MTS
CC
GTPase
CC
TM
TM
CC
CC
cGFP
GFP
238 AA
MTS::GFP
GFP
279 AA
GFP::TM
279 AA
GFP
Merge
DAPI
Anti-Tdh
GFP
5 µm
n
k
B
MTS::GFP
GFP::TM
cGFP
-Tet
+Tet
-Tet
+Tet
35
25
Anti-GFP
C
oeTbMfnL::3Ty1
WT
K141A
ΔMTS
70
Anti-Ty1
D
CC
GTPase
CC
TM
TM
CC
CC
3Ty1
E
oeTbMfnL-ΔMTS::3Ty1
d3
d5
-Tet
+Tet
-Tet
+Tet
70
55
Anti-Ty1
Anti-Enolase
F
oeTbMfnL-ΔMTS::3Ty1
Anti-Tdh
Anti-Ty1
DAPI
Merge
n
k
G
MTS
CC
GTPase
CC
CC
CC
3Ty1
H
oeTbMfnL-ΔTM::3Ty1
-Tet
+Tet
70
55
Anti-Ty1
Anti-Enolase
I
oeTbMfnL-ΔTM::3Ty1
Anti-Tdh
Anti-Ty1
DAPI
Merge
n
k

Figure 7

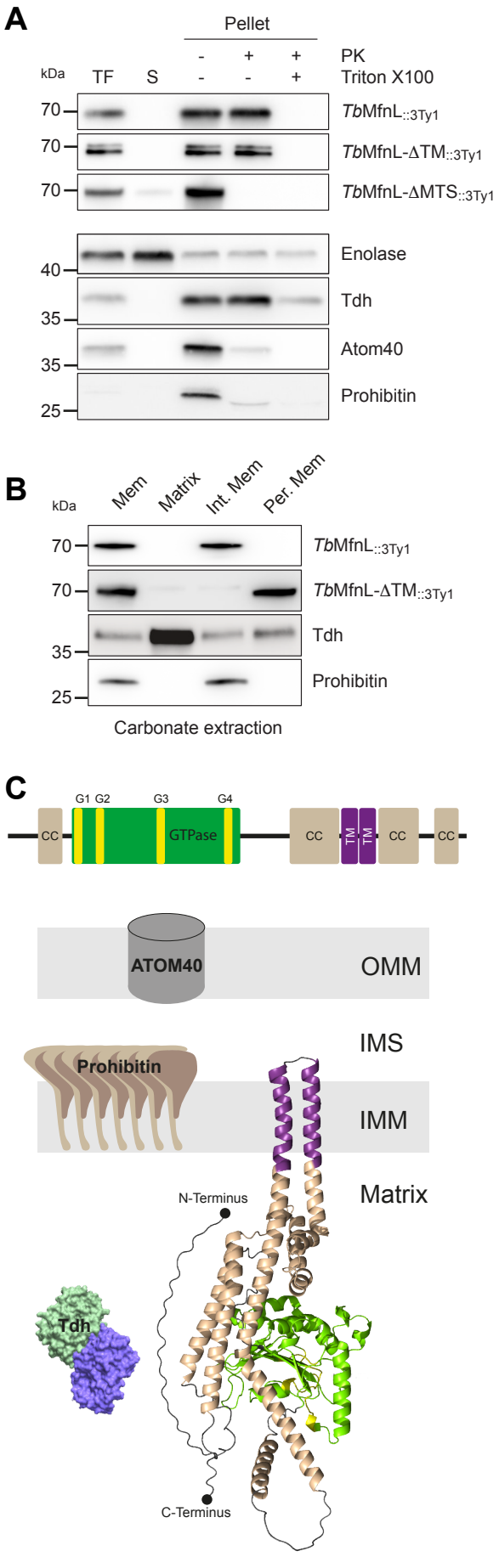
A
Pellet
PK
Triton X100
kDa
TF
S
70
70
70
40
35
35
25
TbMfnL::3Ty1
TbMfnL-ΔTM::3Ty1
TbMfnL-ΔMTS::3Ty1
Enolase
Tdh
Atom40
Prohibitin
B
kDa
Mem
Matrix
Int. Mem
Per. Mem
70
70
35
25
TbMfnL::3Ty1
TbMfnL-ΔTM::3Ty1
Tdh
Prohibitin
Carbonate extraction
C
G1
G2
G3
G4
CC
GTPase
CC
TM
TM
CC
CC
ATOM40
OMM
IMS
Prohibitin
IMM
Matrix
N-Terminus
Tdh
C-Terminus

Figure 8

SUPPLEMENTAL INFORMATION

Figure S1: Alignment of various kinetoplastid MfnL proteins.
Figure S2: Alignment between *Tb*MfnL and various eukaryotic and prokaryotic MfnLs.
Figure S3: Complete maximum likelihood phylogenetic tree of eukaryotic and prokaryotic DSPs.
Figure S4: Growth curves of parental, over-expressing, and mutant cells.
Figure S5: Inactivation of *Tb*MfnL expression using the CRISPR/Cas9 system.
Figure S6: TEM analysis of cells cultured on glucose or proline.
Figure S7: Down-regulation of *Tb*MfnL expression by RNAi.
Figure S8: Results of the ImageJ plugin applied to rhodamine-stained cells.
Figure S9: Overexpression levels of different *Tb*MfnL variants.
Figure S10: Variation in *Tb*MfnL expression levels upon tetracycline induction.
Figure S11: Mitochondrial localization of *Tb*MfnL as shown by immunoelectron microscopy.
Figure S12: Full gel results shown for the PK and carbonate assays.
Figure S13: pLDDT score for *Tb*MfnL protein derived from AlphaFold predictions.
Data S1: ImageJ code used in the study.
Table S1: BLASTp analysis results for several identified organisms.
Table S2: List of all primers and guide RNAs utilized in this study.
Table S3: List of all antibodies used in this study.

Data S1 - Code ImageJ: Mitochondrial junctions (MJ)

```
run("Duplicate...", "title=ORI duplicate channels=2");
run("Duplicate...", "title=Estfond");
run("Gaussian Blur...", "sigma=10");
imageCalculator("Divide create 32-bit", "ORI","Estfond");
selectWindow("Result of ORI");
rename("OriCorr");
selectWindow("Estfond");
setAutoThreshold("Li dark");
run("Create Selection");
selectWindow("OriCorr");
run("Restore Selection");
run("Enlarge...", "enlarge=10 pixel");
setAutoThreshold("Li dark");
run("Analyze Particles...", "size=15-500 show=Masks");
rename("Mask");
run("Options...", "iterations=1 count=4 pad do=Open");
run("Duplicate...", "title=Skeleton");
setOption("BlackBackground", false);
run("Skeletonize");
run("Duplicate...", "title=Ends");
run("Options...", "iterations=1 count=7 pad do=Erode");
imageCalculator("Subtract create", "Skeleton","Ends");
selectWindow("Result of Skeleton");
rename("Endpoints");
selectWindow("Skeleton");
run("Duplicate...", "title=Jonctions");
run("Options...", "iterations=1 count=6 pad do=Erode");
run("Analyze Particles...", "size=0-5000 summarize");
imageCalculator("Add create", "Endpoints","Jonctions");
selectWindow("Result of Endpoints");
rename("Combo");
imageCalculator("Subtract create", "Skeleton","Combo");
selectWindow("Result of Skeleton");
rename("Segments");
selectWindow("Combo");
close();
selectWindow("ORI");
setOption("ScaleConversions", true);
run("8-bit");
run("Merge Channels...", "c1=Jonctions c2=Endpoints c3=Segments c4=ORI create ignore"); close("\\Others");
```

TABLE S1 TO S3

Table S1 –Results from BLASTp and EukProt v3 (query: *Tb*MfnL) of several identified organisms

Name	Organism	Domain Clade	Sequence ID	Amino acid	E-Value	Cover (%)	Identity (%)	Presence of Opa1 /Mgm1	Presence of Mfn /Fzo1	Presence of MidX**	Mitochondrial targeting signal prediction TargetP-2.0 PSORT II MitoFates
*Tb*MfnL	*Trypanosoma brucei*	Eukaryota Discoba; Euglenozoa Kinetoplastea	Tb927.7.2410 (XP_845864.1)	600	0.0	100	100	NO	NO	NO	0.6068 0.3040 0.2000
*El*MfnL	*Euglena longa*	Eukaryota Discoba; Euglenozoa Euglenida	EP00668_Euglena_ longa_P029018	530	8.9e-115 (7e-111)	83	42.8	NO	NO	NO	ND*
*Dp*MfnL	*Diplonema papillatum*	Eukaryota Discoba; Euglenozoa Diplonemea	KAJ9468802.1	479	1e-87 (2e-84)	76	36.3	NO	NO	NO	0.7375 0.3910 0.9300
*Pg*MfnL	*Polarella glacialis*	Eukaryota Sar; Alveolata Dinophyceae	CAE8737761.1	601	2e-79 (3e-80)	73	39.1	NO	NO	NO	0.0063 0.1110 0.0030
*Hf*MfnL	*Hondaea fermentalgiana*	Eukaryota Sar; Stramenopiles Bigyra	GBG23909.1	536	4e-77 (1e-78)	82	35.6	NO	NO	NO	0.5606 0.2170 0.9540
*Ah*MfnL	*Achlya hypogyna*	Eukaryota Sar; Stramenopiles Oomycota	OQR97000.1	498	2e-81 (2e-82)	82	36.6	NO	NO	NO	0.9793 0.7390 0.9990
*Ct*MfnL	*Chaetoceros tenuissimus*	Eukaryota Sar; Stramenopiles Ochrophyta	GFH50037.1	552	1e-77 (6e-78)	74	35.6	NO	NO	NO	0.6911 0.3040 0.8800
*Cht*MfnL	*Chrysochromulina tobinii*	Eukaryota Haptista; Haptophyta Pavlovales	KOO35358.1	514	2e-65 (4e-72)	51	42.5	NO	NO	NO	0.5910 0.2610 0.8740
*Pb*MfnL	*Planctomycetota* bacterium	Prokaryota Planctomycetota	HLY10620.1	448	2e-81 (3e-81)	74	36.8	NO	NO	NO	0.0000 0.1110 0.0000
*Ps*MfnL	*Pedosphaera* sp.	Prokaryota Verucomicrobia	MCH2381658.1	479	2e-75 (1e-76)	79	35.3	NO	NO	NO	0.0099 0.2170 0.6920
*Rc*MfnL	*Rubrimonas cliftonensis*	Prokaryota α-Proteobacteria	WP_093253540.1	450	6e-74 (6e-80)	74	35.6	NO	NO	NO	0.0002 0.1110 0.0100
*Gp*MfnL	*Gammaproteobacteria* bacterium	Prokaryota γ-Proteobacteria	RTZ59088.1	457	1e-71 (6e-80)	75	34.7	NO	NO	NO	0.0000 0.2220 0.0070
*Mb*MfnL	*Myxococcales* bacterium	Prokaryota δ-Proteobacteria	MCA9558847.1	452	5e-70 (4e-71)	77	33.3	NO	NO	NO	0.0001 0.3330 0.0010
*Ld*MfnL	*Lentisphaerae* bacterium	Prokaryota Lentisphaerae	NLB69313.1	465	2e-54 (5e-55)	64	33.1	NO	NO	NO	0.0168 0.0000 0.2470
*Kb*MfnL	*Kiritimatiellae* bacterium	Prokaryota Kiritimatiellae	MBO7223041.1	459	3e-52 (2e-55)	42	43.0	NO	NO	NO	0.0003 0.2610 0.0730
*Hs*Mfn	*Homo sapiens mitofusin-2*	Eukaryota Homo sapiens	NP_001121132.1	757	<1e-2	70	15.4	YES (Opa1)	YES (Fzo1)	NO	0.0787 0.2170 0.0880
*Sc*Fzo1	*Saccharomyces cerevisiae*	Eukaryota Fungi	NP_009738.1	855	<1e-2	61	16.8	YES (Mgm1)	YES (Mfn)	NO	0.0000 0.0430 0.0000
*Nc*BDLP	*Nostoc punctiforme* PCC 73102	Bacteria Cyanobacteriota	WP_2412711.1	693	<1e-2	69	18.2	NO	YES (Mfn)	NO	0.0001 0.1740 0.0240
*Tc*MfnL	*Trypanosoma cruzi*	Eukaryota Discoba; Euglenozoa Kinetoplastea	RNC57734.1	611	0.0	83	54.2	NO	NO	NO	0.6242 0.3910 0.7960
*Le*MfnL	*Leishmania enriettii*	Eukaryota Discoba; Euglenozoa Kinetoplastea	XP_067693110.1	602	2e-130	97	39.5	NO	NO	NO	0.4552 0.1110 0.8820
*Phs*MfnL	*Phytomonas sp. EM1*	Eukaryota Discoba; Euglenozoa Kinetoplastea	CCW65548.1	590	5e-89	78	32.2	NO	NO	NO	0.8692 0.3910 0.9800

ND*, not determined as the N-terminus sequence is unavailable. Sequence IDs beginning with "EP" originate from EukProt v3 database. Parentheses in the E-Value column indicate the E-value obtained from the reciprocal BLASTp analysis, using the putative MfnL ortholog as the query against the *T. brucei* proteome. E-score value below 1e-2 could be considered as "not significant". **We were unable to identify the MidX sequence in the genomes of species that contain the *Tb*MfnL sequence.

Table S2 – Primers used in this study

Name	Sequence	Used for
ET198	TTCGTGTTGCCAACTACAAGGTGAAAAATTTTCTGCGAGCTGGTGAACGGCAACCGCTGGGTAATGAGGTGAGGGTCAAAGGTTCTGGTAGTGGTTCC	Endotag
ET199	CATGCTCGGCAACCTAAGCATGATAGTCCGCGGTAAGAGCAAAAGAACCAGCGCCCCACGTAAATTTGCTTCCAACATTTCCAATTTGAGAGACCTGTGC	
ET160	CATAACGTTACCCACCACATCATCACTGAAGCGACTGTTGCGCAGAAGTCATGACCGAGTACAAGCCCACGGTG	CRISPR/Cas9
ET161	TGTAGTAGTCGCAAAACACATGCGGTTAGTCGAACAGTTGGCACCCAACTTCAGGCACCGGGCTTGCGGGTCATG	
ET211	ATTGACACTCCTATTCATTTGAATGATCGGACATCAGTTGAGGGTCAGCTATGACCGAGTACAAGCCCACGGTG	
ET242	CACACCGTGAAGCAAACCAACGTGTCACGGCGAACAGATCATACCCCCTGTCAGGCACCGGGCTTGCGGGTCATG	
ET92	GCGGCGAGGGTGCGTACGGCCCGG	
ET93	TCACCGTCACCGCCGACGTCGAGG	
ET109	CTGTGGTTCCCAAGGACAATCACC	
MFN_102	ACTGTTGCGCAGAAGTCAGT(NGG)	
MFN_721	TCAGTTGAGGGTCAGCTCAG(NGG)	
MFN_1772	AACCGCTGAGTGATGAGGCG(NGG)	
ET189	GATCAAGCTTCCACATCATCACTGAAGCGACTGT	RNAi
ET190	GATCCTCGAGGTTGGAGATACGCCCGATCGCTGC	
ET191	GATCAAGCTTCTCGAGCCTCGGTTATGTCGTCTTCACCAC	
ET192	GATCGGATCCCCACATCATCACTGAAGCGACTGT	
ET362	GATCGGATCCTTATTTTGATGTTTGACCCC	
ET363	GATCCTCGAGCGGTTGAGGAACTCTTATTG	
ET94	GATCCATATGGGATCCAAGCTTATGAGGCAGTTAGGAAGTGCAG	*Tb*MfnL
ET95	GATCGGTACCGCGGCCGCTCTAGATTATTTGACCCTCACCTCATTACC	
ET96	GATCGGTACCTCTAGATTTGACCCTCACCTCATTACCCAG	
ET149	GAACCACAGCGCGGGAGCGTCTACGATGATTAATC	K141A
ET150	GATTAATCATCGTAGACGCTCCCGCGCTGTGGTTC	
ET197	GATCGCGGCCGCAAGCTTCATATGGGTGCCAACTGCTCGACTAACC	ΔMTS
ET292	CCGGAAGATGAAGGTTAAGTCATTGGTTGACTTTG	ΔTM
ET293	CAAAGTCAACCAATGACTTAACCTTCATCTTCCGG	

Table S3 – Antibodies used in this study

Name	Species	Dilution	Source/Ref
Anti-Ty1	Mouse	WB 1:800	iMET lab
		IF 1:500	
		UExM 1:250	
Anti-HA	Mouse	WB 1:1000	Biolegend
		IF 1:1000	
		UExM 1:500	
Anti-HA	Rat	IF 1:1000	Roche
Anti-Tdh	Rabbit	WB 1:500	iMET lab
		IF 1:200	
		UExM 1:100	
Anti-Enolase	Rabbit	WB 1:100000	Gift from P. Michels, Edinburgh, UK
Atom40	Rabbit	WB 1:10000	Gift from A. Schneider, Bern, Switzerland
Anti-Frdg	Rabbit	WB 1:50	iMET lab
Anti-Hsp60 H7	Mouse	IF 1:500	iMET lab
Anti-PPDK	Rabbit	WB 1:1000	iMET lab
Anti-GFP	Rabbit	WB 1:1000	Abcam
Anti-Prohibitin	Rabbit	WB 1:1000	Gift from H. Hashimi, Czech Republic
Anti-Mouse HRP	Goat	WB 1:5000	Bio-Rad
Anti-Rabbit HRP	Goat	WB 1:10000	Bio-Rad
Anti-Mouse Alexa Fluor 594	Donkey	IF 1:400	ThermoFisher
		UExM 1:250	
Anti-mouse Alexa Fluor 488	Donkey	IF 1:400	ThermoFisher
		UExM 1:250	
Anti-Rabbit Alexa Fluor 594	Donkey	IF 1:400	ThermoFisher
		UExM 1:250	
Anti-Rabbit Alexa Fluor 488	Donkey	IF 1:400	ThermoFisher
		UExM 1:250	
Anti-Rat Alexa Fluor 594	Donkey	IF 1:400	ThermoFisher

Supplemental figures

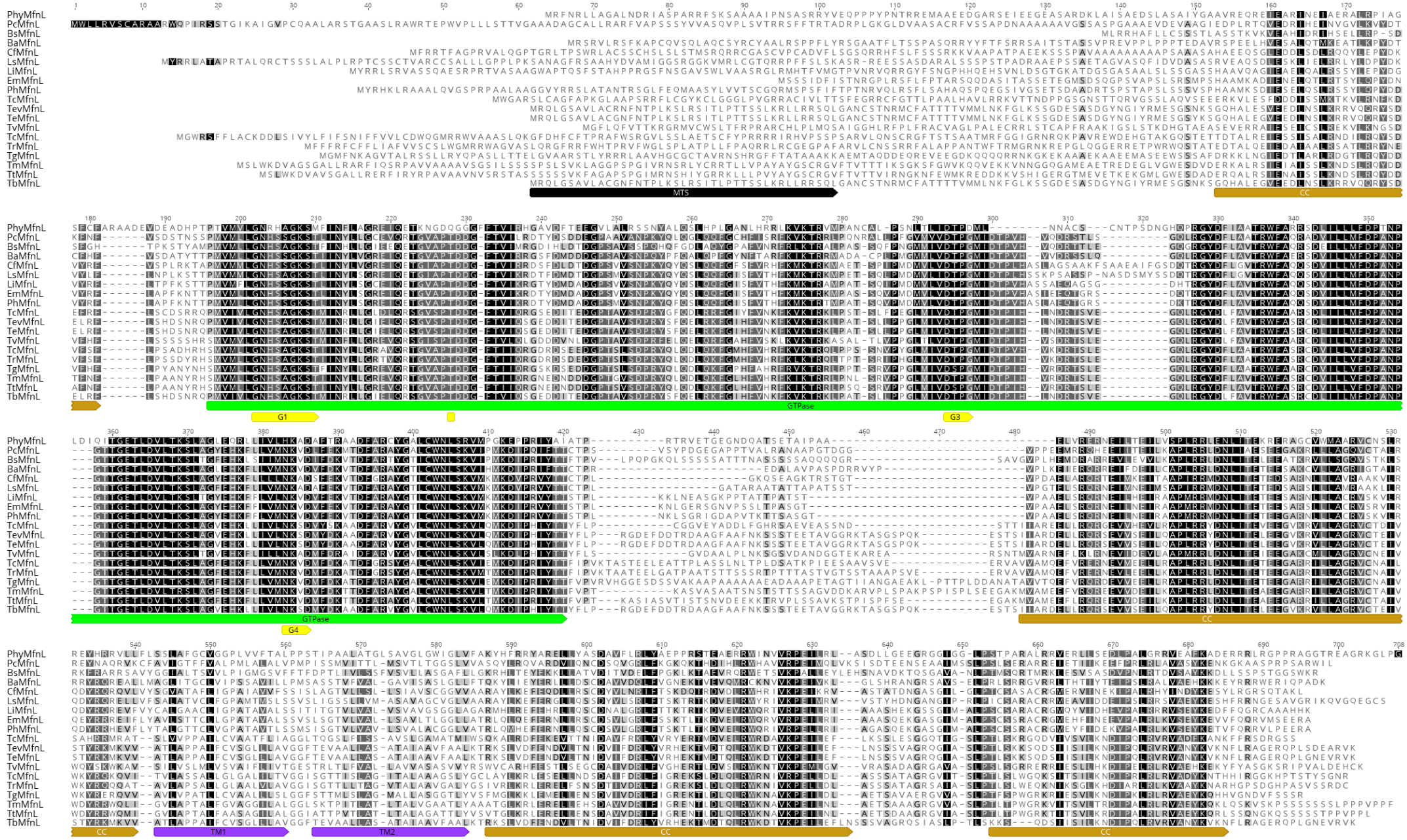

Figure S1 - Sequence alignement between *Tb*MfnL and various kinetoplastids MfnL. MTS, predicted mitochondrial targeting sequence are indicated by grey boxes; GTPase domain is indicated by a green box, and the four GTP-binding motifs are indicated by yellow boxes and numbered; The coil coil domain are indicated by light brown boxes. TM, transmembrane span are indicated by purple boxes. Identities and similarities are represented by white characters on a black background and black characters on a grey background respectively. *Tb*MfnL, *Trypanosoma brucei* DRP (ID: Tb927.7.2410); *Phy*MfnL, *Phytomonas* sp. EM1(ID: CCW65548); *Pc*MfnL, *Paratrypanosoma confusum* (ID: PCON_0070060); *Bs*MfnL, *Bodo saltans* (ID: BSAL_56690); *Ba*MfnL, *Blechomonas ayalai* (ID: Baya_002_1420); *Cf*MfnL, *Crithidia fasciculata* (ID: CFAX1_240011500); *Ls*MfnL, *Leptomonas seymouri* (ID: Lsey_0356_0020); *Li*MfnL, *Leishmania infantum* (ID: LINF_220010300); *Em*MfnL, *Endotrypanum monterogeii* (ID: EMOLV88_220009500); *Ph*MfnL, *Porcisia hertigi* (ID: JKF63_04376); *Tc*MfnL, *Trypanosoma cruzi* (ID: TcCLB.508321.60); *Tev*MfnL, *Trypanosoma evansi* (ID: TevSTIB805.7.2480); *Te*MfnL, *Trypanosoma equiperdum* (ID: TEOVI_000623300); *Tv*MfnL, *Trypanosoma vivax* (ID: TvY486_0702250); *Tc*MfnL, *Trypanosoma congolense* (ID: TcIL3000_7_1710); *Tr*MfnL, *Trypanosoma rangeli* (ID: TRSC58_06192); *Tg*MfnL, *Trypanosoma grayi* (ID: DQ04_08691020); *Tm*MfnL, *Trypanosoma melophagium* (ID: LSM04_004715); *Tt*MfnL, *Trypanosoma theileri* (ID: TM35_000191450).

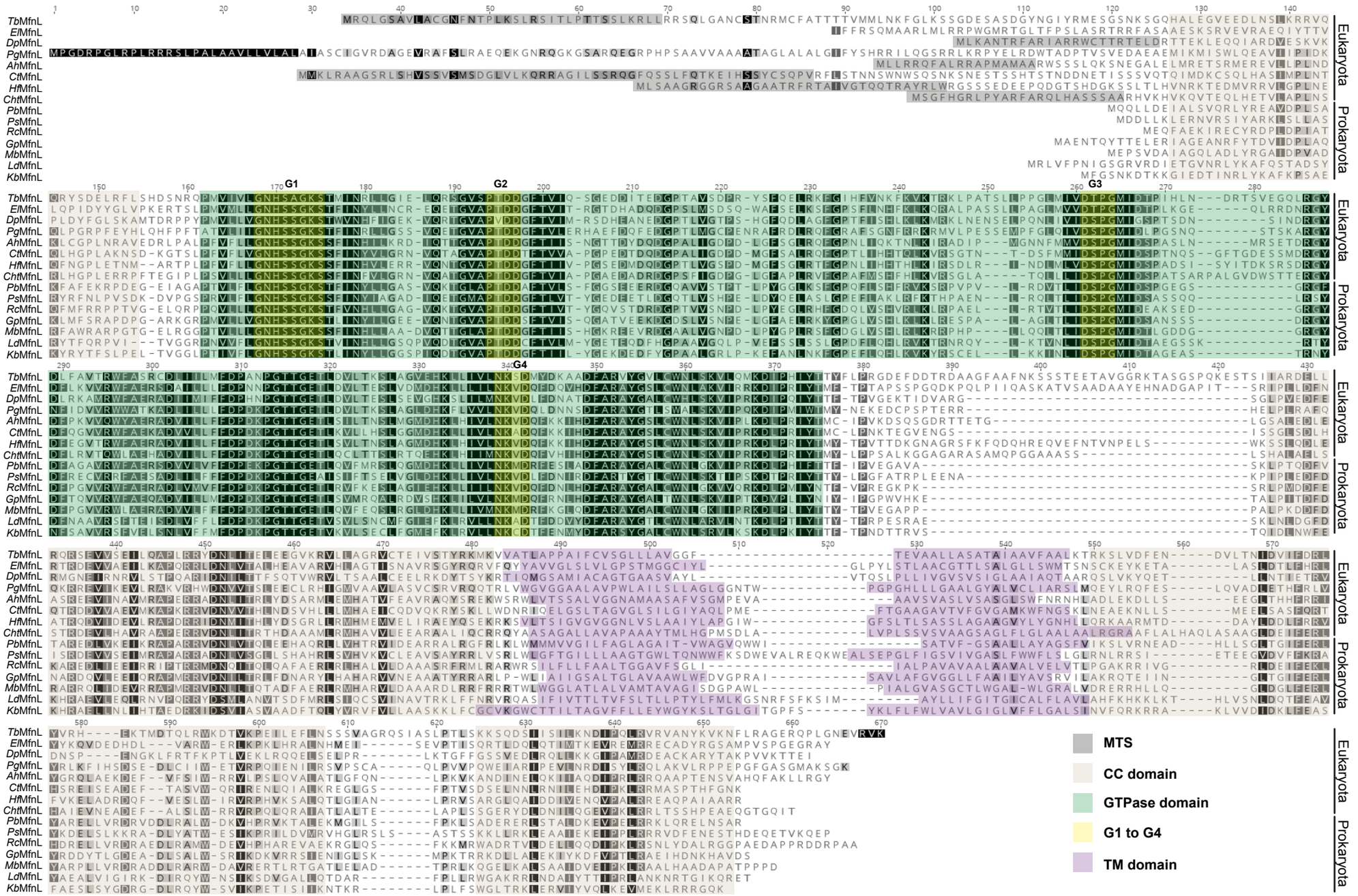

Figure S2 - Sequence and structure alignement between *Tb*MfnL and homologous proteins identified in various eukaryotes and prokaryotes with BLASTp. MTS, predicted mitochondrial targeting sequence are highlighted in grey; GTPase domain is highlighted in green, and the four GTP-binding motifs are highlighted in yellow and numbered; The coil coil domain are highlighted in light brown. TM, transmembrane span are highlighted in purple. Identities and similarities are represented by white characters on a black background and black characters on a grey background respectively. Structure predictions were performed using PSIPRED and mitochondrial targeting sequences were predicted by various algorithms (TargetP2.0, PSORTII, MitoFates, MitoprotII and iPSORT). **Eukayota:** *Tb*MfnL, *Trypanosoma brucei* DRP (ID: Tb927.7.2410); *El*MfnL, *Euglena longa* (ID: EP00668_Euglena_longa_P029018); DpMfnL, *Diplonema papillatum* (ID: KAJ9468802.1); *Pg*MfnL, *Polarella glacialis* (ID: CAE8737761.1); *Ah*MfnL, *Achlya hypogyna* (ID: OQR970001); *Ct*MfnL, *Chaetoceros tenuissimus* (ID: GFH50037.1); *Hf*MfnL, *Hondaea fermentalgiana* (ID: GBG23909.1); *Cht*MfnL, *Chrysochromulina tobinii* (ID: KOO35358.1). **Prokaryota:** *Pb*MfnL, *Planctomycetaceae* bacterium (ID: MBV8881356.1); *Ps*MfnL, *Pedosphaera* sp. (ID: MCH2381658.1); *Rc*MfnL, *Rubrimonas cliftonensis* (ID: WP_093253540.1); *Gp*MfnL, *Gammaproteobacteria* bacterium (ID: RTZ59088.1); *Mb*MfnL, *Myxococcota* bacterium (ID: MBU0550280.1); *Ld*MfnL, *Lentisphaerae* bacterium (ID: NLB69313.1); *Kb*MfnL, *Kiritimatiellae* bacterium (ID: MBO7223041.1). The accession number for *Euglena longa* was obtained from Eukprot V3 database. The alignment was performed using Geneious software with the BLOSUM62 matrix.

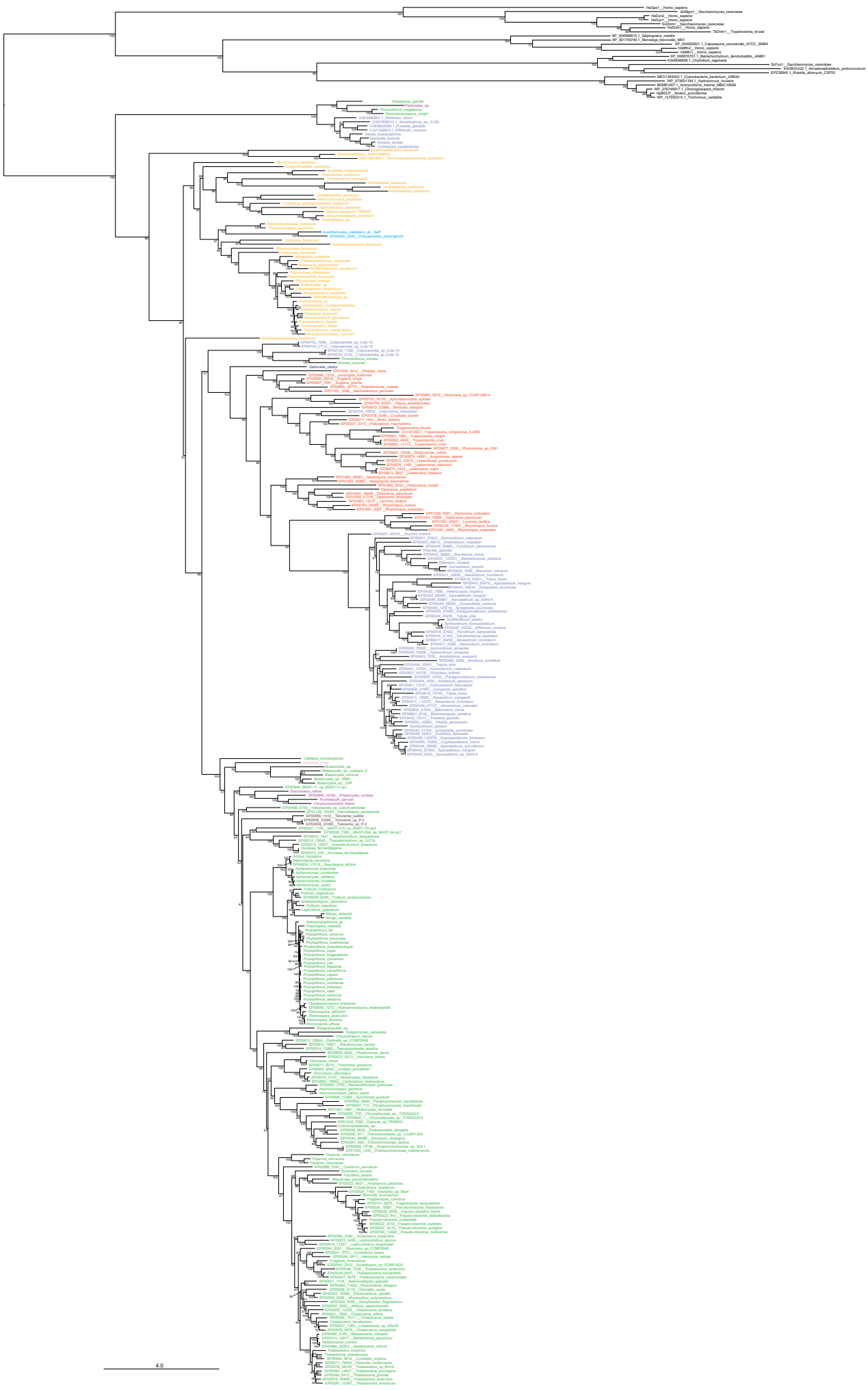

Figure S3 - Maximum likelihood phylogenetic tree of eukaryotic and eukaryotic DSPs. The tree was reconstructed using the LG+C60+G4 model of sequence evolution. Ultrafast bootstrap support values (1000 replicates) are shown on each branch. Taxa are colored according to their taxonomic affiliation.

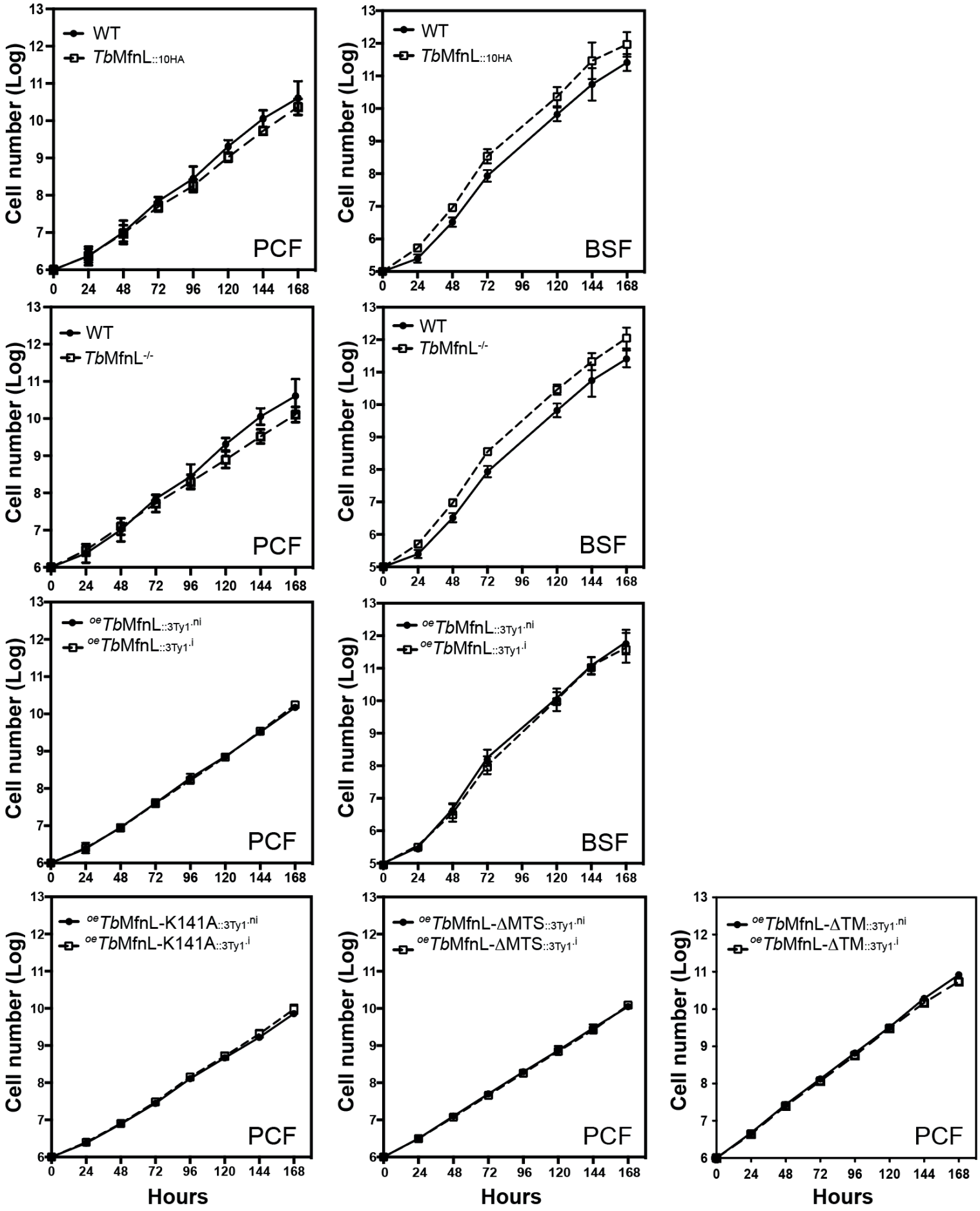

Figure S4 – Growth curves of parental, over-expressing and mutant cells. Cells were maintained in the exponential growth phase and cumulative cell numbers reflect normalization for dilution during cultivation. (.ni) non-induced and (.i) induced cells. PCF, procyclic forms; BSF, bloodstream forms. n=3 to 6.

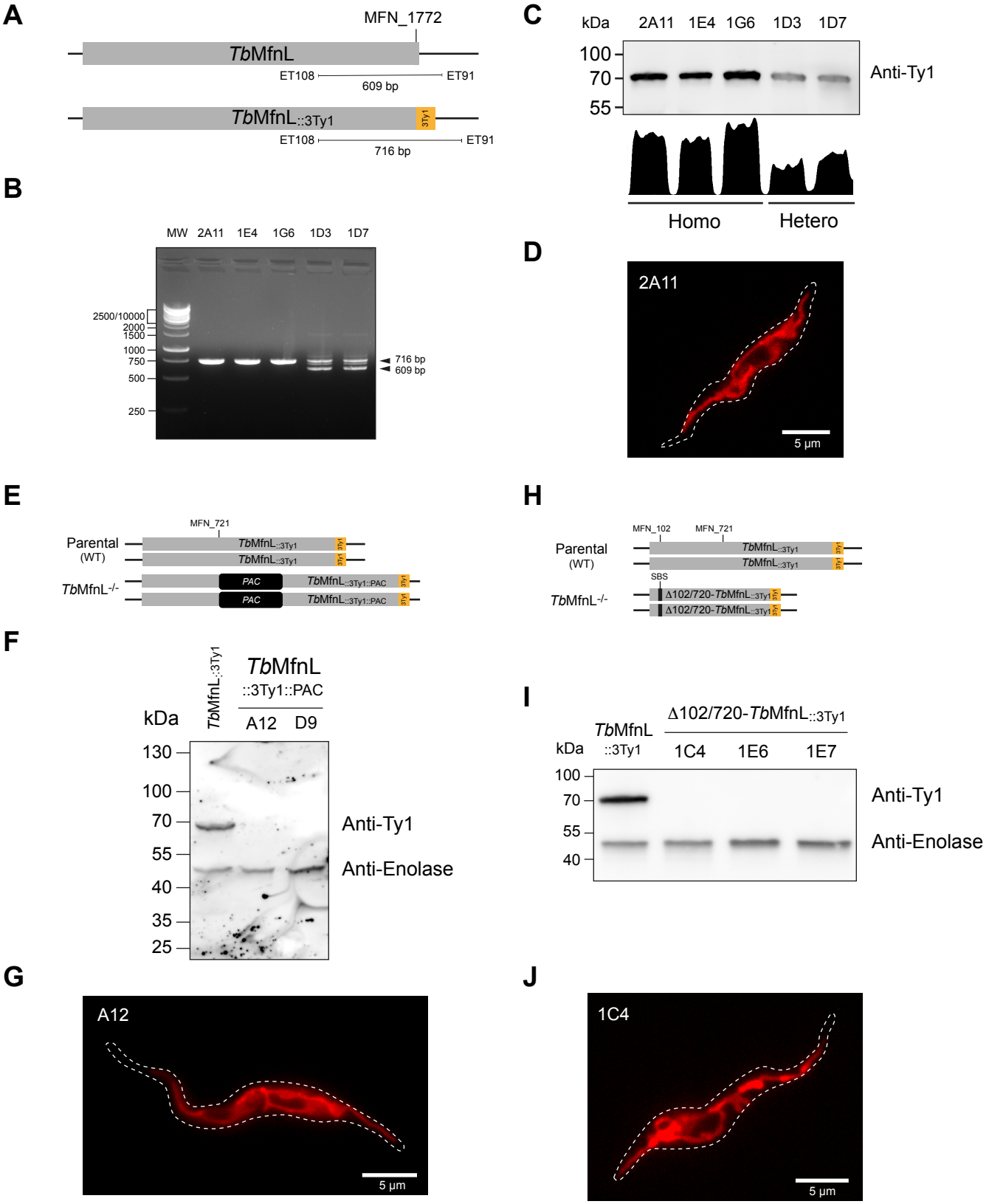

Figure S5 - *Tb*MfnL endotagged with a 3xTy1 sequence and inactivation of *Tb*MfnL expression by CRISPR/-Cas9 in PCF. (A) Design of the endotagged strain with addition of the 3Ty1 tags at the C-terminus of the protein using the CRISPR/Cas9 system. **(B)** Selection of homozygous clones by PCR (2A11, 1E4 and 1G6) using the PCR approach shown in panel A. **(C)** Western-blot analysis of whole cell extracts ($5x10^6$ cells) from *T. brucei* PCF clones expressing *Tb*MfnL$_{::3Ty1}$ revealed with anti-Ty1 antibody and anti-Enolase as a control, and expression levels between homozygous and heterozygous cells. **(D)** Analysis of mitochondrial structure by rhodamine 123 staining in live cells (clone 2A11); **(E)** CRISPR/Cas9-mediated inactivation of *Tb*MfnL using a single guide RNA and insertion of a puromycin resistance marker (PAC) in the *Tb*MfnL$_{::3Ty1}$ (2A11 clone). **(F)** Western blot of whole cell extracts ($5x10^6$ cells) of *Tb*MfnL$_{::3Ty1}$ (clone 2A11 background) and *Tb*MfnL$_{::3Ty1::PAC}$ (A12 and D9) revealed by anti-Ty1 antibody. **(G)** Rhodamine staining of *Tb*MfnL$_{::3Ty1::PAC}$ (clone A12). **(H)** CRISPR/Cas9-mediated inactivation of *Tb*MfnL using two different guide RNAs that deletes approximately 600 bp of the coding sequence in the *Tb*MfnL$_{::3Ty1}$ (2A11 background). **(I)** Western blot of whole cell extracts ($5x10^6$ cells) of *Tb*MfnL$_{::3Ty1}$ (2A11 background) and Δ102/720-*Tb*MfnL$_{::3Ty1}$ clones (1C4, 1E6 and 1E7) revealed by anti-Ty1 and anti-Enolase antibodies. **(J)** Rhodamine staining of Δ102/720-*Tb*MfnL$_{::3Ty1}$ (clone 1C4).

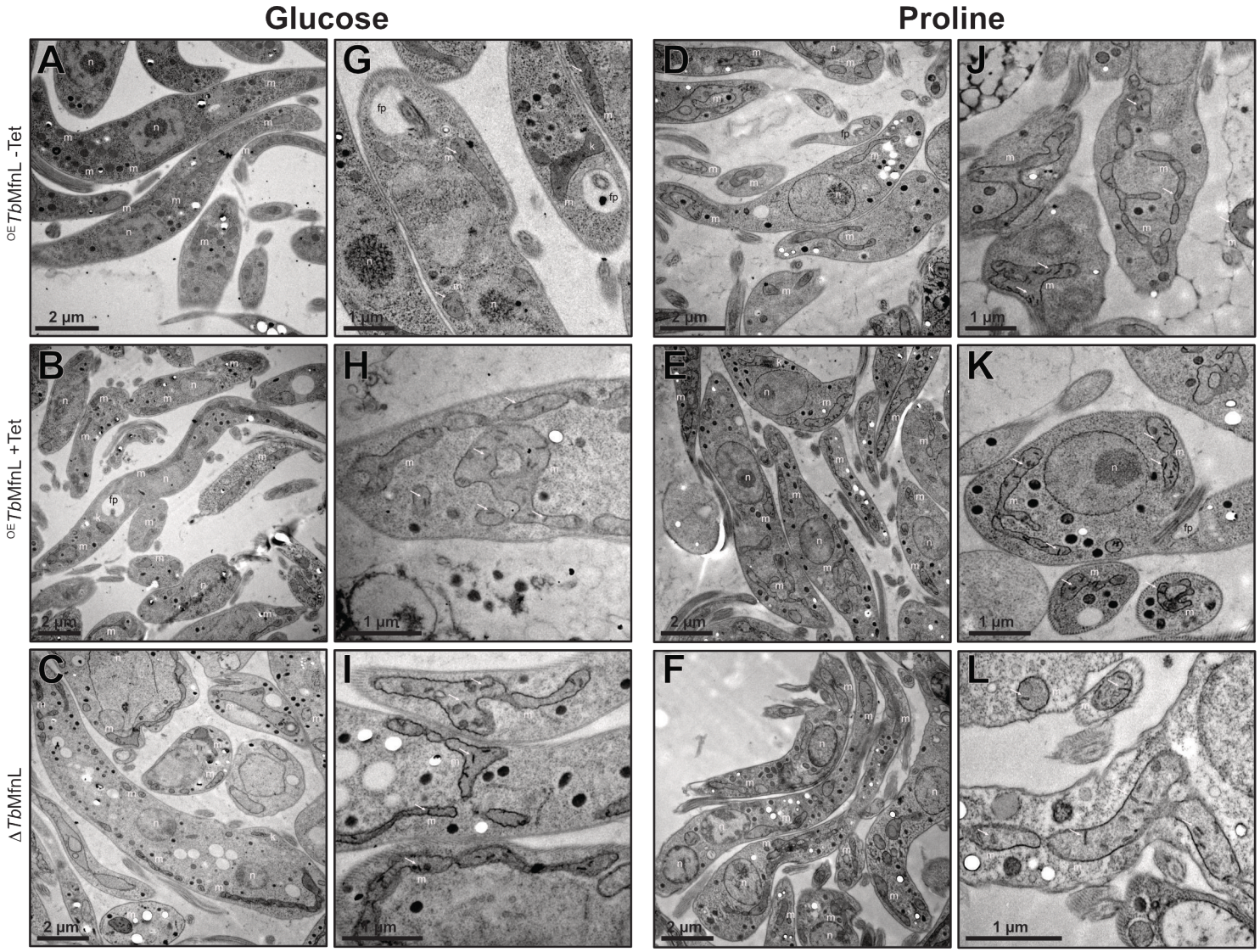

Figure S6 - Mitochondrial ultrastructure analyzed by transmission electron microscopy (TEM). Cells cultured with either glucose or proline, including those overexpressing *Tb*MfnL$_{::3Ty1}$ and inactivated TbMfnL$^{-/-}$, were examined by TEM. Overexpression of *Tb*MfnL$_{::3Ty1}$ was induced for 5 days with tetracycline (Tet) prior to TEM analysis. Panels A–F provide an overview, while panels G–L focus on the mitochondrion and cristaes. n, nucleus; m, mitochondrion; k, kinetoplast; fp, flagellar pocket; white arrows point to the cristae.

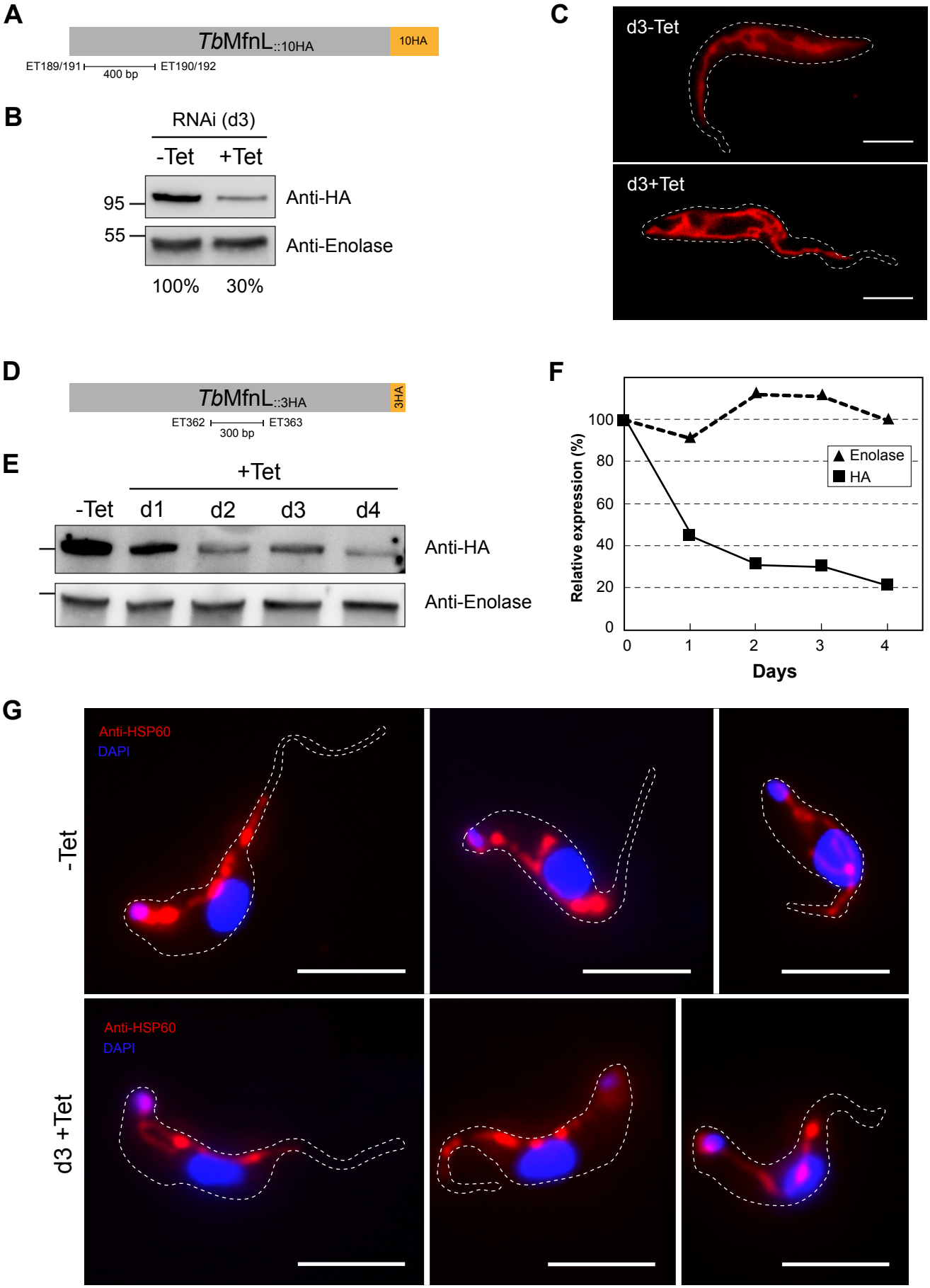

Figure S7 - Inhibition of *Tb*MfnL expression by RNAi in PCF (A/B/C) and BSF (D/E/F/G). (A) Shematic representation of the sequence used for down-regulation of *Tb*MfnL expression in PCF. **(B)** *Tb*MfnL$_{::10HA}$ down-regulation by RNA interference in PCF. Western blot analysis of total extract (5x10^6 PCF cells) of non-induced (-Tet) and induced (+Tet) cells using anti-HA antibody after 3 days of tetracycline induction. Antibody against Enolase was used as a loading control. **(C)** Rhodamine 123 labelled mitochondrial network of cells incubated with tetracycline for 3 days. **(D)** Shematic representation of the sequence used for down-regulation of *Tb*MfnL expression in BSF. **(E)** *Tb*MfnL$_{::3HA}$ down-regulation by tetracycline-induced RNA interference in BSF. Western blot analysis of the total extract (5x10^6 BSF cells) of non-induced (-Tet) and induced (+Tet) cells using anti-HA antibody after 4 days of tetracycline induction. Antibody against Enolase was used as a loading control. **(F)** Relative expression of down-regulation of *Tb*MfnL expression by RNAi in BSF. **(G)** Mitochondrial network labelled with anti-HSP60 from cells incubated or not with tetracycline for 3 days. The scale bar represents 5 µm.

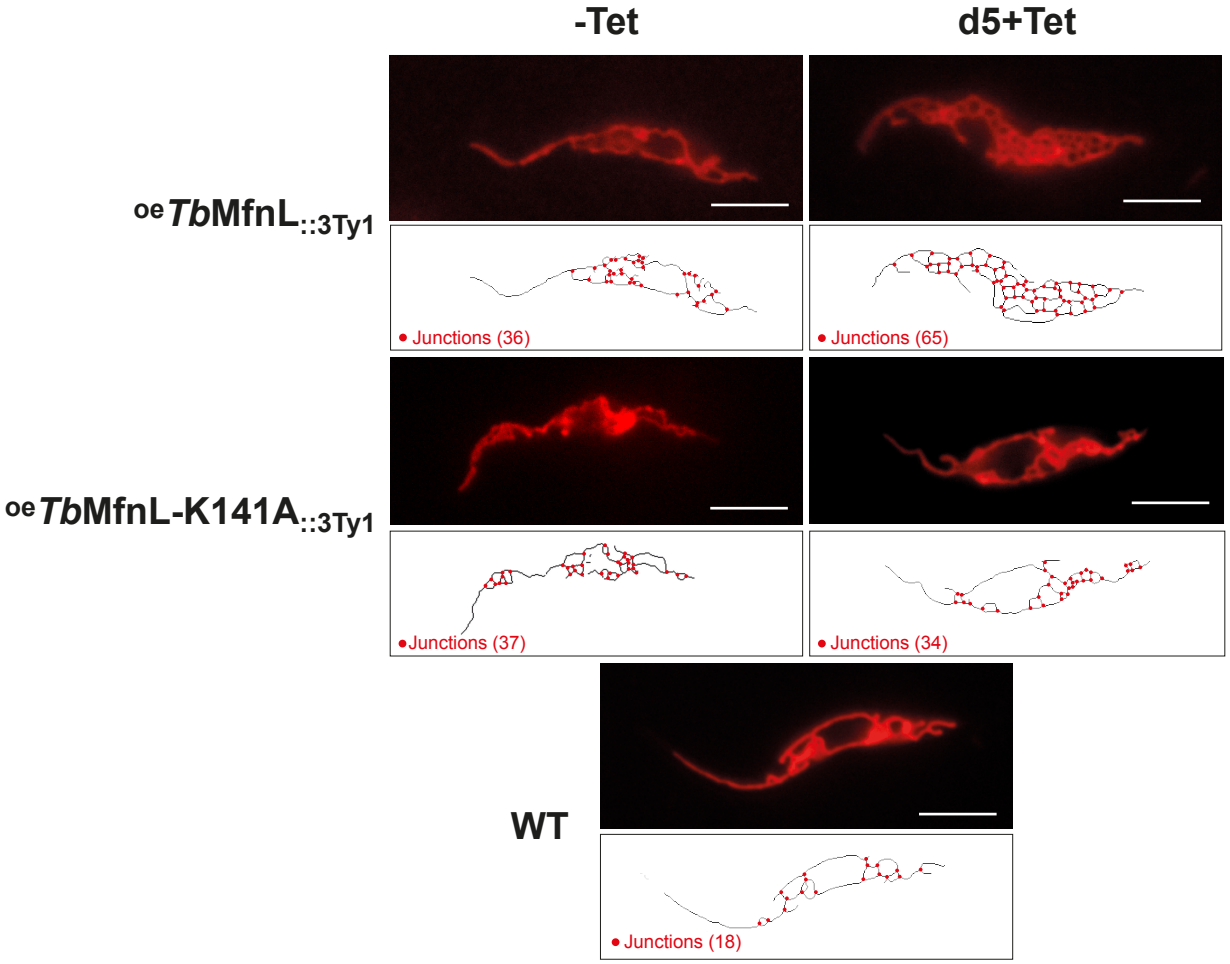

Figure S8 - Mitochondrial shape of parental WT, ^{oe}*Tb*MfnL$_{::3Ty1}$ and ^{oe}*Tb*-MfnL-K141A$_{::3Ty1}$ PCF cells. The top panel depicts live cells stained with rhodamine 123. Bottom panel was obtained using the ImageJ macro (Mitochondrial Junctions). Tet refers to tetracycline, d5, tetracycline induced cells for 5 days. The scale bar corresponds to 5 µm. ni , non-induced cells; d5 .i, induced cells for 5 days. The scale bar corresponds to 5 µm. Red circles in the skeleton image represent the junctions of three mitochondrial tubules.

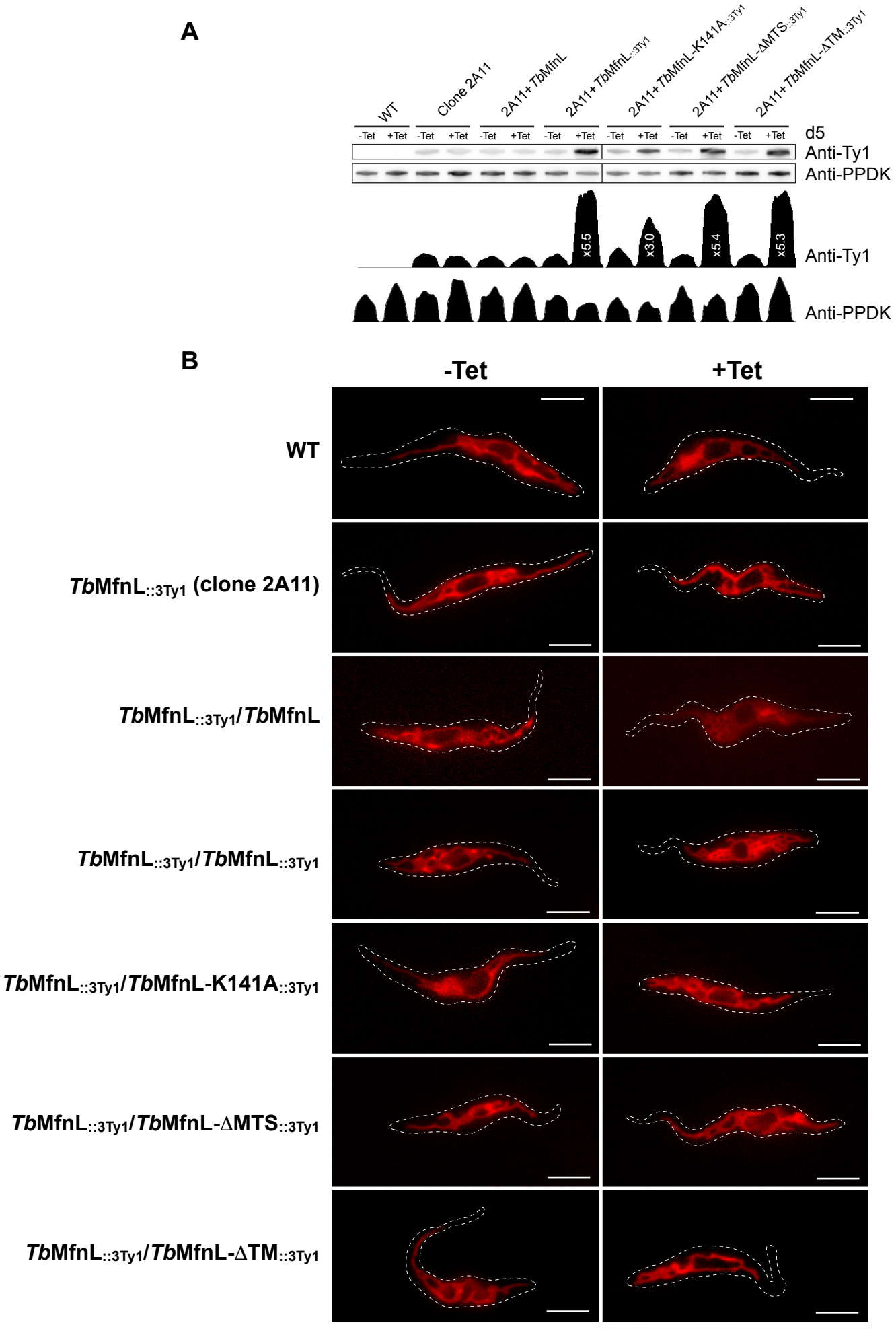

Figure S9 - Overexpression of *Tb*MfnL in endotagged cells. (A) Western-blot of whole-cell extracts ($5x10^6$ cells) of *T. brucei* parental WT PCF and expressing various *Tb*MfnL in *Tb*MfnL::3Ty1 background (clone 2A11) revealed with an anti-Ty1 antibody. Quantification of the expression were performed using ImageJ with PPDK as a loading control. **(B)** Mitochondrial structure analysis using rhodamine 123 staining on living cells; mitochondrial structure of parental WT PCF and expressing various *Tb*MfnL in *Tb*MfnL::3Ty1 background without tetracycline (-Tet) and 5 days after addition of tetracycline (+Tet). The scale bar represents 5 µm.

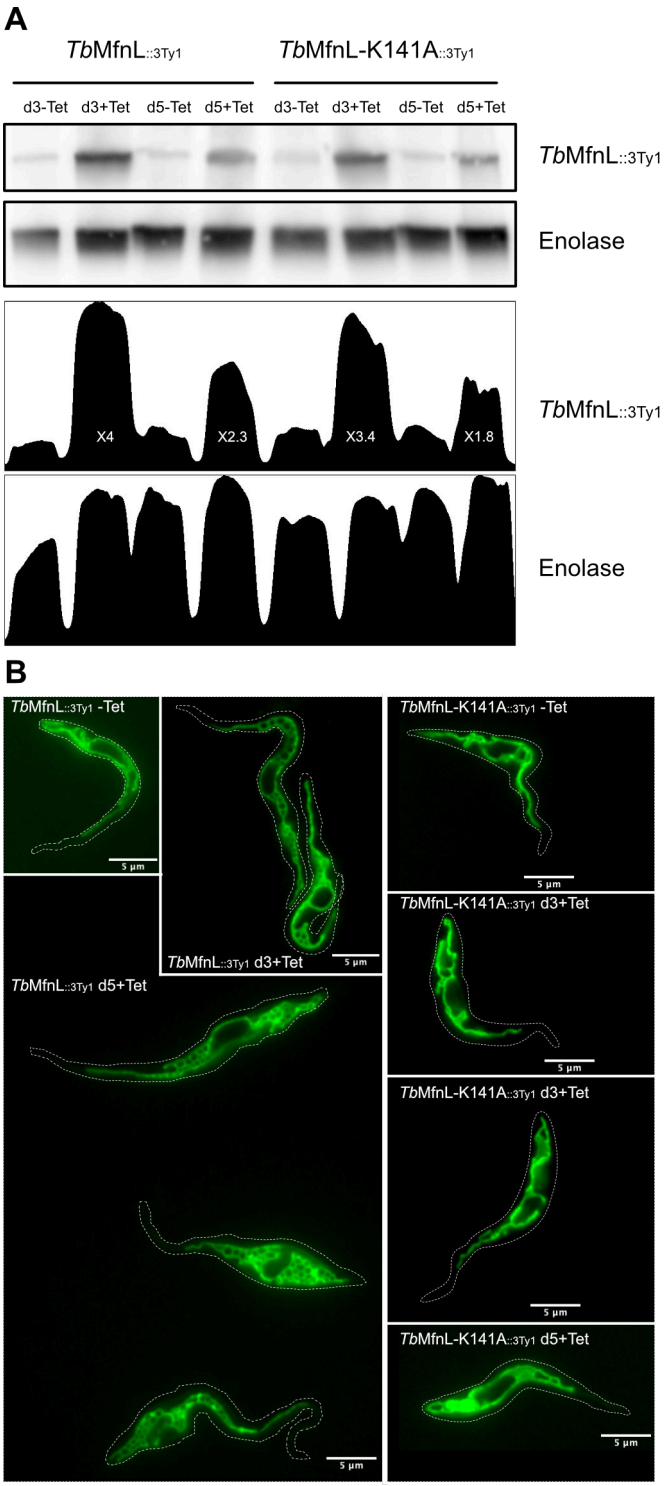

Figure S10 - Variation in the expression level of *Tb*MfnL::3Ty1 induced by tetracycline.. (A) Western blot analysis of whole-cell extracts (5 x 10^6 cells) from *T. brucei* PCF expressing *Tb*MfnL::3Ty1 and *Tb*MfnL-141A::3Ty1 in the *Tb*MfnL::3Ty1 background (clone 2A11) probed with an anti-Ty1 antibody. Expression levels were quantified using ImageJ, with PPDK as a loading control, at day 3 and day 5 following tetracycline induction. (B) Corresponding mitochondrial structures were visualized using Mitotracker staining on live cells. The scale bar represents 5 µm.

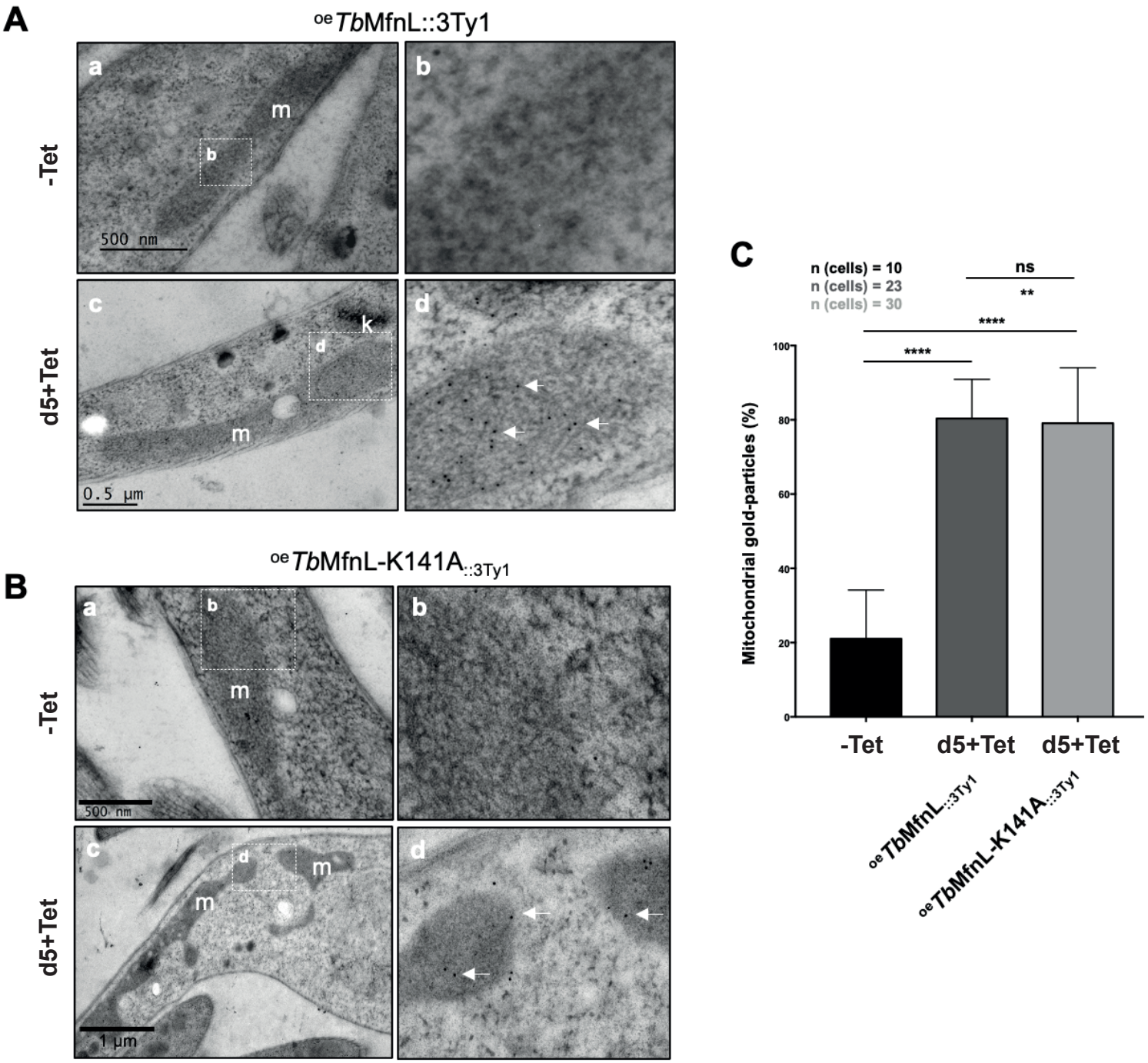

Figure S11 - Immuno localization of *oeTb*MfnL$_{::3Ty1}$ by electron microscopy. Immuno localization of *oeTb*MfnL$_{::3Ty1}$ **(A)** and *oeTb*DBFK141A$_{::3Ty1}$ **(B)** expressed in PCF by electron microscopy. Non-induced cells (-Tet, a and b) and 5 days induced cells (+Tet, c and d) were labelled with an anti-Ty1 antibody and an anti-mouse IgG-gold particle conjugate; black dots represent gold particles highlighted by white arrows; b/d are magnification of a and c, respectively. **(C)** Quantification of mitochondrial gold particles. For non-induced (-Tet) and induced (+Tet) *oeTb*MfnL$_{::3Ty1}$ cells, 221 and 3076 gold particles were counted, respectively, and for non-induced (-Tet) and induced (+Tet) *oeTb*MfnL-K141A$_{::3Ty1}$ cells, 78 and 1123 gold particles were counted, respectively. A mean of the non-induced (-Tet) cells from the two strains is represented on the graph. Statistic: t test - Confidence interval 95% - P-value style: 0.1234 (ns); 0.0332 (*); 0.0021 (**); 0.0002 (***); <0.0001 (****).

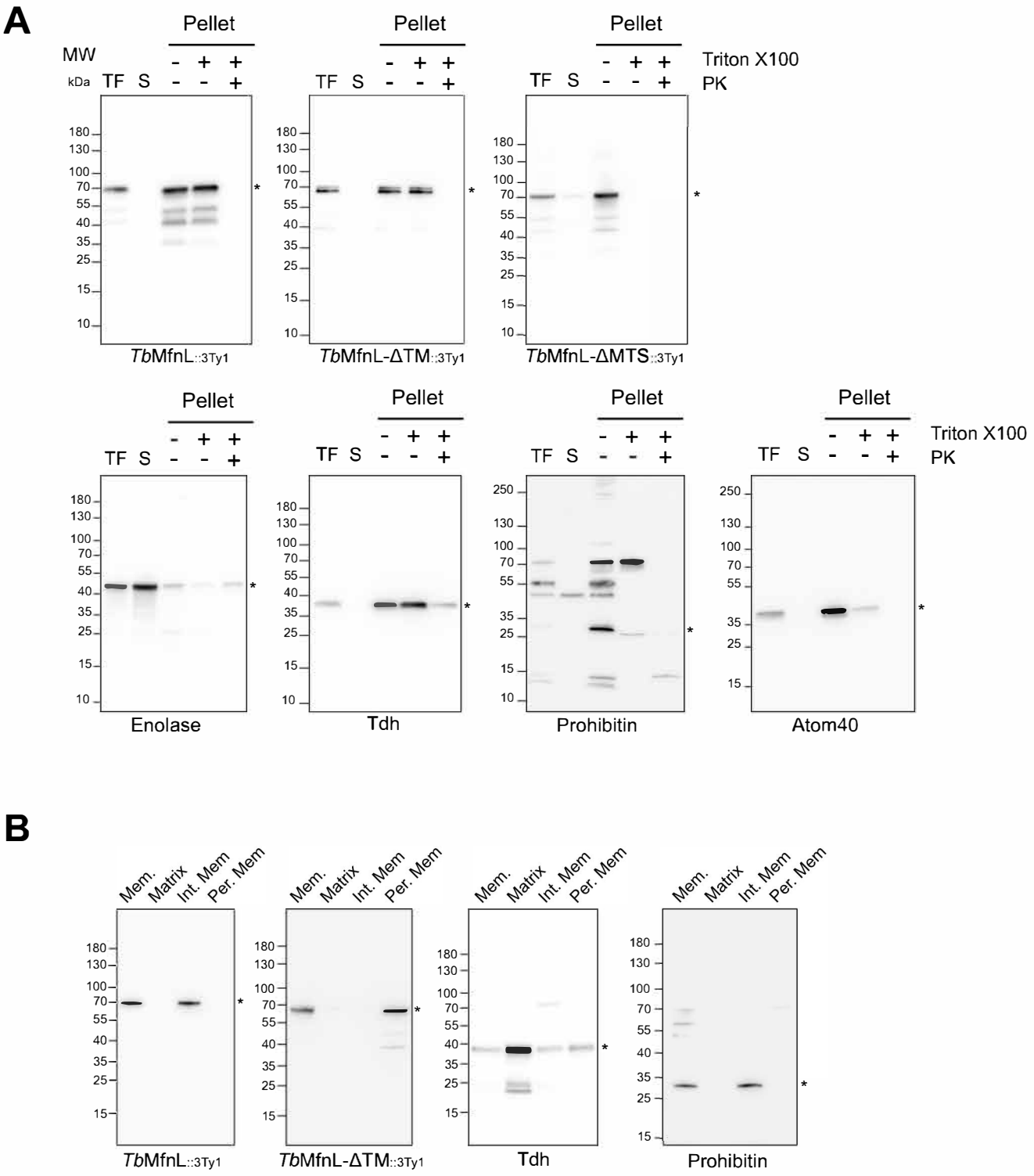

Figure S12 - Membrane topology of *Tb*MfnI (entire western blot). (A) The Proteinase K protection assay involved incubating mitoplasts with Proteinase K and Triton X100, as denoted by the"+" symbol. TF represents the total fraction containing both cytoplasmic and membrane components; S denotes the supernatant, comprising the cytosolic contents; and Pellet represents the organelle fraction. **(B)** Carbonate extraction of mitochondria isolated from ^{oe}*Tb*MfnL $_{::3Ty1}$ and ^{oe}*Tb*MfnL-ΔTM$_{::3Ty1}$ cells. Mem., membrane fraction; Matrix, matrix fraction; Int. Mem, integral membrane fraction; Per. Mem, peripheral membrane fraction. The star indicates the corresponding protein. The expected sizes of the proteins are as follows: *Tb*MfnL - 62 kDa, Enolase - 46 kDa, Tdh - 37 kDa, Prohibitin - 31 kDa, and Atom40 - 38 kDa.

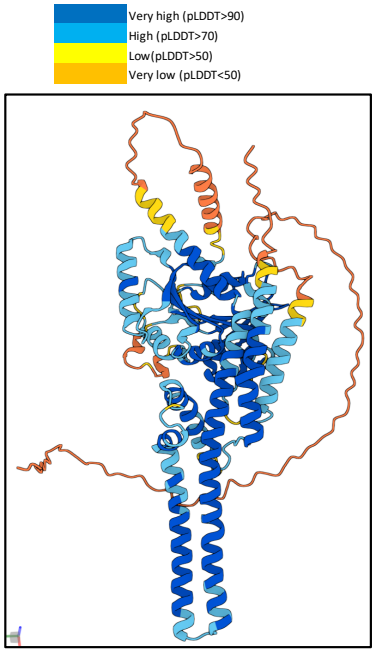

	AA	pLDDT score	
1	M	30.09	MTS
2	R	30.36	
3	Q	28.32	
4	L	33.91	
5	G	30.08	
6	S	26.27	
7	A	30.52	
8	V	30.24	
9	L	25.05	
10	A	30.77	
11	C	23.79	
12	G	28.12	
13	N	28.51	
14	F	30.13	
15	N	30.87	
16	T	33.73	
17	P	32.74	
18	L	24.73	
19	K	30.40	
20	S	30.62	
21	L	25.14	
22	R	28.56	
23	S	26.47	
24	I	30.04	
25	T	29.81	
26	L	25.17	
27	P	33.36	
28	T	30.91	
29	T	27.51	
30	S	27.63	
31	S	28.48	
32	L	27.61	
33	K	27.46	
34	R	27.17	
35	L	28.51	
36	L	27.51	
37	R	26.41	
38	R	27.63	
39	S	24.84	
40	Q	26.30	
41	L	30.18	
42	G	27.69	
43	A	25.13	
44	N	26.65	
45	C	23.42	
46	S	28.41	
47	T	26.33	
48	N	26.16	
49	R	23.54	
50	M	23.67	
51	C	23.15	
52	F	22.13	
53	A	25.43	
54	T	22.58	
55	T	25.67	
56	T	22.30	
57	T	22.70	
58	V	24.23	
59	M	21.24	
60	M	23.95	
61	L	22.69	
62	N	24.71	
63	K	22.27	
64	F	25.57	
65	G	22.84	
66	L	23.94	
67	K	20.30	
68	S	24.15	
69	S	20.69	
70	G	24.95	
71	D	21.00	
72	E	24.69	
73	S	23.45	
74	A	22.79	
75	S	24.60	
76	D	23.42	
77	G	24.04	
78	Y	27.27	
79	N	26.60	
80	G	24.63	
81	I	26.70	
82	Y	29.75	
83	R	25.55	
84	M	30.48	
85	E	25.61	
86	S	29.84	
87	G	31.32	
88	S	35.66	
89	N	47.10	
90	K	45.22	
91	S	50.44	
92	G	56.13	
93	Q	61.15	
94	H	66.26	
95	A	70.77	
96	L	74.28	
97	E	76.83	
98	G	83.25	
99	V	84.21	
100	E	84.67	

	AA	pLDDT score	
101	E	87.40	
102	D	87.07	
103	L	87.37	
104	N	87.13	
105	S	89.50	
106	L	88.33	
107	K	86.54	
108	R	86.66	
109	R	87.75	
110	V	84.71	
111	Q	83.18	
112	Q	80.17	
113	R	78.57	
114	Y	74.96	
115	S	66.78	
116	D	67.17	
117	E	68.54	
118	L	69.72	
119	R	74.35	
120	F	80.29	
121	L	74.08	
122	S	67.50	
123	H	60.88	
124	D	62.16	
125	S	54.19	
126	N	59.16	
127	R	73.84	
128	Q	85.21	
129	P	91.76	GTPase
130	M	94.59	
131	V	97.21	
132	I	97.25	
133	V	96.38	
134	L	93.62	
135	G	90.57	
136	N	85.07	
137	H	81.27	
138	S	84.26	
139	A	89.08	
140	G	90.91	
141	K	93.23	
142	S	92.82	
143	T	92.85	
144	M	94.35	
145	I	94.85	
146	N	94.11	
147	R	91.74	
148	L	92.82	
149	L	93.18	
150	G	90.33	
151	I	91.43	
152	E	90.23	
153	L	91.08	
154	Q	90.54	
155	R	83.38	
156	S	77.03	
157	G	70.88	
158	V	63.25	
159	S	60.79	
160	P	60.25	
161	T	61.06	
162	D	64.27	
163	D	73.97	
164	G	87.85	
165	F	94.69	
166	T	95.60	
167	V	96.49	
168	I	96.05	
169	Q	94.65	
170	S	93.67	
171	G	92.72	
172	E	91.13	
173	D	93.11	
174	D	95.26	
175	I	95.38	
176	T	95.42	
177	E	95.00	
178	D	94.54	
179	G	93.68	
180	P	95.47	
181	T	95.98	
182	A	94.32	
183	V	93.79	
184	S	91.98	
185	D	91.02	
186	P	86.58	
187	R	85.84	
188	Y	87.16	
189	S	86.33	
190	F	92.12	
191	Q	90.83	
192	E	90.32	
193	L	93.02	
194	R	93.17	
195	K	93.19	
196	F	91.65	
197	G	91.05	
198	I	90.85	
199	H	90.58	
200	F	93.21	

	AA	pLDDT score	
201	V	94.41	GTPase
202	N	92.76	
203	K	91.95	
204	F	95.44	
205	K	95.29	
206	V	96.02	
207	K	96.07	
208	T	95.66	
209	R	95.25	
210	K	94.65	
211	L	92.48	
212	P	92.47	
213	A	85.90	
214	T	86.79	
215	S	90.32	
216	L	90.22	
217	L	89.35	
218	P	86.20	
219	P	84.46	
220	G	87.65	
221	L	92.72	
222	M	95.22	
223	I	96.64	
224	V	96.73	
225	D	95.26	
226	T	93.32	
227	P	88.90	
228	G	85.40	
229	M	82.81	
230	I	74.74	
231	D	64.39	
232	T	53.20	
233	P	45.52	
234	I	48.10	
235	H	48.34	
236	L	47.69	
237	N	43.31	
238	D	47.74	
239	R	51.95	
240	T	44.58	
241	S	44.56	
242	V	47.06	
243	E	40.19	
244	G	44.51	
245	Q	54.40	
246	L	61.55	
247	R	73.74	
248	G	79.50	
249	Y	85.88	
250	D	87.28	
251	L	87.58	
252	F	89.23	
253	A	90.50	
254	V	93.02	
255	T	94.01	
256	R	93.92	
257	W	93.46	
258	F	94.97	
259	A	93.83	
260	S	89.95	
261	R	90.66	
262	C	93.54	
263	D	94.01	
264	L	95.59	
265	I	96.56	
266	I	96.78	
267	L	94.51	
268	M	93.47	
269	F	90.63	
270	D	84.88	
271	P	75.87	
272	A	73.22	
273	N	71.64	
274	P	57.80	
275	G	58.29	
276	T	66.23	
277	T	70.03	
278	G	74.41	
279	E	79.51	
280	T	83.17	
281	L	80.36	
282	D	82.86	
283	V	86.65	
284	L	85.00	
285	T	82.80	
286	K	85.46	
287	S	90.60	
288	L	90.98	
289	A	85.20	
290	G	82.92	
291	V	88.51	
292	E	87.48	
293	H	88.81	
294	K	92.34	
295	L	93.80	
296	L	94.96	
297	I	94.28	
298	V	94.80	
299	L	93.42	
300	N	92.92	

	AA	pLDDT score	
301	K	90.70	GTPase
302	S	89.41	
303	D	85.62	
304	M	82.57	
305	Y	80.41	
306	D	84.59	
307	K	86.06	
308	A	88.68	
309	A	87.31	
310	D	88.50	
311	F	89.95	
312	A	89.11	
313	R	88.92	
314	V	91.10	
315	Y	91.19	
316	G	89.41	
317	V	89.11	
318	L	89.95	
319	C	88.41	
320	W	85.79	
321	N	87.45	
322	L	86.39	
323	S	83.35	
324	K	83.53	
325	V	83.34	
326	L	78.51	
327	Q	79.21	
328	M	84.42	
329	K	85.91	
330	D	85.70	
331	I	88.21	
332	P	92.29	
333	H	93.61	
334	I	95.61	
335	Y	93.98	
336	T	94.15	
337	T	92.41	
338	Y	91.12	
339	F	85.46	
340	L	80.75	
341	P	70.27	
342	R	63.64	
343	G	61.96	
344	D	54.15	
345	E	54.15	
346	F	47.20	
347	D	47.66	
348	D	50.24	
349	T	44.53	
350	R	42.70	
351	D	41.04	
352	A	39.55	
353	A	40.71	
354	G	40.49	
355	F	38.43	
356	A	42.10	
357	A	45.62	
358	F	43.01	
359	N	40.59	
360	K	44.30	
361	S	39.66	
362	S	40.45	
363	S	33.88	
364	T	31.43	
365	E	30.60	
366	E	28.37	
367	T	28.90	
368	A	33.15	
369	V	31.15	
370	G	29.94	
371	G	31.29	
372	R	31.64	
373	K	33.12	
374	T	30.41	
375	A	36.67	
376	S	32.47	
377	G	40.71	
378	S	37.77	
379	P	49.99	
380	Q	50.92	
381	K	50.81	
382	E	54.38	
383	S	51.70	
384	T	59.70	
385	S	68.16	
386	I	64.06	
387	I	62.41	
388	A	78.52	
389	R	81.33	
390	D	84.52	
391	E	88.65	
392	L	91.66	
393	L	91.47	
394	R	92.27	
395	Q	94.73	
396	R	94.44	
397	S	92.87	
398	E	94.18	
399	V	94.94	
400	V	93.87	

	AA	pLDDT score	
401	S	91.91	
402	E	92.57	
403	I	93.76	
404	L	90.31	
405	Q	88.71	
406	A	91.37	
407	P	88.72	
408	L	85.83	
409	R	88.06	
410	R	89.70	
411	Y	88.84	
412	D	89.50	
413	N	89.63	
414	L	88.38	
415	I	90.62	
416	T	90.58	
417	E	87.93	
418	L	89.70	
419	E	92.40	
420	E	90.53	
421	G	91.00	
422	V	92.29	
423	K	93.60	
424	R	93.48	
425	V	92.28	
426	L	92.62	
427	L	93.00	
428	A	93.50	
429	G	92.05	
430	R	92.68	
431	V	93.96	
432	C	92.75	
433	T	93.09	
434	E	92.74	
435	I	93.01	
436	V	92.79	
437	S	92.78	
438	T	91.88	
439	Y	91.71	
440	R	91.85	
441	K	92.85	
442	M	90.74	
443	K	90.58	
444	V	92.34	
445	V	91.43	
446	A	89.68	TM1
447	T	90.05	
448	L	92.98	
449	A	90.56	
450	P	92.07	
451	P	92.99	
452	A	92.99	
453	I	92.02	
454	F	92.55	
455	C	93.17	
456	V	92.37	
457	S	89.44	
458	G	88.60	
459	L	91.31	
460	L	90.27	
461	L	88.85	
462	A	89.54	
463	V	90.22	
464	G	80.07	
465	G	77.03	
466	F	78.81	
467	T	87.11	TM2
468	E	85.10	
469	V	88.21	
470	A	86.71	
471	A	87.34	
472	L	91.10	
473	L	91.08	
474	A	90.86	
475	S	90.55	
476	A	93.22	
477	T	92.62	
478	A	92.24	
479	I	94.68	
480	A	93.87	
481	A	93.78	
482	V	93.93	
483	F	94.51	
484	A	93.38	
485	A	92.99	
486	L	94.18	
487	K	94.12	
488	T	91.68	
489	R	88.91	
490	K	91.22	
491	S	90.47	
492	L	88.84	
493	V	87.13	
494	D	89.98	
495	F	90.46	
496	E	88.11	
497	N	87.15	
498	D	89.23	
499	V	88.19	
500	L	85.15	

	AA	pLDDT score
501	T	86.92
502	N	89.47
503	I	91.19
504	D	92.69
505	V	90.71
506	I	90.59
507	F	92.43
508	D	90.77
509	R	89.21
510	L	88.03
511	Y	86.35
512	V	82.14
513	R	72.40
514	H	66.19
515	E	74.33
516	K	78.89
517	T	89.13
518	M	87.67
519	D	88.07
520	T	91.46
521	Q	92.02
522	L	91.21
523	R	93.12
524	W	94.35
525	K	93.10
526	D	89.41
527	T	90.26
528	V	93.75
529	K	93.82
530	P	92.91
531	E	89.87
532	I	91.06
533	L	90.50
534	E	87.52
535	F	86.95
536	L	85.34
537	N	84.45
538	S	81.42
539	S	74.02
540	S	63.44
541	V	60.85
542	A	59.48
543	G	54.90
544	R	53.19
545	Q	61.23
546	S	74.91
547	I	83.03
548	A	82.81
549	S	82.50
550	L	87.44
551	P	86.56
552	T	87.84
553	L	89.21
554	S	91.83
555	K	91.94
556	K	92.29
557	S	91.79
558	Q	92.95
559	D	93.97
560	S	93.47
561	I	92.61
562	I	94.35
563	S	94.76
564	I	93.68
565	L	93.87
566	K	95.34
567	N	95.14
568	D	94.40
569	I	93.94
570	P	95.29
571	Q	93.59
572	L	91.87
573	R	92.84
574	V	91.85
575	R	90.00
576	V	88.87
577	A	88.39
578	N	88.21
579	Y	84.05
580	K	83.19
581	V	81.73
582	K	78.39
583	N	71.31
584	F	64.70
585	L	52.30
586	R	56.77
587	A	52.51
588	G	42.18
589	E	39.30
590	R	38.11
591	Q	29.15
592	P	29.68
593	L	27.47
594	G	30.79
595	N	29.09
596	E	27.18
597	V	30.32
598	R	26.39
599	V	28.59
600	K	35.84

Figure S13 - AlphaFold structure of *Tb*MfnL with pLDDT scores for each amino acid. The pLDDT scores are color-coded as blue (>90), light blue (>70), yellow (>50), and orange (<50). The MTS sequence is highlighted by a black box, the GTPase domain by a green box, and the transmembrane domains by purple boxes. The average pLDDT score for the entire protein was 72.5.